OPTICAL REFRIGERATION ON CDSE/CDS QUANTUM DOTS

A Dissertation

Submitted to the Faculty

of

Purdue University

by

Muchuan Hua

In Partial Fulfillment of the

Requirements for the Degree

of

Doctor of Philosophy

December 2019

Purdue University

Indianapolis, Indiana

THE PURDUE UNIVERSITY GRADUATE SCHOOL
STATEMENT OF DISSERTATION APPROVAL

Dr. Ricardo S. Decca, Chair

Department of Physics

Dr. Tongcang Li

Department of Physics and Astronomy (Purdue, West Lafayette)

Dr. Ruihua Cheng

Department of Physics

Dr. Yogesh N. Joglekar

Department of Physics

Dr. Jing Liu

Department of Physics

Approved by:

Dr. Ricardo S. Decca

Head of the Graduate Program

To my parents,

who raised me up and whose loving spirit sustains me still.

To my wife,

who has held our family, allowing me to finish this dissertation.

In memory of my grandfather,

the kindest, honest and the most patient man I have ever known.

ACKNOWLEDGMENTS

I would like to express my sincere gratitude and thanks to my advisor Professor Ricardo S. Decca for his professional advising, patient guidance and continuous support over my Ph. D. study and this research. His enthusiasm and immense knowledge in physics has and will encourage me all the time on my way of being a researcher.

I would like to thank the rest of my committee members, Professor Jing Liu, Professor Ruihua Cheng, Professor Tongcang Li and Professor Yogesh N. Joglekar, who have provide me meaningful help and advise for the completion of this dissertation. Especially, I wish to thank Professor Cheng, Professor Liu, their postdocs and graduate students, who had shared tools and equipment with me.

I would like to thank our former technician, Dr. Bruce Ray, from who I learnt the skill of running organic synthesis and other knowledge in chemistry. I also would like to thank Dr. Daniel Minner and Dr. Bijin Li from our Chemistry and Chemical Biology department, who shared professional knowledge and chemicals for my quantum dots synthesis.

I would like to thank Professor Gavrin, Professor Petrache and all the other faculties who gave me help over my Ph. D. study.

I would like to thank administratives in Department of Physics, Juli, Kimberly, Stephanie, Brenda and Clair for their support.

I would like to thank the graduate students in our department, who gave me help.

TABLE OF CONTENTS

LIST OF TABLES

LIST OF FIGURES

Figure Page

Figure Page

Figure Page

Figure Page

Figure Page

SYMBOLS

$\mathcal{A}$	absorbance
$\vec{A}$	vector potential
$A_{\mathrm{e}}^{\mathrm{c}}$	normalization coefficient of a free electron's wavefunction inside the conduction band of a QD
A_0	amplitude of the vector field
a_{c}	effective cross–section area
a	surface area
$B_{\mathrm{h}}^{\mathrm{v}}$	normalization coefficient of a free hole's wavefunction inside the valence ba nd of a quantum dot
B_{k}	normalization constant of phonon-induced electric potential
$\mathcal{C}_{\mathrm{c}}$	complex conjugate
$\mathcal{C}_{\mathrm{QD}}$	concentration of a quantum dot sample
$\mathcal{C}_{\mathrm{seed}}$	concentration of CdSe seeds suspension
C_g	coupling strength
c	speed of light
c_{ph}	speed of sound
$\mathcal{D}$	dipole moment of the quantum dots
d	diameter of quantum dots
d_{cuv}	size of the cuvette
e	electron
$\vec{\mathcal{E}}_{\mathrm{loc}}$	local electric field of a CdSe ion pair in QDs
$\vec{\mathcal{E}}_{\mathrm{lop}}$	electric field introduced by longitudinal optical phonon
f	focal distance
g	phonon density of state
$\mathcal{H}$	Hamiltonian

$\mathcal{H}_{\mathrm{c}}$	Hamiltonian of Coulomb interaction between the electron and hole in a quantum dot
$\mathcal{H}_{\mathrm{e}}^{\mathrm{c}}$	Hamiltonian of a free electron in quantum dots' conduction band
$\mathcal{H}_{\mathrm{h}}^{\mathrm{v}}$	Hamiltonian of a free hole in quantum dots' valence band
$\mathcal{H}_{\mathrm{e}}$	Hamiltonian of a electron in quantum dots within an external radiation field
$\mathcal{H}_0$	unperturbated electronic Hamiltonian
$\mathcal{H}_{\text{e-R}}$	Hamiltonian of the electron-raidiation interaction
H	Heating coefficient
h	hole
I	light intensity
Im	imaginary part of a quantity
j	spherical Bessel function of the first kind
n	spherical Bessel function of the second kind
k	wavenumber
k_{B}	Boltzmann constant
k_{c}	thermal conductivity
k_{s}	intra-band transition rate in the surface band of CdSe quantum dots
k_{int}	inter-band transition rate in CdSe quantum dots
k_{r}	radiative decay rate
k_{nr}	non-radiative decay rate
L_{c}	effective length of the support
$\mathcal{M}$	reduced mass of CdSe ion pairs
m_0	mass of a free electron
m_*	effective mass of exciton
m_{e}^*	effective mass of electron
m_{h}^*	effective mass of hole
$\mathcal{N}$	number density of ion Cd^{2+}-Se^{2-} pairs

N	excitonic population
N_{d}	carrier density in the absorption band of CdSe quantum dots
N_{g}	population density of the ground state
N_{s}	carrier density in the emission band of CdSe quantum dots
N_1	population density of the first excited state
N_2	population density of the second excited state
O_{d}	density of state in the absorption band of CdSe quantum dots
O_{s}	density of state in the surface band of CdSe quantum dots
$\vec{\mathcal{P}}$	polarization of the CdSe ion pairs
P_{b}	radiation absorption power of a single quantum dot
P_{c}	optical cooling power
P_{ex}	power of the excitation laser
$\bar{P}_{\mathrm{h,o}}$	mean heating power of an optical thermometry
P_{H}	total heat transfer between the QDs sample and the environment
P_{h}	heat transfer through thermal conduction
P_{in}	optical power absorbed by the QDs sample
P_{sb}	heat transfer through thermal radiation
P'_{sb}	heat transfer through thermal radiation for a single quantum dot
P_{sc}	cooling power of a single QD
$\vec{p}$	momentum operator
Q_{in}	heat received by the heat engine from the hot reservoir
$Q^{\mathrm{h}}_{\mathrm{out}}$	heat exhausted from the heat energy
Q_{T}	heat extracted by the refrigeration from the cooling substance
$Q^{\mathrm{r}}_{\mathrm{out}}$	heat exhausted from the refrigerator
R_s	spontaneous emission rate
r_{a}	Bohr radius of hydrogen atoms
r_{b}	excitonic Bohr radius
r_{core}	core radius of quantum dots
r_{shell}	shell radius of quantum dots

S	Huang-Rhys factor
s	slope of plots
s_{ref}	slope of the reference dye's data points
T	temperature
T_{f}	effective temperature of the pump light
T_{p}	effective temperature of the emission light
T_{q}	temperature of a single quantum dot
T_{s}	effective temperature of the quantum dot sample
U	Bloch function
$\vec{u}$	displacement of the normal coordinate of phonon mods
$\vec{u}_{\mathrm{lop}}$	relative displacement of Cd and Se ions from their equilibrium positions
u_0	amplitude relative displacement of Cd and Se ions from their equilibrium positions
V	potential energy
$\mathcal{V}_{\mathrm{Cd}}$	volume of $Cd(DDTC)_2$ solution
$\mathcal{V}_{\mathrm{CdS}}$	volume of CdS shell
$\mathcal{V}_{\mathrm{mo}}$	volume of a CdS monolayer
$\mathcal{V}_{\mathrm{seed}}$	volume of CdSe seed suspension
W	work done
w	width of the laser beam
w_0	waist of the Gaussian laser beam
x	distance to the beam waist of the laser spot
Y	spherical Harmonic function
y_0	y-intercept of plots
α	absorption coefficient
α_{b}	background absorption coefficient
α_{p}	photon absorption rate of the sample
$\bar{\alpha}_{\mathrm{p,s}}$	mean absorption rate of a single QD

β	effective spring constant of CdSe lattice
Γ_{i}	intrinsic decay lifetime of the electronic states
δ	Dirac delta function
ε	energy
ε_{a}	absorption energy
ε_{C}	Coulomb interaction energy of the electron-hole pair of the exciton in CdSe quantum dots
ε_{c}	phonon cut-off energy
ε_{e}	energy of free electron inside CdSe quantum dots
ε_{d}	center of the absorption band
ε_{em}	emission energy
$\bar{\varepsilon}_{em}$	mean emission energy
$\varepsilon_{\mathrm{ex}}$	excitation energy
ε_{g}	energy gap of bulk zinc-blende CdSe
$\varepsilon_{\mathrm{g}}^{\mathrm{eff}}$	effective energy gap of zinc-blende CdSe quantum dots
ε_{h}	energy of free hole inside CdSe quantum dots
$\varepsilon_{\mathrm{lop}}$	the longitudinal optical phonon energy
ε_{s}	center of the emission band
$\bar{\varepsilon}_{\mathrm{u}}$	mean up-conversion energy of the photoluminescence light
ε_{12}	energy difference between level 1 and 2
ϵ	dielectric constant
ϵ_{a}	dielectric constant of air
ϵ_{ref}	dielectric constant of the reference dye's solution
ϵ_o	permittivity of vacuum
ϵ_{s}	dielectric constant of the sample's suspension solvent
$\epsilon(0)$	dielectric constant of CdSe (low frequency limit)
$\epsilon(\infty)$	dielectric constant of CdSe (high frequency limit)
ζ	effective photon energy, defined as $\frac{\hbar\omega}{k_{\mathrm{B}}T}$
η	quantum yield

η_{eff}	effective quantum efficiency
η_{c}	cooling efficiency
η_{es}	luminescent escape efficiency
η_{ref}	quantum yield of the reference dye solution
Θ	refraction angle of XRD scanning
θ	polar axis in spherical coordinates
κ	coefficient of engine's performance
Λ	light collection coefficient
λ	wavelength
Ξ	polarizability of CdSe ion pairs
ξ	dimensionality
ρ	charge density
ϱ	emissivity
σ_{ab}	Stefan–Boltzmann constant
σ_{d}	energy variance of the absorption band
σ_{s}	energy variance of the emission band
ς	light extinction coefficient of CdSe seeds
τ_{a}	lifetime of Auger process
τ_{c}	exposure time for the pump laser during optical refrigeration procedure
τ_{nr}	non-radiative decay lifetime
τ_{p}	exposure time for the probe laser during optical thermometry
τ_{r}	radiative decay lifetime
τ_{s}	temporal gap between two consecutive optical thermometry measurements
φ	azimuthal axis in spherical coordinates
Φ	quantum dots' electronic wavefunction
ϕ	electric potential
υ	view factor

χ	root mean square of errors
$\hbar$	reduced Planck's constant
ψ	envelop function
ω	angular frequency
ω_{lop}	angular frequency of longitudinal optical phonons
Ω	solid angle
∇	nabla

ABBREVIATIONS

Ar	argon
CCD	charge coupled device
$Cd(DDTC)_2$	cadmium diethyldithiocarbamate
CdFt	cadmium formate
CdS	cadmium sulfide
CdSe	cadmium selenide
CdTe	cadmium telluride
CO_2	carbon dioxide
DCPL	energy down conversion photoluminescence
DOS	density of states
FWHM	full width at half maximum
HeNe	Helium Neon
H_2S	hydrogen sulfide
IRF	instrument response function
$LiYF_4$	lithium yittrium flouride
LOP	longitudinal optical phonon
MA	myristic acid
NMR	nuclear magnetic resonance
OR	optical refrigeration
OAM	oleylamie
ODE	octadecene
PL	photoluminescence
QY	quantum yield
QDs	quantum dots
SeO_2	selenium dioxide

SBE	sub-band excitation
SQD	semiconducting quantum dot
TBP	tributylphosphine
TDP	time-dependent perturbation
UPCL	up-conversion photoluminescence
XRD	X-ray diffraction
Yb	ytterbium
ZnS	zinc sulfide

NOMENCLATURE

Myristic acid	tetradecanoic acid
Oleic acid	(9Z)-Octadecenoic acid

ABSTRACT

Hua, Muchuan Ph.D., Purdue University, December 2019. Optical Refrigeration on CdSe/CdS Quantum Dots. Major Professor: Ricardo S. Decca.

Optical refrigeration in quantum dots was carried out in this research. Zinc-blende crystalline CdSe/CdS (core/shell structure) QDs were used as the cooling substance using a novel synthesis method recently developed by Peng's group [1,2]. The method can provide a complete surface passivation for the QDs, leading to unitary photoluminescence quantum yield, which is an important criterion for realizing OR. A modified synthesis procedure was implemented in our lab to produce QD samples for the OR experiment. Phonon-assisted up-conversion photoluminescence driven by sub-band gap laser excitation was utilized as the cooling mechanism in the QD samples. A net cooling efficiency was predicted within a range of the laser excitation energy, even after taking into account possible parasitic heating processes. To observe the cooling effect, the experiment was carried out in a thermally isolated environment, which temperature was also monitored. By using an optical thermometry technique developed for this research, a maximum temperature drop of 0.68 ± 0.07 K was observed in the experiment. This development paves the way to use QDs' cooling in new industrial and fundamental research approaches.

1. INTRODUCTION

1.1 History and background of optical refrigeration

Optical refrigeration (OR) is a technique to remove heat (cooling) from a system by using light, providing a non-contact temperature control method. The most famous implementation is atom cooling by Doppler effect, known as Doppler cooling [3], which is an effective method to achieve Bose-Einstein condensation in neutral atom systems. The related research was rewarded by Physics Noble Prizes in 1997 and 2001 [3,4]. The idea of applying OR in solids was first proposed by German physicist Peter Pringsheim [5] in 1929 [1]. He noticed that thermal vibration energy of solids can be potentially removed by spontaneous up-conversion photoluminescence (UCPL, also known as anti-Stokes photoluminescence) processes when the excitation light has energy $\varepsilon_{\mathrm{ex}}$ lower than the mean luminescent energy $\bar{\varepsilon}_{\mathrm{em}}$. However, in 1945, Vavilov initiated the discussion about the compatibility between OR and the second law of thermodynamics [6]. In his argument, he stated if OR processes can be achieved in a system, then such system could potentially become self-contained by recycling the energy of the emitted light, which contradicts the second law of thermodynamics. Pringsheim stated that the entropy of the emitted light is much higher than the one of the incident light (the incident light is monochromatic and uni-directional), therefore, the total entropy of the system increases during the process, and the second law holds. A more comprehensive statement was given by Landau in 1946 [7], in which he concluded that the entropy of either monochromatic or uni-directional light is zero. He also introduced the effective temperature of light (defined as the temperature required by a black body to radiate the same intensity at the light's energy) to calculate the

[1] Pringsheim is referred by other researchers as the first person who introduced the theory of OR in solids. The original paper was written in German, and no English version has been found. Hence, the author has not read the paper

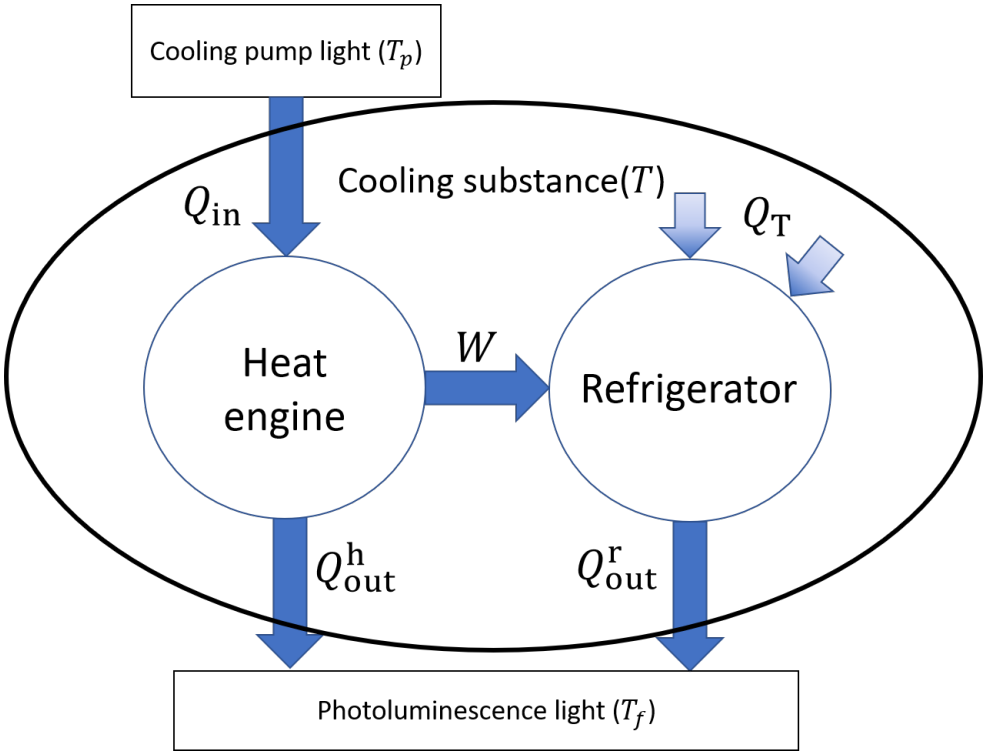

Figure 1.1. Thermodynamic scheme of optical refrigeration system. T denotes the temperature of the material. Q_{in}: heat received by the heat engine from the hot reservoir, $Q^{\mathrm{h}}_{\mathrm{out}}$: heat exhausted from the heat energy, Q_{T}: heat extracted by the refrigerator from the cooling substance, $Q^{\mathrm{r}}_{\mathrm{out}}$: heat exhausted from the refrigerator, W: the work generated by the heat engine.

thermal dynamic limitation of OR. Typically the temperature of incident light source T_{p} is much higher than the temperature of photoluminescence (PL) light, T_{f}. Within these parameters, the thermodynamic scheme of OR can be understood with the schematic plot shown in Fig 1.1. OR is constructed with a heat engine, a refrigerator, a hot reservoir, and a cold reservoir and the cooling substance [8]. In such system, the hot reservoir is connected to the heat engine, driving the heat engine to produce work W, which is used by the refrigerator to remove heat from the cooling substance. Both the heat engine and the refrigerator exhaust heat into the cold reservoir. For the case of OR in solids, the hot reservoir is the excitation light with a very high effective temperature T_{p}, while the heat engine, refrigerator, and the cooling substance are the

same objects, the cooling material. The heat is exhausted in the form of PL light with a relatively low effective temperature T_{f}, where $T < T_{\mathrm{f}} < T_{\mathrm{P}}$. The coefficient of performance κ can be defined as

$$\kappa = \frac{T_{\mathrm{p}} - T_{\mathrm{f}}}{T_{\mathrm{p}}} \frac{T}{T_{\mathrm{f}} - T}. \tag{1.1}$$

Here $\frac{T_{\mathrm{p}} - T_{\mathrm{f}}}{T_{\mathrm{p}}}$ denotes the Carnot's efficiency of the heat engine. $\frac{T}{T_{\mathrm{f}} - T}$ is determined by the intrinsic properties of the cooling material, which are more or less fixed. Thus, for a given system, when $T_{\mathrm{p}} \to \infty$, κ approaches the ideal value $\frac{T}{T_{\mathrm{f}} - T}$, which is the case of an ideal laser [7] (besides its monochromaticity and uni-directional nature, coherence of laser leads to an almost zero entropy with an infinite effective temperature).

For pedagogical reasons, OR process can be described by a three-level system (non-degenerate) shown in Fig. 1.2. Here, N_{g}, N_1 and N_2 are defined as the population densities of the levels. When monochromatically exciting level 1 from the ground state, N_2 is non-zero since level 1 and 2 thermalize at the material's temperature T, following a Boltzmann distribution

$$\frac{N_2}{N_1} = e^{-\varepsilon_{12}/k_{\mathrm{B}}T}, \tag{1.2}$$

where, k_{B} denotes the Boltzmann constant and ε_{12} is the energy difference between levels 1 and 2. Therefore, when a transition from level 2 to the ground state occurrs, cooling is achieved. By defining κ as the ratio of energy removed from the system over the heat been input into the system, for each cooling cycle,

$$\kappa = \frac{\varepsilon_{\mathrm{em}} - \varepsilon_{\mathrm{ex}}}{\varepsilon_{\mathrm{ex}}}. \tag{1.3}$$

Where $\varepsilon_{\mathrm{ex}}$ and $\varepsilon_{\mathrm{em}}$ denote the excitation energy, the energy of level 1 and the emission energy, the energy of level 2 respectively (consider the energy of the ground is zero). To show Eq. 1.1 and 1.3 are identical, the effective temperature T_{p} of the excitation laser and the effective temperature T_{f} of the emission light are introduced. By assuming the transition between the ground state and level 1 is optically allowed with an infinite narrow linewidth, the ground state and level 1 are thermalized with

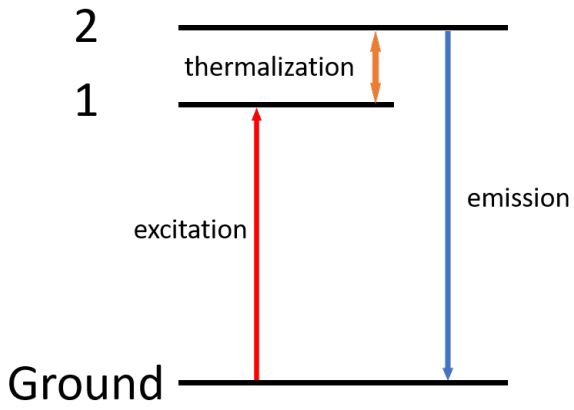

Figure 1.2. Optical refrigeration process in a three-level system. The energy up-conversion in the emission is achieved by monochromatic excitation of the lower excited state, level 1, leading to a non-zero population of level 2 due to thermalization. Here the spontaneous emission from level 1 is ignored to show an optimal cooling effect.

temperature T_{p}. And the population ratio between level 1 and the ground state is given by

$$\frac{N_1}{N_{\mathrm{g}}} = e^{-\varepsilon_{ex}/k_{\mathrm{B}}T_{\mathrm{p}}}. \tag{1.4}$$

Similarly,

$$\frac{N_2}{N_{\mathrm{g}}} = e^{-\varepsilon_{em}/k_{\mathrm{B}}T_{\mathrm{f}}}. \tag{1.5}$$

According to Eq. 1.2, 1.4 and 1.5,

$$\frac{\varepsilon_{\mathrm{em}}}{\varepsilon_{\mathrm{ex}}} = \frac{T_{\mathrm{f}}}{T_{\mathrm{p}}}\frac{(T_{\mathrm{p}} - T)}{(T_{\mathrm{f}} - T)}. \tag{1.6}$$

Eq. 1.1 is derived by substituting Eq. 1.6 into Eq. 1.3, therefore, the two configurations are consistent.

In real systems, the work created by the incident light will not be fully utilized by the cooling process. Non-radiative processes, such as phonon emissions and background absorption could potentially cause heating effects, preventing cooling from being observed. On the other hand, the maximum cooling efficiency is governed by $\frac{k_{\mathrm{B}}T}{\varepsilon_{ex}}$ which is typically small, around 2% for visible light [9]. Therefore, a light source

with perfect monochromaticity and almost zero divergence is required to maximize cooling efficiency. In fact, OR in any material was not achieved until the development of the laser (historically, maser [10]).

The first implementation of OR in solids was done by Epstein *et al.* in 1995 [11]. A 0.3 K temperature decrease was observed in Yb^{3+} doped glass under laser excitation. A schematic of the OR process in this system is shown in Figure 1.3, where laser light

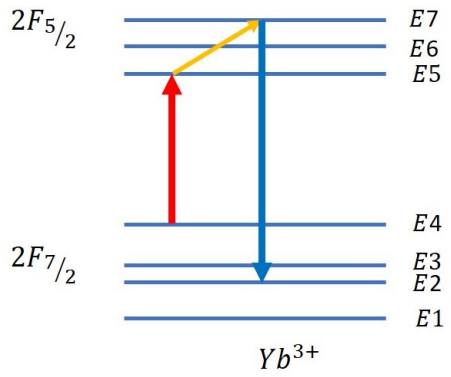

Figure 1.3. Scheme of optical refrigeration processes in Yb^{3+} doped glass.

with the lowest allowed excitation energy was sent into the system, and the excited electron gained extra energy by absorbing thermal vibration energy. Therefore, when the electron decayed radiatively, the energy of the emitted photon ε_{em} was higher than ε_{ex}, removing heat from the system. After Epstein *et al.*'s success, many attempts were carried out and succeeded with rare-earth-ion doped systems [12–20]. The most impressive work among them was carried out by Seletskiy in 2009 [21], where a cryogenic temperature of 155 K was achieved (starting from room temperature) in Yb^{3+} doped $LiYF_4$ crystal.

No implementation was successful in any other systems until 2012, when CdS nanobelts were cooled down by 40 K with laser excitation by Jun Zhang *et al.* [22]. This was the first time OR was achieved in semiconducting nanomaterials. The authors pointed out that excitons and longitudinal optical phonons (LOPs) are strongly coupled in CdS nanobelts, leading to multi LOPs resonant annihilation in UCPL re-

moving more than an ε_{lop} for each cooling cycle, where ε_{lop} is the energy of a single LOP. Thus a much larger cooling effect is observed in CdS nanobelts, which should be also applicable in other II-VI semiconducting nanomaterials. Their results showed the possibility of OR in other semiconducting nanomaterials, inspiring our research based on realizing OR in semiconducting quantum dots (QDs).

Semiconducting QDs are well known for their optical properties [23], *i. e.* quantization of the absorption spectra and size-tunable energy band gap among others. These phenomena allow wide applications of semiconducting QDs in light emitting and photovoltaic devices [24–26]. Realizing OR in QDs would provide a non-contact cooling technique for existing QD devices. Furthermore, providing cooling materials with tunable absorption and emission energy would significantly broaden the possible light sources for OR application. Besides being a natural extension to the work done in CdS nanobelts, QDs would provide a much more versatile platform for OR, such as suspensions in a solid matrix. In our research, CdSe/CdS (core/shell) QDs have been selected as the active components to look for QD based OR. Their emission spectra cover the entire visible range, allowing, in principle, realizing OR under sunlight (requires proper filters to create quasi-monochromatic light).

1.2 Criteria of optical refrigeration in solids

From an energy point of view, a net up-conversion in the PL mean emission energy is required for a system to achieve OR. For example, in neutral atoms gas systems and CO_2 gas system [27], the energy up-conversion is achieved by Doppler effect and molecular collisions respectively.

In a solid system, the source of the energy up-conversion originates from thermal vibration modes (*i. e.* phonons in systems with translational invariance). Therefore, for OR in a solid system to be possible, phonons must be coupled to the PL processes. However, the coupling strength of creating or annihilating a phonon is identical, while creation processes are thermodynamically much more favored, producing energy

down-conversion PL (DCPL), which is a heating process. This fact requires the system to have a discontinuity in its electronic energy structure, in other words, a gap between the ground and excited states. Therefore, by monochromatically exciting electrons to the edge of the excited states or band, DCPL processes are prohibited due to the lack of available states. Excitons may also recombine purely non-radiatively through the creation of phonons, in which all absorbed photon energy would be transferred into heat. To eliminate such non-radiative decay processes, the energy gap needs to be much larger than the cut-off energy of the phonons (only higher order processes are energetically allowed, which are much less likely to occur). On the other hand, if the excitonic non-radiative decay rate is not zero, the re-absorption of emitted photons will statistically increase the probability of excitons recombining non-radiatively, leading to a net heating effect. Meanwhile, if the photon being absorbed was emitted through the energy up-conversion process, which energy is higher than the excitation energy, the condition of lack of available states no longer holds, leading to a redshift in the emission spectra, reducing the cooling effect. Therefore, the geometry of the system needs to be tailored to minimize re-absorption. Consequently, the thermal energy removed from the system by each OR process would be very limited comparing to the excitation energy, further requiring the elimination of excitonic non-radiative decay processes.

PL quantum yield (QY) η is introduced to describe the likelihood of an exciton to decay radiatively, which is defined as the ratio of the number of photons emitted over the number of the photons absorbed by the system. So, $\eta \rightarrow 1$ is crucial for a material to achieve OR. A well-known system satisfying such criterion is the rare-earth-ion doped glass mentioned in section 1.1. In such system, the active component, rare-earth-ions, is poorly coupled to the phonons modes in the glass substrate [17], prohibiting non-radiative decay processes. On the other hand, since most of the cooling substance is made of an inactive component, the glass matrix, background absorption becomes an important heating mechanism. Therefore, the matrix material

needs to be transparent to the excitation light, with negligible defect concentration, perfect uniformity and purity.

As a conclusion, the criteria of achieving OR in a system are: very high quantum yield (almost unity), energy up-conversion and negligible background absorption.

Quantitative evaluation of the possibility of realizing OR in solids can be done by calculating the cooling efficiency η_{c}. Here η_{c} is defined as

$$\eta_{\mathrm{c}} = \frac{P_{\mathrm{c}}}{P_{\mathrm{in}}}, \tag{1.7}$$

where P_{c} denotes the net optical power removed from the system (bear in mind, it could be negative), and P_{in} denotes the total optical power absorbed by the system (light scattering is not considered, as it introduces no net energy exchange with the system). These two values are directly related to the excitonic population N. Under optical excitation, the rate of change of N is given by [17]

$$\frac{dN}{dt} = \frac{\alpha I}{\varepsilon_{\mathrm{ex}}} - k_{\mathrm{nr}}N - k_{\mathrm{r}}N + (1-\eta_{\mathrm{es}})k_{\mathrm{r}}N,$$

where α and I are the absorption coefficient and the intensity of the excitation light respectively (laser spectra can be considered monochromatic when compared to the PL signal width), k_{nr} is the nonradiative decay rate (including Auger processes, in which carriers are ionized by multi-photon absorption, a non-linear processe); k_{r} is the radiative decay rate and η_{es} is the luminescence escape efficiency. α, k_{r} and k_{nr} are ε_{ex}, N and temperature dependent. It is important to point out that η_{es} is averaged over the entire PL spectrum. The term $(1-\eta_{\mathrm{es}})k_{\mathrm{r}}N$ represents the net re-absorption, giving an effective radiative decay rate of $\eta_{\mathrm{es}}k_{\mathrm{r}}N$. Accordingly,

$$P_{\mathrm{in}} = (\alpha + \alpha_{\mathrm{b}})I, \tag{1.8}$$

where, α_{b} is the background absorption rate, and

$$P_{\mathrm{c}} = \eta_{\mathrm{es}}k_{\mathrm{r}}N\varepsilon_{\mathrm{em}} - \alpha I. \tag{1.9}$$

In steady state, $\frac{dN}{dt} = 0$, the total excitonic decay rate is equal to the total photon absorption rate (not including the back ground absorption),

$$\frac{\alpha I}{\varepsilon_{\mathrm{ex}}} = (k_{\mathrm{nr}} + \eta_{\mathrm{es}}k_{\mathrm{r}})N.$$

Thus, the effective quantum efficiency for light emission η_{eff} can be defined as the effective total radiative decay rate over the total excitonic decay rate

$$\eta_{\text{eff}} = \frac{\eta_{\text{es}} k_{\text{r}}}{(k_{\text{nr}} + \eta_{\text{es}} k_{\text{r}})}. \tag{1.10}$$

According to Eq. 1.7, 1.8, 1.9 and 1.10,

$$\eta_c = \eta_{\text{eff}} \frac{1}{(1 + \alpha_{\text{b}}/\alpha)} \frac{\bar{\varepsilon}_{\text{em}}}{\varepsilon_{\text{ex}}} - 1. \tag{1.11}$$

Here $\bar{\varepsilon}_{\text{em}}$ is the PL mean emission energy. To realize OR, η_{c} must be positive, requiring the values of η_{eff}, $\frac{1}{1+\alpha_{\text{b}}/\alpha}$ and $\frac{\bar{\varepsilon}_{\text{em}}}{\varepsilon_{\text{ex}}}$ to be as large as possible. In an ideal system, where η approaches unity, or $k_{\text{nr}} \to 0$, $\eta_{\text{eff}} \approx \eta \to 1$. $\frac{1}{1+\alpha_{\text{b}}/\alpha}$ reaches unity when $\alpha_{\text{b}} \to 0$. Therefore, $\frac{\bar{\varepsilon}_{\text{em}}}{\varepsilon_{\text{ex}}}$ must be larger than one. However as mentioned earlier in this section, if $\frac{\bar{\varepsilon}_{\text{em}}}{\varepsilon_{\text{ex}}}$ is too large, it favors the non-radiative decay processes, leading to a smaller η_{eff} value. The optimized condition is determined by the competing result between η_{eff} and $\frac{\bar{\varepsilon}_{\text{em}}}{\varepsilon_{\text{ex}}}$.

In semiconducting materials, their QY is typically not perfect due to the excitonic non-radiative decay paths introduced by bulk and surface defects [28], while strong re-absorption in semiconducting materials makes the situation even worse. An advantage of using semiconducting QDs is that the re-absorption processes are suppressed as the QDs' size is typically much smaller than the depletion depth for the excitation light. On the other hand, the energy gap between their conduction and valence bands provides the possibility of achieving up-conversion in the PL mean emission energy. Semiconducting materials also provide a much higher density (larger PL cross-section) of active component compared to the rare-earth-ion systems, potentially producing a much higher cooling power. Therefore, seeking powerful cooling mechanism and perfecting PL QY, requires a deep understanding of the materials' physical properties and its connection with synthesis procedures.

1.3 Semiconducting quantum dots

The basic physics of semiconducting QDs can be understood by the "particle-in-a-box" model, where a QD is considered as a box with infinite potential walls at its boundary. When a particle is trapped inside a box and its natural length scale is comparable to the box's size, it experiences strong spatial confinement, leading to discrete energy states. In semiconducting materials, a properly tuned excitation can promote an electron into the conduction band, leaving a hole in the valence band. This electron and hole pair, also known as an exciton, can be treated as a hydrogen-like particle. Therefore, its spatial length scale can be characterized by its excitonic Bohr-radius r_b. Using the effective-mass approximation [29],

$$r_b = \frac{m_0}{m_*} r_a. \tag{1.12}$$

Here r_a is the Bohr radius for hydrogen atoms, m_0 is the mass of a free electron and m_* is the reduced effective-mass of the exciton, defined as [30]

$$m_* = \frac{m_e^* m_h^*}{m_e^* + m_h^*}. \tag{1.13}$$

Where m_e^* and m_h^* denote the effective-mass of the electron and hole in the material respectively. Hence, when the size of the QD is smaller than the excitonic Bohr-radius, the exciton experiences strong spatial confinement. As shown in figure 1.4, the allowed energy states for electron and hole in the conduction and valence band respectively become discrete, leading to an atomic-like energy spectrum. Another direct consequence of the confinement is the increase of the energy band gap, where the bottom(top) of the conduction(valence) band is increased(decreased) from its original value. Therefore, the effective energy band gap, $\varepsilon_{\mathrm{g}}^{\mathrm{eff}}$ of the QDs is larger than the intrinsic value for the bulk material, ε_{g}. The smaller the size of QDs, the larger the energy band gap will be, leading to tunable absorption and emission energies.

The production of QDs can be tracked back to a very early age in human history, a well known example is stained glass. It is produced by diluting gold, silver or other materials into the melted glass, resulting in the formation of nanocrystals (or

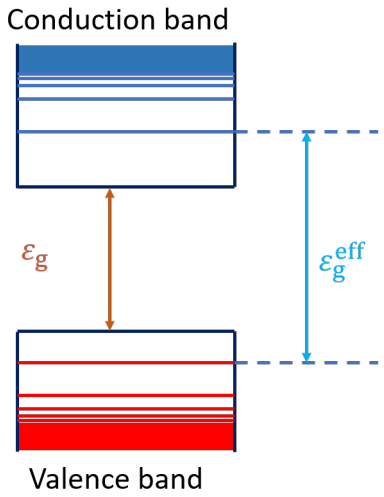

Figure 1.4. Discrete energy levels in semiconducting quantum dots due to spacial confinement.

microcrystals), while the size of them is determined by the concentration. The first QDs sample made in the lab was synthesized by Ekimov [31] in 1979, embedding small semiconducting crystals into glass matrices. The synthesis method was similar to the "ancient" version, resulting in great uncertainty of the QD's size distribution [32]. Shortly after, in 1982, the first physics model to describe QDs systems was developed by Efros [33], Ekimov's student at the time. The name of QDs was given by Reed *et al.* [34]in 1985. Many of QDs's optical properties are inherited from the bulk material, while the size dependent energy gap leads to tunable absorption and emission spectra, attracting significant interest from researchers. However, early studies of QDs were limited by their poorly controlled size distribution and crystalline structure. Details of the electronic structure inside QDs could not be derived with large ensembles, which give wide ($>$ 100 meV) absorption and PL spectra [23].

The situation was dramatically improved by Murray *et al.* in 1992 [35], more specifically, the "hot injection" method developed by their research. The idea is to create super-saturation of the QDs' precursors during a standard wet-chemical synthesis by rapidly injecting excessive amounts of one or all of the precursors at

the reaction temperature. By doing so, the nucleation processes (precipitation of crystal monomers) is initiated over the entire solution at almost the same time [36, 37]. As the precursors are being rapidly consumed, accompanied by a decrease in temperature, the nucleation processes is terminated. Since all monomers are nucleated approximately simultaneously and growth is terminated uniformly across the sample, an almost monodispersed size distribution of the QDs is obtained. Murray's method revealed the principle of the production of monodispersed QDs samples: nucleation processes of QDs must be initiated and terminated simultaneously across the whole sample. Nowadays commercial QDs samples with typical size dispersion lower than 5% are available.

The "hot injection" method, however, also has its disadvantages. One of the issues is the high temperatures used for injection (typically around $350-380\,^{\circ}\mathrm{C}$) and growth (typically around $300-350\,^{\circ}\mathrm{C}$). Although it requires a much lower temperature than diluting materials into melted glass, the organic solvents involved in the synthesis, make the procedure relative dangerous. The high temperature also leads to a rapid growth rate, making the dots more vulnerable to structural defects. The injection process itself requires a uniform spreading of the precursor inside the reaction mixture, making it difficult to scale up for massive production.

New synthesis methods developed in the last decades for growing CdSe QDs with zinc-blende crystal structure provide an alternative choice. It has been achieved by different groups [1,38–40] in the non-coordinating solvent octadecene [41]. Unlike the regular procedure to produce high quality CdSe QDs with wurtzite crystal structure [35, 42], in which the hot-injection of precursors is required, the synthesis of the zinc-blende CdSe QDs is performed with a moderate reaction speed at a much lower temperature. The reaction speed can be further slowed down by reducing the reaction temperature or increasing the length of the corresponding binding ligands. Benefiting from the slow reaction speed of this method, massive production of CdSe QDs with almost no inner crystalline defects can be achieved in zinc-blende CdSe QDs [43].

1.3.1 Zinc-blende CdSe quantum dots

CdSe QDs have attracted great amount of interest from researchers in recent decades due to their novel optical properties [24, 44–48]. Zinc-blende is one of the crystalline structures available for bulk CdSe, with an energy band gap of 1.65 eV at room temperature [49]. By adjusting the size of CdSe QDs from 0.5 nm to 5 nm [50] CdSe QDs' emission energy can be tuned through the whole visible range. However, early production of CdSe QDs usually ended up with wurtzite structure, another stable crystalline structure favored at a higher temperature ($> 96\,^{\circ}\mathrm{C}$ [51]), while the zinc-blende structure might appear as stacking defects (the only structural difference between the wurtzite and zinc-blende CdSe crystals is the stacking sequence of the CdSe hexagonal layers). In fact, the synthesis of CdSe QDs starts with zinc-blende crystalline cores, and a phase transition takes place during the growth processes at high temperature [52, 53]. Such phase transition requires shifting of the stacking layers, which can be stopped by using a lower synthesis temperature or adding tighter binding ligands [54, 55]. Consequently, the synthesis of zinc-blende CdSe QDs is performed with a moderate reaction speed, favoring the production of the perfect inner crystal structure. In addition, different from the wurtzite structure, the aspect ratio of the zinc-blende structure is one, providing isotropic optical properties and a simpler electronic structure, which simplifies the evaluation of their cooling capability. Therefore, CdSe QDs with zinc-blende crystal structure was selected as the active component in our research.

Surface effects on CdSe QDs are not significantly altered by its crystal structure. The big surface curvature owing to the small QD size introduces a significant amount of surface defects (dangling atoms and lattice vacancies) on the surface of QDs. These defects provide substantial non-radiative decay paths for excitons [56], hampering the QD's QY. Hence, bare CdSe QDs usually have a very low QY (typically lower than 10%). To bring the QY of the CdSe quantum dots close to unity, surface treatments which passivate the surface defects must be performed, such as the growth of an

inorganic shell and attaching molecular ligands onto the QDs' surface. In our case, where an extremely high QY is needed, both methods were applied.

1.4 Surface treatment on CdSe QDs

1.4.1 Surface passivation with CdS shell

Passivating the surface of QDs with inorganic materials has been well studied for decades. The idea of the method is to grow one or multiple layers of an inorganic material, different from the one of the original dots, with a wider energy gap. Incomplete crystal sites can be passivated (form complete crystal bonds) by atoms in the shell, while the potential barrier introduced by the wider energy gap prevents excitons from reaching the new surface. On the other hand, the newly grown shell should have a similar lattice structure to the QDs' material to ensure the complete passivation of surface defects and minimize the stress at the interface, such that the dots do not crack. For the case of CdSe QDs, CdS is one of the most popular coating materials. Because of the similar lattice constants between CdSe and CdS (0.6 nm and 0.58 nm for CdS and CdSe in their zinc-blende structure), the likelihood of introducing defects at the boundary between these materials is greatly reduced. For the same reason, more complete passivation of the surface structure should also be expected. On the other hand, the conduction(valence) band of CdS is higher(lower) than the one of CdSe, precluding the exciton to reach the surface of the shell, where defects may also occur. Recent investigations indicate that holes can still be effectively trapped by the surface defects on the CdS shell. To remove these surface hole-traps, other passivation techniques are required.

1.4.2 Surface passivation with ligands

One effective method to eliminate surface hole-traps on CdS shell is capping it with molecular ligands. Such method is widely used in colloidal QDs, since they are

automatically mixed with molecular ligands as the precursors and surfactants used in the synthesis are in the form of metal-organic compounds (a group of chemical compounds formed by metal ions and organic ligands complex). Typically, the surface of QDs are attached by the ligands' polar head groups [37,57], while the non-polar tails are facing the organic solvent, providing stability of the colloid. Therefore, surface properties of QDs can be modified as desired by adding specific ligands. To ensure the complete coverage of surface ligands, most QDs were designed to be finished with either all positive ions or all negative ions. For example in the CdS shell, to eliminate hole-traps, the QDs are finished with Cd^{2+}, and phosphine or amine or both groups are used to cap the surface. However, experimentally, a very limited but not zero negative ions sites (S^{2-}) may remain on the surface. So, to guarantee the complete passivation, a newly proposed solution is coating the QDs with short chain Cd-carboxylate monomers [1]. It must be pointed out that ligands are vulnerable to oxidation, hence specific storage method (*i. e.* inert gas protection) is required. Very recently, synthesis with almost unity QY has been achieved for zinc-blende [2] structures CdSe QDs after complete surface passivation, enhancing the possibility of realizing OR on them. Thus, zinc-blende CdSe QDs were selected to be the cooling materials in our research. In order to achieve OR, discovering and optimizing the possible cooling mechanism in zinc-blende CdSe QDs needs to be carried out.

1.5 Cooling mechanism in CdSe QDs

Although there is no translational invariance in QDs, the lattice structure should be close to the bulk material. Therefore, LOPs may couple to PL processes through Fröhlich interactions, while acoustic phonon coupling could still happen through deformation potential and piezoelectric potential [58–61]. In addition, because the surface to volume ratio is huge in QDs, while the PL processes in CdSe QDs were suggested to be intrinsically related to the surface electronic states [62], surface phonon modes, which are typically ignored in bulk materials, might significantly couple to

the PL processes. Therefore, possible up-conversion in the PL mean emission energy could be achieved by phonon-annihilation coupled PL processes. Different to CdSe bulk materials, in which phonons strongly couple to the PL processes with a Huang-Rhys factor, $S \approx 10$ [63] ($S = \frac{1}{2}\omega^2\vec{u}^2/\hbar\omega$, where $\vec{u}$ denotes the displacement of the normal coordinate of phonon modes caused by the exciton, and ω is the angular frequency of the phonon [64, 65]), S is typically more than 20 folds weaker in CdSe QDs [63,65]. Although the weak phonon-excitonic coupling strength does not hurt the cooling effect (discussed in section 1.2), the CdSe QDs system might be restricted to only have single-phonon-coupled PL processes. Accordingly, up-conversion in CdSe QDs' PL mean emission energy might be achieved though single-LOP-annihilation coupled PL processes. With the purpose of evaluating and optimizing the cooling effect, a quantitative model needs to be developed and tested to give reliable predictions in the PL spectra of the sample with different parameters, such as temperature and excitation energy.

2. THEORETICAL CALCULATIONS

Towards realizing OR on CdSe/CdS (core/shell) quantum dots, quantitative calculation of the cooling efficiency is important and necessary for designing the sample synthesis, defining testing projects and construction of the experimental setup.

The calculation of the electronic structure of our QDs samples will be discussed first to understand their PL mechanism including possible cooling mechanisms. Following that, estimation of the photon absorption and emission rates, especially with the phonon-assisted process taken into account will be presented. These two sections will also reveal the limitations of existing theoretical models, introducing the motivation of developing a semi-empirical model, which will be discussed in the third section. Then, a complete calculation of cooling efficiency and cooling power of our samples under plausible conditions (*i. e.* different QYs and background absorption rates) will be illustrated. The possible thermal conduction through the environment will be shown in the last section, giving an indication of the maximum temperature drop that can be observed in OR experiments.

2.1 Size dependent energy band gap of QDs

The effective energy band gap determines the absorption edge of QDs samples. Its value is mainly defined by the intrinsic energy band gap of the material and the quantization in both conduction and valence bands due to the spatial confinement. In our research, it is calculated using the "particle-in-a-box" model with the well-known effective-mass approximation [66, 67]. Due to the almost spherical symmetry of the dots, we will call the model "particle-in-a-sphere".

2.1.1 Quantization of electronic states in QDs

In the "particle-in-a-sphere" model, the carriers inside the QDs are treated as free particles by introducing the effective-mass approximation [66, 67]. The idea is that the crystal structure of the QDs is treated to be identical to the bulk material, and the Bloch theorem remains valid. Therefore, the electronic wavefunction Φ in a QD is

$$\Phi(\vec{r}) = U(\vec{r})\psi(\vec{r}), \tag{2.1}$$

where, $U(\vec{r})$ is the periodic Bloch function, and $\psi(\vec{r})$ is the envelope function which satisfy boundary conditions. For colloidal QDs, the envelope function can be solved by considering the carriers being confined in a potential well with spherical symmetry. In the case of zinc-blende CdSe/CdS QDs, the radial potential energy is illustrated in figure 2.1, in which the intrinsic band gap value and the offsets between the CdSe and CdS are obtained from reference [49]. Because of the confinement potential, the

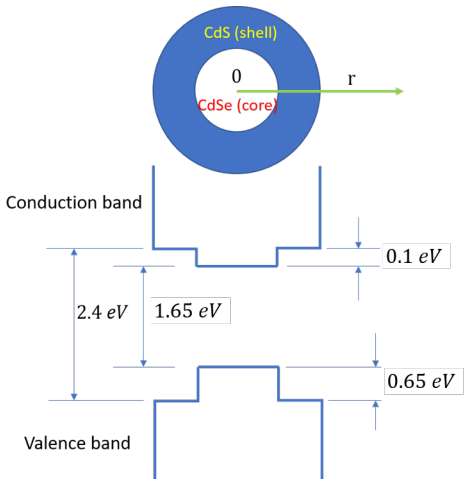

Figure 2.1. Electronic energy structure of CdSe/CdS quantum dots in zinc-blende structure.

electronic energy levels allowed in the bands are discrete levels [68]. The modified band gap is determined by the energies at the bottom of the conduction band (c) and the top of the valence band (v). The Hamiltonian of the electron (e)/hole (h)

Table 2.1.
Effective masses used in the calculation. m_0 is the electron's rest mass.

Material	electron effective mass	heavy hole effective mass
CdSe	$0.11\,m_0$	$0.8\,m_0$
CdS	$0.14\,m_0$	$0.51\,m_0$

(indicated by the subscripts) in the conduction/valence (indicated in the superscripts) band is,

$$\mathcal{H}_{e/h}^{c/v} = -\hbar^2 \nabla \frac{1}{m_{e/h}^{c/v}} \nabla + V^{c/v}(r). \tag{2.2}$$

Here $m_{e/h}^{c/v}$ is the electron/hole's effective mass in the conduction/valence band. $V^{c/v}(r)$ denotes the confinement potential of the conduction/valence band. Since the unit cell of the zinc-blende structure has face-centered cubic symmetry, a single value of electron effective mass is used. On the other hand, our research only involves sub-band edge excitation. Therefore, only the heavy hole values were used for the calculation in each band. The values of electrons' and holes' effective masses used in the calculation are listed in table 2.1 [69].

The problem is solved independently for electrons and holes. For electrons energy is measured from the bottom of the conduction band. For holes, it is measured from the top of the valence band. Assuming the bottom(top) of the conduction(valence) band to be at zero potential, and a "hard" potential at the shell-vacuum boundary,

$$V^{c/v} = \begin{cases} 0 & for \quad r \leq r_{\text{core}} \\ V_{\text{shell}}^{e/v} & for \quad r_{\text{core}} < r > r_{\text{shell}} \\ \infty & for \quad r \geq r_{\text{shell}} \end{cases}$$

where r_{core} and r_{shell} is the radius of the core and shell respectively, $V_{\text{shell}}^{c/v}$ is the potential energy of the shell material's conduction/valence band measured with respect to that of the core. The solution of the Schördinger equation,

$$\mathcal{H}_{e/h}^{c/v} \psi_{e/h}^{c/v} = \varepsilon_{e/h}^{c/v} \psi_{e/h}^{c/v}, \tag{2.3}$$

is a combination of spherical Bessel functions and spherical harmonic functions,

$$\psi_{e/h}^{c/v} = [\mathcal{A}_{e/h,l,m}^{c/v} j_l(k_{e/h,l,m}^{c/v} r) + \mathcal{B}_{e/h,l,m}^{c/v} n_l(k_{e/h}^{c/v} r)]\, Y_l^m(\theta, \varphi), \tag{2.4}$$

where j_l and n_l are the spherical Bessel functions of the first and second kinds respectively. Y_l^m are the spherical harmonic functions. $k_{e/h}^{c/v}$ are given by,

$$k_{e/h}^{c/v} = \sqrt{\frac{2(\varepsilon_{e/h}^{c/v} - V^{c/v}) m_{e/h}^{c/v}}{\hbar^2}} \tag{2.5}$$

Where $\varepsilon_{e/h}^{c/v}$ denotes the energy of the electron/hole. Because n_l diverges at the origin, the radial wavefunction in the core is,

$$\psi_{e/h}^{c/v,\text{core}} = \mathcal{A}_{e/h,l,m}^{c/v,\text{core}} j_l(k_{e/h,l}^{c/v,\text{core}} r). \tag{2.6}$$

In the shell,

$$\psi_{e/h}^{c/v,\text{shell}} = \mathcal{A}_{e/h,l,m}^{c/v,\text{shell}} j_l(k_{e/h,l}^{c/v,\text{shell}} r) + \mathcal{B}_{e/h,l,m}^{c/v,\text{shell}} n_l(k_{e/h,l}^{c/v,\text{shell}} r). \tag{2.7}$$

The energy levels and the normalization coefficients can be obtained by applying boundary conditions

$$\psi_{e/h}^{c/v,\text{core}}|_{r=r_\text{core}} = \psi_{e/h}^{c/v,\text{shell}}|_{r=r_\text{core}}, \tag{2.8}$$

$$\frac{1}{m_{e/h}^{c/v,\text{core}}} \frac{\partial}{\partial r} \psi_{e/h}^{c/v,\text{core}}|_{r=r_\text{core}} = \frac{1}{m_{e/h}^{c/v,\text{shell}}} \frac{\partial}{\partial r} \psi_{e/h}^{c/v,\text{shell}}|_{r=r_\text{core}}, \tag{2.9}$$

$$\psi_{e/h}^{c/v,\text{shell}}|_{r=r_\text{shell}} = 0. \tag{2.10}$$

By applying Eq. 2.6 and 2.7 to Eq 2.8 and 2.9, the constants $\mathcal{A}_{e/h,l,m}^{c/v,\text{shell}}$ and $\mathcal{B}_{e/h,l,m}^{c/v,\text{shell}}$ can be obtained

$$\mathcal{A}_{e/h,l,m}^{c/v,\text{shell}} = \frac{j_l(k_{e/h,l,m}^{c/v,\text{core}} r_\text{core}) n_l'(k_{e/h}^{c/v,\text{shell}} r_\text{core}) - \frac{m_{e/h}^{c/v,\text{shell}} k_{e/h,l,m}^{c/v,\text{core}}}{m_{e/h}^{c/v,\text{core}} k_{e/h,l,m}^{c/v,\text{shell}}} j_l'(k_{e/h,l,m}^{c/v,\text{core}} r_\text{core}) n_l(k_{e/h}^{c/v,\text{shell}} r_\text{core})}{j_l(k_{e/h,l,m}^{c/v,\text{shell}} r_\text{core}) n_l'(k_{e/h}^{c/v,\text{shell}} r_\text{core}) - j_l'(k_{e/h,l,m}^{c/v,\text{shell}} r_\text{core}) n_l(k_{e/h}^{c/v,\text{shell}} r_\text{core})} A_{e/h,l,m}^{c/v,\text{core}}, \tag{2.11}$$

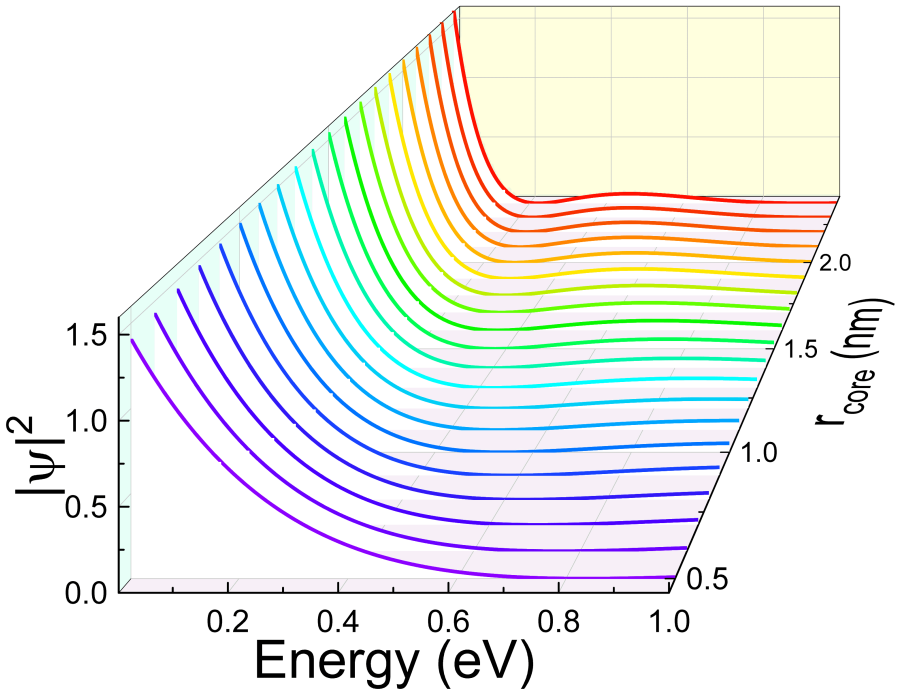

Figure 2.2. Probability density of the electron on the shell boundary (conduction band) versus energy. A shell thickness of 1.4 nm (4 layers of CdS) were used in the calculation to derive the plots.

$$\mathcal{B}^{c/v,\text{shell}}_{e/h,l,m} = \frac{j_l(k^{c/v,\text{core}}_{e/h,l,m} r_{\text{core}}) j_l'(k^{c/v,\text{shell}}_{e/h} r_{\text{core}}) - \frac{m^{c/v,\text{shell}}_{e/h} k^{c/v,\text{shell}}_{e/h,l,m}}{m^{c/v,\text{core}}_{e/h} k^{c/v,\text{shell}}_{e/h,l,m}} j_l'(k^{c/v,\text{core}}_{e/h,l,m} r_{\text{core}}) j_l(k^{c/v,\text{shell}}_{e/h} r_{\text{core}})}{j_l'(k^{c/v,\text{shell}}_{e/h,l,m} r_{\text{core}}) n_l(k^{c/v,\text{shell}}_{e/h} r_{\text{core}}) - j_l(k^{c/v,\text{shell}}_{e/h,l,m} r_{\text{core}}) n_l'(k^{c/v,\text{shell}}_{e/h} r_{\text{core}})} A^{c/v,\text{core}}_{e/h,l,m}. \tag{2.12}$$

Here $j_l' \equiv \frac{\partial j_l}{\partial r}$ and $n_l' \equiv \frac{\partial n_l}{\partial r}$. Since both $\mathcal{A}^{c/v,\text{shell}}_{e/h,l,m}$ and $\mathcal{B}^{c/v,\text{shell}}_{e/h,l,m}$ are expressed as functions of $\mathcal{A}^{c/v,\text{core}}_{e/h,l,m}$, for a QD with given r_{core} and r_{shell}, $\varepsilon^{c/v}_{e/h}$ can be determined through finding the smallest root of Eq. 2.10. Plots of $|\psi^c_e|^2_{r=r_{\text{shell}}}$ versus ε at different r_{core} and a fixed shell thickness of 1.4 nm (4 layers of CdS, the shell thickness of the samples for OR experiment) are shown in Fig. 2.2. As expected, the smallest root of Eq. 2.10 increases as r_{shell} decreases, while the electron's free particle energy is much higher than the hole's owing to a much lighter effective mass. Then, according to Eq. 2.6, 2.7, 2.11 and 2.12, $\mathcal{A}^{c/v,\text{core}}_{e/h,l,m}$ is determined by normalizing $\psi^{c/v}_{e/h}$.

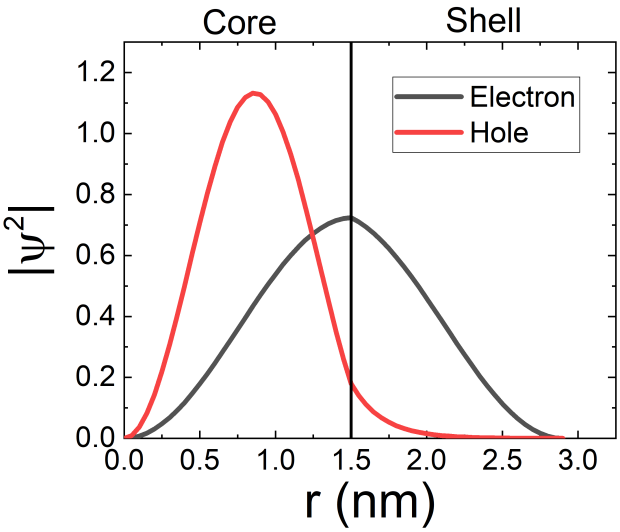

Figure 2.3. The probability density of the electron (black curve) and hole (red curve) in the conduction band and valence band respectively. $r_{\text{core}} = 1.5$ nm and $r_{\text{shell}} = 2.9$ nm were used in the calculation to derive the figure.

Typical probability density functions ($|\psi|^2$) of the electron and hole in a QD along the radial axis are shown in Fig. 2.3. Due to the shallow potential between the conduction bands of CdSe and CdS interface, the electron's probability density distribution heavily disperses into the CdS shell, while the hole is more confined at the CdSe core as the potential barrier the two materials' valence bands is more significant.

However, such calculation might not be able to give accurate enough predictions of QDs' size-energy dependence. Due to the spatial confinement, the separation between the electron and hole inside QDs is much smaller than the case for bulk materials, leading to a significant increase in the Coulomb interaction energy between the two carriers. Therefore, corrections taking Coulomb interaction energy into account are needed.

2.1.2 Coulomb interaction energy

In the case of QDs, due to their small size, the overlap between the electron's and hole's wavefunctions is significant, the effect introduced by Coulomb interaction is not negligible. Correction was carried out by introducing the Hamiltonian for the Coulomb interaction $\mathcal{H}_{\mathrm{C}}$,

$$\mathcal{H}_{\mathrm{C}} = -\frac{1}{4\pi\epsilon(\vec{r})}\frac{e^2}{r_{e-h}}, \tag{2.13}$$

where ϵ is the dielectric constant of the material and $e = 1.6 \times 10^{-19}\,\mathrm{C}$ is the unit charge. r_{e-h} denotes the spatial distance between the electron and hole inside QDs, given by

$$r_{\mathrm{e\text{-}h}} = |\vec{r}_{\mathrm{e}} - \vec{r}_{\mathrm{h}}|, \tag{2.14}$$

where $\bar{r}_{\mathrm{e}}$ and $\bar{r}_{\mathrm{h}}$ denote the coordinates of the electron and hole respectively. $\mathcal{H}_{\mathrm{C}}$ is considered as the perturbation of the intrinsic electronic Hamiltonian, and its appropriateness evaluated *a posteriori* by comparing the size of the correction to the single particle level. Here the Dirac brackets are introduced to simplify the notation, where $|\Phi_{e/h}^{c/v}\rangle$ is the corresponding electronic state, while the excitonic states is described as $|\Phi_{\mathrm{e}}^{\mathrm{c}}\rangle|\Phi_{\mathrm{h}}^{\mathrm{v}}\rangle$, the product of the electron and hole states. $\langle\Phi_{e/h}^{c/v}|\Phi_{e/h}^{c/v}\rangle$ denotes the inner product of the wavefunctions. The Coulomb interaction energy ε_{C} is given by

$$\varepsilon_{\mathrm{C}} = \langle\Phi_{e}^{c}|\langle\Phi_{\mathrm{h}}^{v}|\mathcal{H}_{\mathrm{C}}|\Phi_{e}^{c}\rangle|\Phi_{\mathrm{h}}^{v}\rangle.$$

The calculation result is shown in Fig. 2.4, where the Coulomb interaction energy is small compared to the energy of the carriers especially for the QDs with smaller size. The wavefunction $\Phi_{e/h}^{c/v}$ with corrected effective energy band gap is used to calculate the electronic transition rates of our samples and provide a reference for our synthesis. Therefore, the effective energy band gap of the QDs with Coulomb interaction correction is,

$$\varepsilon_{\mathrm{g}}^{\mathrm{eff}} = \varepsilon_{\mathrm{g}} + \varepsilon_{\mathrm{e}}^{\mathrm{c}} + \varepsilon_{\mathrm{h}}^{\mathrm{v}} + \varepsilon_{\mathrm{C}}. \tag{2.15}$$

As shown in Fig. 2.5, $\varepsilon_{\mathrm{g}}^{\mathrm{eff}}$ increased monotonically as the size of the dot decreases. Because the typical core size of reported high quality (unity QY) CdSe/CdS QDs [1,2]

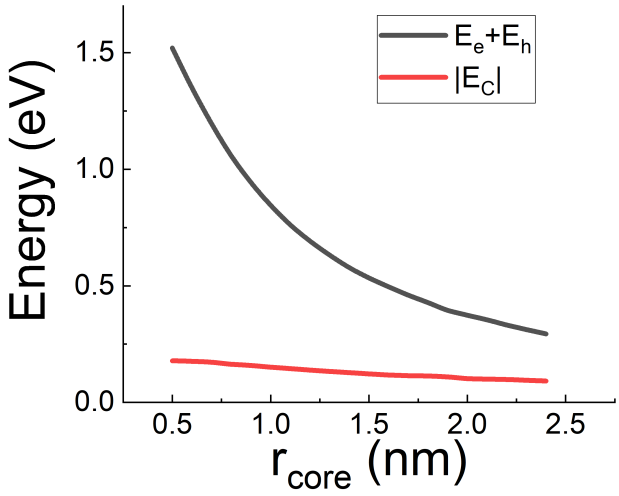

Figure 2.4. Coulomb interaction energy (red curve) between the electron and hole comparing to their total energy (black curve). A fixed shell thickness of 1.4 nm was used in the calculation to obtain the figure.

is within the range of $1.5 - 1.75$ nm, the proper laser energy to provide sub-band excitation needs to be in the $1.9 - 2.0$ eV range.

2.2 Electronic band edge transition

According to section 1.2, the cooling efficiency η_c for OR is proportional to the term $\frac{1}{1+\alpha_b/\alpha}$. Hence, maximization of η_c is benefited by a bigger absorption rate α at fixed α_b. On the other hand, the maximum cooling power is proportional to the QDs' PL emission rate, which determines the maximum number of cooling cycles achieved in a QD per unit time. In an OR process, as the excitation energy is close to the effective energy band gap, both the photon absorption and emission processes can be considered as excitonic band edge transitions. Therefore, quantitative calculation of the band edge transition rate with optical excitation is essential for our research.

The band edge transition probability due to photon absorption can be calculated by treating QDs as a two-level system with the ground state, $|\Phi_e^v\rangle|\Phi_h^v\rangle$ (both the

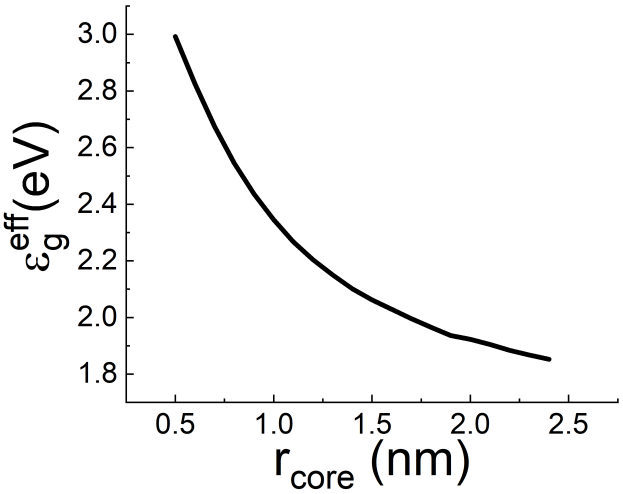

Figure 2.5. Calculated effective energy gap $\varepsilon_{\mathrm{g}}^{\mathrm{eff}}$ of CdSe QDs with respect to the core radius r_{core}. A shell thickness of 1.4 nm (4 layers of CdS) were used in the calculation.

electron and hole are at the top of the valence band) and the excited state, $|\Phi_e^c\rangle|\Phi_{\mathrm{h}}^v\rangle$ (the electron is at the bottom of the conduction band, while the hole is left at the top of the valence band). Here, $|\Phi_{\mathrm{e}}^{\mathrm{v}}\rangle$ is not derived from the "particle-in-a-sphere" model, and it is identical to $|\Phi_{\mathrm{h}}^{\mathrm{v}}\rangle$, equivalent to having no free carriers, which is the ground state. The Hamiltonian of the electrons in the QDs within the external radiation field (light) is

$$\mathcal{H}_e = \frac{1}{2m_{\mathrm{e}}^*}(\vec{p} - e\vec{A})^2 + V, \tag{2.16}$$

where $\vec{A}$ is the vector potential of the light, $\vec{p}$ is the momentum operator and V denotes the potential energy. Expanding the kinetic energy term in Eq. 2.16 gives,

$$\mathcal{H}_{\mathrm{e}} = \frac{\vec{p}^2}{2m_e^*} + V + \frac{e}{2m_e^*}(\vec{p}\cdot\vec{A} + \vec{A}\cdot\vec{p}) + \frac{e^2A^2}{2m_e^*}. \tag{2.17}$$

In our calculation, the intensity of the excitation light was limited purposely to avoid multi-photon absorption. Therefore, the contribution of the A^2 term is even smaller than the $\bar{A}\cdot\bar{p}$ one and considered to be negligible. The cross terms left were treated

as a perturbation, $\mathcal{H}_{\text{e-R}}$ to the unperturbed electronic Hamiltonian $\mathcal{H}_0 = \frac{\vec{p}^2}{2m_e^*} + V$. Introducing the Coulomb gauge condition gives

$$\vec{p} \cdot \vec{A} = \vec{A} \cdot \vec{p}. \tag{2.18}$$

Therefore,

$$\mathcal{H}_e = \mathcal{H}_0 + \mathcal{H}_{e-R},$$

where,

$$\mathcal{H}_{e-R} = \frac{e}{m_e^*} \vec{A} \cdot \vec{p}.$$

By defining $\vec{A} = A_0 \hat{a} e^{-i(\vec{k}\cdot\vec{r} - \omega t)}$, where A_0 and $\hat{A}$ are the amplitude and direction of $\vec{A}$ respectively,

$$\mathcal{H}_{\text{e-R}} = H_{\text{e-R}} e^{-i\omega t}$$

where

$$H_{\text{e-R}} = \frac{eA_0}{m_{\text{e}}^*} \hat{A} e^{-i\vec{k}\cdot\vec{r}} \cdot \vec{p}, \tag{2.19}$$

with i the imaginary number. Because in our application the size of QDs is much smaller than the wavelength of the light, the calculation can be further simplified by applying the dipole-approximation [61, 70],

$$e^{-i\vec{k}\cdot\vec{r}} \to 1.$$

By using the commutator relationship,

$$\vec{p} = \frac{im_{\text{e}}^*}{\hbar} (\mathcal{H} \cdot \vec{r} - \vec{r} \cdot \mathcal{H}),$$

Eq. 2.19 can rewritten as

$$H_{\text{e-R}} \approx -e\vec{r} \cdot \vec{\mathcal{E}}, \tag{2.20}$$

where $\vec{\mathcal{E}}$ is the electric field of the incident light.

For the case of band edge excitation, the contribution from the perturbed terms of the excitonic wavefunctions is small comparing to the intrinsic terms. Therefore,

the rate of excitons being created from the ground state to the excited state with light excitation is given by first order time-dependent perturbation (TDP) [71],

$$\begin{aligned} R &= \frac{2\pi}{\hbar}\Big|\langle\Phi_{\mathrm{e}}^{\mathrm{v}}|\langle\Phi_{\mathrm{h}}^{\mathrm{v}}|\mathcal{H}_{e-R}|\Phi_{\mathrm{e}}^{\mathrm{c}}\rangle|\Phi_{\mathrm{h}}^{\mathrm{v}}\rangle\Big|^2\delta(\varepsilon) \\ &= \frac{2\pi\epsilon^2 e^2}{\hbar}\big|\langle\Phi_{\mathrm{e}}^{\mathrm{v}}|\langle\Phi_{\mathrm{h}}^{\mathrm{v}}|\vec{r}\cdot\vec{\mathcal{E}}|\Phi_{\mathrm{e}}^{\mathrm{c}}\rangle|\Phi_{\mathrm{h}}^{\mathrm{v}}\rangle\big|^2. \end{aligned} \tag{2.21}$$

Here $|\Phi_{\mathrm{e}}^{\mathrm{v}}\rangle|\Phi_{\mathrm{h}}^{\mathrm{v}}\rangle$ and $|\Phi_{\mathrm{e}}^{\mathrm{c}}\rangle|\Phi_{\mathrm{h}}^{\mathrm{v}}\rangle$ are the intrinsic excitonic wavefunctions of the ground state and excited state respectively. The steady state approximation has been used in Eq. 2.21. By recalling Eq. 2.1 from section 2.1.1, while applying the approximation that the envelope function varies slowly along QDs' radius, Eq. 2.21 becomes,

$$R = \frac{2\pi e^2\mathcal{E}^2}{\hbar}\big|\langle U_e^{\mathrm{c}}(\vec{r})|\epsilon\vec{r}|U_{\mathrm{h}}^{\mathrm{v}}(\vec{r})\rangle\langle\psi_{\mathrm{h}}^{\mathrm{v}}|\psi_{\mathrm{e}}^{\mathrm{c}}\rangle\big|^2. \tag{2.22}$$

A test was carried out by plotting the light power absorbed by QDs sample's (commercially purchased CdSe QDs with nominal diameter of 3.5 nm) versus laser incident power. As the intensity satisfies $I = \frac{1}{2}\epsilon_0 c\mathcal{E}^2$, the slope of the plot s is given by

$$s = \frac{4\pi n e^2}{ac\hbar\epsilon_0^2}\big|\langle U_e^{\mathrm{c}}(\vec{r})|\epsilon\vec{r}|U_{\mathrm{h}}^{\mathrm{v}}(\vec{r})\rangle\langle\psi_{\mathrm{h}}^{\mathrm{v}}|\psi_{\mathrm{e}}^{\mathrm{c}}\rangle\big|^2. \tag{2.23}$$

Here n is the number of the QDs within the light path, c is the speed of light, a is the effective area of the light spot and ϵ_0 is the vacuum permittivity. The experimental data is shown in Fig 2.6, where $s \approx 0.014$ was observed, while a calculated value of approximately 0.03 was derived from Eq. 2.23. Considering the approximations applied in the model, the model is able to provide acceptable results for estimation purposes. However, when estimating the spontaneous emission rate R_s of CdSe QDs, significant deviation between the calculation and experiments was observed. The formula of R_s is well documented [71]

$$R = \frac{4\pi\varepsilon_{\mathrm{g}}^3\epsilon^2}{\hbar^4 c^3\epsilon_0^2}\mathcal{D}, \tag{2.24}$$

where $\mathcal{D} = \big|\langle U_e^{\mathrm{c}}(\vec{r})|\vec{r}|U_{\mathrm{h}}^{\mathrm{v}}(\vec{r})\rangle\langle\psi_{\mathrm{h}}^{\mathrm{v}}|\psi_{\mathrm{e}}^{\mathrm{c}}\rangle\big|^2$ denotes the dipole moment of QDs. Since the energy of the emitted photon is identical to the effective energy band gap, $\varepsilon_{\mathrm{g}}^{\mathrm{eff}}$ is used as the photon energy term in the calculation. The result of QDs with size

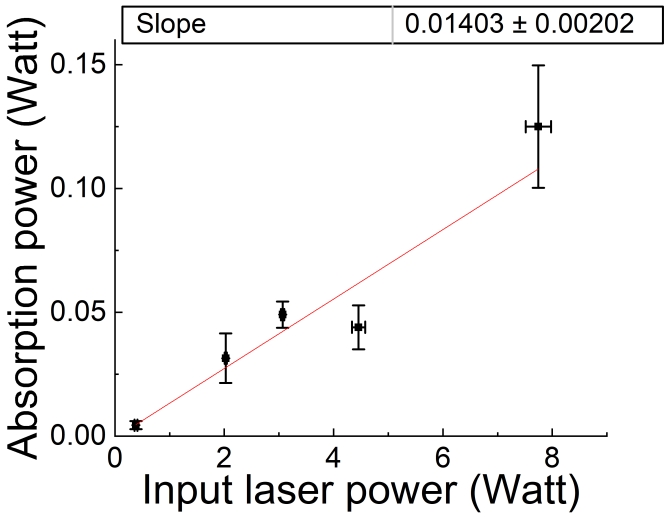

Figure 2.6. QDs absorption power versus incident power. The data was acquired on bare CdSe QDs sample purchased from NNlab with mean diameter of 3.5 nm.

around 3 nm is a $R \sim 10^9\,\mathrm{s}^{-1}$, leading to a radiative decay lifetime around 1 ns. It agrees with the result from the model in reference [72], but it is very different from experimental results reported, which typical values around $10-30$ ns [56,73–75]. The deviation suggests the existence of a very different emission mechanism inside CdSe QDs. Surface states were found to be responsible to the observation and PL emission through surface states were suggested to be an intrinsic property of CdSe QDs [62]. Excitonic decay through surface states was be introduced in the semi-empirical model developed for this research and will be discussed in section2.4.

2.3 Longitudinal optical phonon(LOP)-assisted photon absorption

Although the emission processes cannot be properly described by the "particle-in-a-sphere" model, its prediction in absorption processes is found to be much more reliable. Therefore, analysis of possible energy up-conversion processes during photon absorption was carried out with the equations derived in the previous sections.

LOP-annihilation coupled PL processes were determined to be the major cooling mechanism of the first optically cooled semiconducting material, CdS nanobelts [22]. Since phonon-coupled PL processes are also observed in CdSe based QDs [76, 77], the possibility of utilizing LOP-annihilation coupled PL processes to realize cooling is evaluated.

The possible cooling power of such process is based on the LOP energy and its coupling strength. The energy of the LOP in CdSe QDs is fixed and close to the bulk value, 25 meV [77, 78] approximately. However the transition rate needs to be calculated. It is well known LOPs couple to PL processes through the Fröhlich interaction [79, 80], which is adapted here for QDs. In the CdSe based QDs, a polar crystal system, a uniform deformation of the ions' position in each primitive cell due to the presence of a LOP leads to a macroscopic electric field $\vec{\mathcal{E}}_{\text{lop}}$ [61].

$$\vec{\mathcal{E}}_{\text{lop}} = -\Xi \vec{u}_{\text{lop}}, \tag{2.25}$$

where Ξ is the polarizability of CdSe ion pairs. $\vec{u}_{\text{lop}} = \vec{u}_{+} - \vec{u}_{-}$, $\vec{u}_{+}$ and $\vec{u}_{-}$ are the displacements of the Cd^{2+} and Se^{2-} ions from their equilibrium positions. From a macroscopic point of view, the electric displacement field inside the QD is zero, therefore

$$\epsilon_o \vec{\mathcal{E}}_{\text{lop}} = -\vec{\mathcal{P}}. \tag{2.26}$$

ϵ_o is the permittivity of the vacuum, $\vec{\mathcal{P}}$ is the induced polarization of the ion pairs inside CdSe QDs. $\vec{\mathcal{P}}$ is determined by the ion displacement $\vec{u}_{\text{lop}}$ and the local electic field $\vec{\mathcal{E}}_{\text{loc}}$,

$$\vec{\mathcal{P}} = e\mathcal{N}\vec{u}_{\text{lop}} + \mathcal{N}\Xi\vec{\mathcal{E}}_{\text{loc}}. \tag{2.27}$$

$\mathcal{N}$ denotes the number density of ion pairs. By considering the QDs are perfect spheres,

$$\vec{\mathcal{E}}_{\text{loc}} = \vec{\mathcal{E}}_{\text{lop}} + \frac{1}{3\epsilon_o}\vec{\mathcal{P}}. \tag{2.28}$$

According to Eq. 2.26, Eq. 2.27 and Eq. 2.28, $\vec{\mathcal{E}}_{\text{lop}}$ can be rewritten as

$$\vec{\mathcal{E}}_{\text{lop}} = \frac{-e\mathcal{N}}{\epsilon_o - \frac{2\Xi\mathcal{N}}{3}}\vec{u}_{\text{lop}}, \tag{2.29}$$

which can be expressed as the negative gradient of the delocalization electrical potential $\phi(\vec{r})$, such that

$$\nabla\phi(\vec{r}) = \frac{e\mathcal{N}}{\epsilon_o - \frac{2\Xi\mathcal{N}}{3}}\vec{u}_{\text{lop}}. \tag{2.30}$$

Since we assume that the dots have perfect spherical symmetry, we could write the delocalization electrical potential in the orthonormal basis set,

$$\phi(\vec{r}) = \sum_{l,m}\sum_{k} B_k\phi_{l,m}(k)j_l(kr)Y_l^m(\theta,\varphi),$$

where B_k is the normalization constant. Hence

$$\vec{u}_{\text{lop}} = \sum_{l,m}\sum_{k} u_o\nabla j_l(kr)Y_l^m + Cc. \tag{2.31}$$

Here Cc represents the complex conjugate and u_o is the normalization constant. The energy density of LOP $d\varepsilon_{\text{lop}}$ can be written as,

$$d\varepsilon_{\text{lop}} = \frac{1}{2}\mathcal{N}\mathcal{M}\dot{\vec{u}}_{\text{lop}}^2 + \frac{1}{2}\mathcal{N}\Xi\vec{u}_{\text{lop}}^2. \tag{2.32}$$

Here $\mathcal{M}$ is the reduced mass of the ion pair. ε_{lop} can be calculated by integrating $d\varepsilon_{\text{lop}}$ over the whole QD. $\frac{1}{2}\mathcal{N}\mathcal{M}\dot{\vec{u}}_{\text{lop}}^2$ and $\frac{1}{2}\mathcal{N}\Xi\vec{u}_{\text{lop}}^2$ denote the kinetic energy and potential energy part of the LOP respectively. Here the calculation can be done by applying Green's first identity

$$\int_{\text{v}}\nabla\phi_1\nabla\phi_2 d\vec{r} = -\int_{\text{v}}\phi_1\nabla^2\phi_2 d\vec{r} + \int_{\text{a}}\phi_1\frac{\partial\phi_2}{\partial\vec{n}}da. \tag{2.33}$$

For LOP inside the QDs, the surface integral is zero and $\nabla^2\phi(\vec{r}) = k^2\phi(\vec{r})$. By introducing the standard LOP phonon Hamiltonian in terms of the creation and annihilation operators $a_{l,m}^{\dagger}$ and $a_{l.m}$ is given by

$$\mathcal{H}_{\text{lop}} = \varepsilon_{\text{lop}}(a_{l,m}^{\dagger}a_{l.m} + \frac{1}{2}), \tag{2.34}$$

The solution of the $\vec{u}_{\text{lop}}$ is,

$$\vec{u}_{\text{lop}}(\mathbf{r}) = \sum_{l,m}\sum_{k}\Big[\frac{\hbar^2 B_k^2}{2\mathcal{N}\mathcal{M}\varepsilon_{\text{lop}}k^2}\Big]^{1/2} \times [a_{l,m}(k)\nabla j_l(kr)Y_l^m(\theta,\varphi) + Hc.]. \tag{2.35}$$

Hc denotes the Hermitian conjugate.

From Eq. 2.30 and Eq. 2.35 we derive

$$\phi(r) = \sum_{l,m}\sum_{k}\Big[\frac{\varepsilon_{\rm lop}B_k^2}{2\epsilon_0 k^2}\Big]^{1/2}\Big[\frac{1}{\epsilon(\infty)}-\frac{1}{\epsilon(0)}\Big]^{1/2}\times[a_{l,m}(k)j_l(kr)Y_l^m(\theta,\varphi)+Hc], \quad (2.36)$$

where

$$\frac{\mathcal{N}e}{1+\frac{2}{3}\mathcal{N}\alpha}\Big[\frac{\epsilon_0\varepsilon_{\rm lop}^2}{\mathcal{N}\mu}\Big]^{1/2}=\Big[\frac{1}{\epsilon(\infty)}-\frac{1}{\epsilon(0)}\Big]^{1/2}. \quad (2.37)$$

$\epsilon(0)$ and $\epsilon(\infty)$ are CdSe's dielectric constants in static and high frequency electric filed respectively. Thus

$$\mathcal{H}_{\text{e-ph}} = \int \phi(r)\rho(r)d\tau, \quad (2.38)$$

Where $\rho(r)$ is the charge density of the photon induced exciton. To finally calculate the absorption probability $R_{\rm ph}$ of these processes, second order TDP is used,

$$R_{\rm ph} \simeq \frac{2\pi}{\hbar}\Big|\frac{<0|\mathcal{H}_{e-R}|1><1|\mathcal{H}_{e-ph}|1>}{\varepsilon-\varepsilon_{\rm ex}+i\Gamma_i}\Big|^2 g(\varepsilon_{\rm ex}+\varepsilon_{\rm lop})\frac{1}{1+e^{\frac{3}{2}\varepsilon_{\rm lop}/k_{\rm b}T}}. \quad (2.39)$$

Here $g(\varepsilon)$ is the density of state (DOS) and $|0\rangle = |\Phi_{\rm e}^{\rm v}\rangle|\Phi_{\rm h}^{\rm v}\rangle$ and $|1\rangle = |\Phi_{\rm e}^{\rm c}\rangle|\Phi_{\rm h}^{\rm v}\rangle$ were introduced for simplicity. In Eq. 2.39. Γ_i is the intrinsic broadening of level $|1\rangle$ and the $\frac{1}{1+e^{\frac{3}{2}\varepsilon_{\rm lop}/k_{\rm B}T}}$ term describes the thermal population of the LOPs, where $k_{\rm B}$ is the Boltzmann constant.

The most important result for OR is not the absolute value or $R_{\rm ph}$, but $\frac{R_{\rm ph}}{R}$. According to the calculation result, $\frac{R_{\rm ph}}{R}\approx 8.4$ was derived, suggesting a strong coupling of LOP assisted photon abosption in CdSe QDs.

2.4 Semi-empirical modeling of PL lineshape

The cooling efficiency of the QDs relies on both absorption and emission processes. But, as shown in section 2.2, emission processes in QDs cannot be described by the band-edge transition properly. Therefore, to quantitatively describe QDs PL processes, a new approach is required.

Although the absorption spectra of QDs is qualitatively described by the "particle-in-a-sphere" model, the emission processes in QDs is not as simple. Furthermore,

while QDs have been studied extensively, very limited information exists about the overall PL lineshape on ensembles. Since this is a critical part in OR, we have developed a semi-empirical model for PL lineshape.

Experimentally, the absorption and PL emission spectra of QDs ensembles do not behave as an atomic-like quasi-monochromatic lineshape. A noticeable redshift of PL spectra with respect to the absorption has been found for all kinds of QDs [81, 82]. Surface states has been claimed to be responsible for the redshift [56, 62, 83, 84], and the main path for carrier transfer between conduction and surface states is attributed to be vibration-coupled processes (typically, acoustic phonons in QDs). Surface states are also considered a source (other sources are the size distribution of QDs samples and the phonon-coupled PL processes) of the broadening in QDs' PL linewidth at room temperature, where the typical full-width-half-maximum (FWHM) of QDs samples' PL spectra is around 90 meV [85–87]. Even for a single QD, a PL spectrum linewidth much wider than the ones for atoms at room temperature was observed by Chen and his coworkers [88]. On the other hand, with the typical size of several nanometers, there are hundreds to thousands of atoms in a single QD. It is impossible to completely solve for the Hamiltonian of any practical QD's system. Meanwhile, the size of QDs is not big enough to be well described by solid state physics approaches for lattice systems. Therefore, we made an attempt of describing the QDs' PL spectra quantitatively by applying a semi-empirical model based on our experimental results. Thus, we can shortcut the arduous exact theoretical work and give practical predictions for QDs' PL spectral lineshape, which is necessary when considering OR applications of QDs.

In 2003, Wang *et. al* [56] suggested recombinations from surface states are the dominant emission processes in CdSe QDs. More recently, Gao *et. al* [62] suggested surface states light emission is an intrinsic property of zinc-blende CdSe QDs. Thus, in our model, all radiative recombinations of the excitons in QDs are assumed to take place through surface states. To describe QDs' broad PL spectra, a Gaussian

distribution[1] $O_s(\varepsilon)$ with its center at ε_s and variance of σ_s is used for the surface DOS, which we will refer to as the surface band. ε_s is extracted from PL experiments. Similarly, to describe the broadening in QDs' absorption spectra, a Gaussian $O_d(\varepsilon)$ with its center ε_d and variance σ_d is used for QDs' absorption edge (the complete absorption spectrum can be described by adding more Gaussian DOSs for higher excitonic states), and transition allowed energy levels become absorption bands. ε_d and σ_d are determined from absorption experiments. The carrier transfer from the absorption band to the surface band is accomplished through acoustic-phonon-assisted processes in the model, and is assumed to be much faster than the intra-band transition inside the absorption band. Therefore, the intra-band transition in the absorption band is negligible. Accordingly, four parameters are needed to be defined for completing the overall lineshape:

(i) k_s: Intra-band transition probability between energy levels within the surface band;

(ii) k_{int}: Inter-band transition probability between energy levels in absorption and surface bands;

(iii) k_r: Radiative decay probability;

(iv) k_{nr}: Non-radiative decay probability.

For simplicity, all transition probabilities were considered to be energy independent. According to the model, a schematic plot of the PL process which can potentially achieve net up-conversion in QDs' PL mean emission energy is shown in Fig. 2.7. In the figure, a sub-band excitation (SBE) with energy ε_{ex} ($\varepsilon_{ex} < \varepsilon_s < \varepsilon_d$) yields the creation of excitons through LOP-annihilation-coupled photon absorption processes. Since the phonon coupling strength is weak in CdSe QDs comparing to the bulk(section 1.5, $S \sim 0.1$), only single LOP coupled photon absorption processes were considered. Thus, by defining the excitonic ground state as 0 energy, the energy of

[1]The broadening of QDs' PL spectra originates from complicated sources, such as the inhomogeneity of QDs' size distribution and shape. Furthermore, experimentally, the lineshape of CdSe QDs' absorption and PL emission spectra were found to be Gaussian like. Therefore, a Gaussian density of states is considered as an acceptable approximation to describe the electronic structure of our samples. But, if needed, real spectra can be directly implemented into the model.

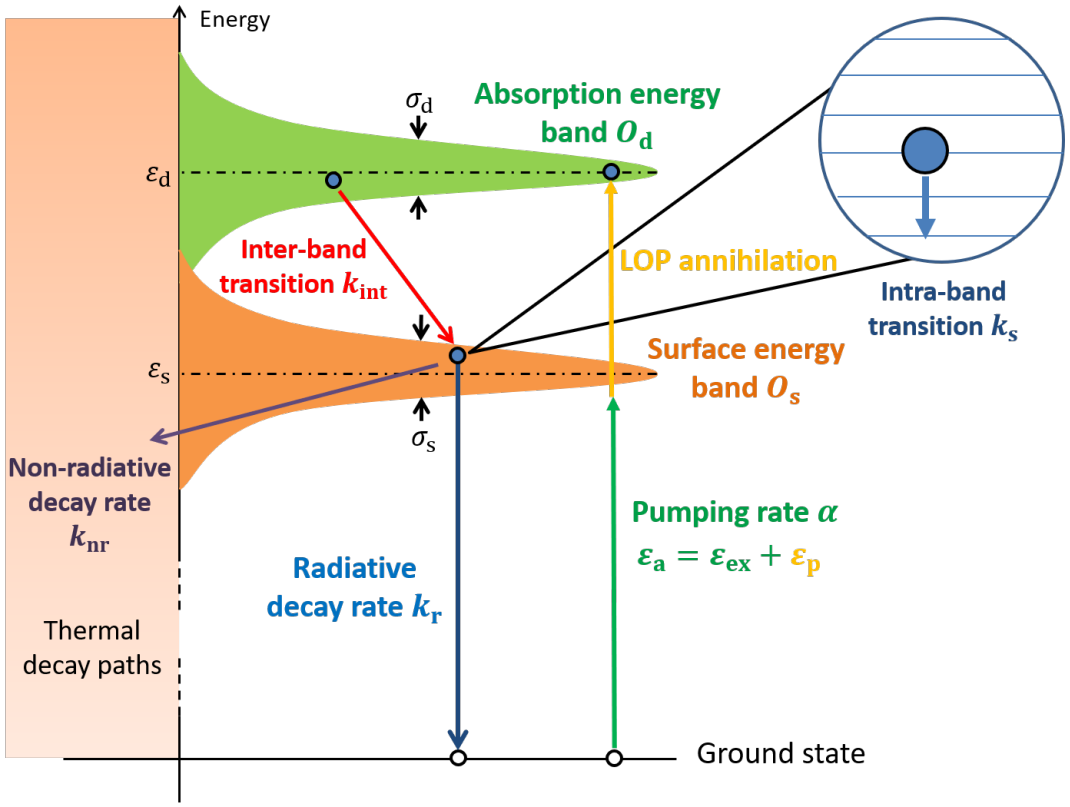

Figure 2.7. Scheme plot of a possible OR process according to the semi-empirical model.

the created exciton ε_a is

$$\varepsilon_a = \varepsilon_{ex} + \varepsilon_{LOP}.$$

At SBE, the creation of excitons only occurs in the CdSe core [1, 2, 42], therefore, the LOPs of CdSe are considered as the source of ε_{lop}. Following the excitation, excitons rapidly transition to the surface band through the acoustic-phonon-assisted inter-band transition. The transition rate is governed by the phonon DOS $g(\varepsilon)$. Because the phonon dispersion relationship is not clear inside QDs, for the sake of simplicity, and as an approximation, the phonon dispersion relationship is defined as

$$\omega = c_{ph} k. \tag{2.40}$$

Here c_{ph} denotes the speed of sound in the material. As assumed by the model, the transition is between the intrinsic excitonic states and the surface states, both bulk

and surface acoustic phonon modes are considered to be possible to participate in the inter-band transition processes. Additionally, according to results in section 2.1.1, the probability of finding both carriers, particularly electrons, near the surface is significant. Therefore, a fitting parameter ξ was assigned to indicate the dimensionallity of phonon modes ($\xi = 2$ for surface, $\xi = 3$ for bulk). Hence, the phonon DOS is given by

$$g_\xi(\varepsilon) = C_\mathrm{g}\Big|\frac{\varepsilon^{\xi-1}}{e^{\varepsilon/k_\mathrm{B}T}-1}\Big|,$$

where C_g is the coupling strength, containing the information of c_ph. For a phonon emission process, ε is treated as a negative number.

The rate of change of excitonic density $N_\mathrm{d}(\varepsilon)$ with energy ε in the absorption band is given by

$$\frac{dN_\mathrm{d}(\varepsilon)}{dt} = \alpha\delta(\varepsilon-\varepsilon_\mathrm{a})O_\mathrm{d}(\varepsilon) - k_\mathrm{int}N_\mathrm{d}(\varepsilon)\int_{\varepsilon_\mathrm{a}-\varepsilon_\mathrm{c}}^{\varepsilon_\mathrm{a}+\varepsilon_\mathrm{c}} g_\xi(\varepsilon^{'}-\varepsilon)O_\mathrm{s}(\varepsilon')d\varepsilon'. \tag{2.41}$$

In Eq. 2.41, $\alpha\delta(\varepsilon-\varepsilon_\mathrm{a})O_\mathrm{d}(\varepsilon)$ describes the photon absorption processes. The second term in the right side denotes an exciton lost through an inter-band transition. ε_c is the phonon cut-off energy (energy of the highest phonon frequency allowed in a lattice), which is unknown for CdSe QDs at room temperature. However, to be able to describe QDs' broad PL spectra, a ε_c larger than the spectra' FWHM is required. It is much larger than the bulk CdSe phonon cut-off energy, a fact that cannot be explained properly at this stage. By accepting the big ε_c value, since $k_\mathrm{B}T$ is close to the value of LOP, $\varepsilon_\mathrm{c} >> k_\mathrm{B}T$. Therefore, g_ξ vanishes when approaching ε_c, and the integral's limit can be set to zero and infinity to simplify the calculation. In steady state condition, $\frac{dN_\mathrm{d}(\varepsilon)}{dt} = 0$, and

$$N_\mathrm{d}(\varepsilon) = \frac{\alpha\delta(\varepsilon-\varepsilon_\mathrm{a})O_\mathrm{d}(\varepsilon)}{k_\mathrm{int}(\varepsilon)\int_0^\infty g_\xi(\varepsilon'-\varepsilon)O_\mathrm{s}(\varepsilon')d\varepsilon'}. \tag{2.42}$$

Once the excitons transition to the surface band, three possible decay paths are allowed for them: redistribute inside the surface band through the intra-band transi-

tion, or following a radiative or non-radiative decay path to the ground state. Doing a similar calculation as for $N_{\rm d}$

$$\frac{dN_{\rm s}(\varepsilon)}{dt} = k_{\rm s}O_{\rm s}(\varepsilon)\int_0^\infty g_2(\varepsilon-\varepsilon')N_{\rm s}(\varepsilon')d\varepsilon' - k_{\rm s}N_{\rm s}(\varepsilon)\int_0^\infty g_2(\varepsilon'-\varepsilon)O_{\rm s}(\varepsilon')d\varepsilon' \\ -(k_{\rm r}+k_{\rm nr})N_{\rm s}(\varepsilon) + k_{\rm int}O_{\rm s}(\varepsilon)\int_0^\infty g_\xi(\varepsilon-\varepsilon^{'})N_{\rm d}(\varepsilon')d\varepsilon', \quad (2.43)$$

The term $k_{\rm s}O_{\rm s}(\varepsilon)\int_0^\infty g_2(\varepsilon-\varepsilon')N_{\rm s}(\varepsilon')d\varepsilon'$ and $k_{\rm s}N_{\rm s}(\varepsilon)\int_0^\infty g_2(\varepsilon'-\varepsilon)O_{\rm s}(\varepsilon')d\varepsilon'$ denote excitons transitioning to or from the level $\varepsilon_{\rm ex}$ at ε through intra-band transition respectively. Because the intra-band transition is inside the surface band, $\xi = 2$ was used. $(k_{\rm r}+k_{\rm nr})N_{\rm s}(\varepsilon)$ accounts for excitons lost from radiative and non-radiative processes. Since mathematically the contributions from $k_{\rm r}$ and $k_{\rm nr}$ are indistinguishable, they are treated as a single parameter $k_{\rm r}' \equiv k_{\rm r}+k_{\rm nr}$. The term $k_{\rm int}O_{\rm s}(\varepsilon)\int_0^\infty g_\xi(\varepsilon-\varepsilon^{'})N_{\rm d}(\varepsilon')d\varepsilon'$ denotes receiving excitons through the inter-band transition from the absorption band. According to Eq. 2.42, this term is rewritten as

$$k_{\rm int}O_{\rm s}(\varepsilon)\int_0^\infty g_\xi(\varepsilon-\varepsilon^{'})N_{\rm d}(\varepsilon')d\varepsilon' = \alpha\frac{g_\xi(\varepsilon-\varepsilon_{\rm a})O_{\rm d}(\varepsilon_{\rm a})O_{\rm s}(\varepsilon)}{\int_0^\infty g_\xi(\varepsilon'-\varepsilon_{\rm a})O_{\rm s}(\varepsilon')d\varepsilon'} \equiv \alpha n_{\rm d}(\varepsilon).$$

Using the notation

$$\int_0^\infty g_2(\varepsilon-\varepsilon')N_{\rm s}(\varepsilon')d\varepsilon' \equiv g_2 * N_{\rm s}(\varepsilon), \quad (2.44)$$

which is a convolution of $g_2(\varepsilon)$ and $N_{\rm s}(\varepsilon)$, and setting $\int_0^\infty g_2(\varepsilon'-\varepsilon)O_{\rm s}(\varepsilon')d\varepsilon' \equiv F(\varepsilon)$, in steady state, Eq. 2.43 is rewritten as

$$0 = k_{\rm s}O_{\rm s}(\varepsilon)g_2 * N_{\rm s}(\varepsilon) - [k_{\rm s}F(\varepsilon)+k_{\rm r}']N_{\rm s}(\varepsilon) + \alpha n_{\rm d}(\varepsilon). \quad (2.45)$$

Eq. 2.45 is an inhomogeneous integral equation and does not have a general solution. It was solved by treating the term $k_{\rm s}O_{\rm s}(\varepsilon)g_2 * N_{\rm s}(\varepsilon)$ as a modification to the function

$$0 = -[k_s F(\varepsilon)+k_{\rm r}+k_{\rm nr}]N_{\rm s}(\varepsilon) + \alpha n_{\rm d}(\varepsilon). \quad (2.46)$$

The solution of Eq. 2.46 is simply

$$N_{\rm s}^0(\varepsilon) = \frac{\alpha n_{\rm d}(\varepsilon)}{k_{\rm s}F(\varepsilon)+k_{\rm r}'}.$$

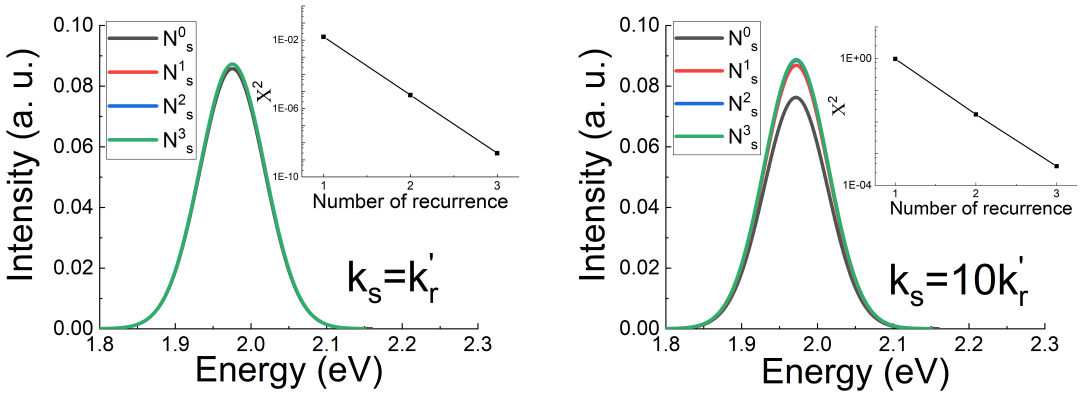

(a) (b)

Figure 2.8. Photoluminescence intensity $I_\varepsilon = k_r N_s(\varepsilon)$ for different numbers of the recurrence: (a) $k_s = k_r'$, (b) $k_s = 10k_r'$. $\varepsilon_{ex} = 1.945$ eV, $\varepsilon_d = 2.059$ eV, $\varepsilon_s = 2.023$ eV, $\sigma_d = 0.034$ eV, $\sigma_s = 0.045$ eV and $\xi = 2$ were used in the calculation.

Where the superscription of N_s denotes the order of the solution in Eq. 2.45. Substituting N_s^0 into the first term of Eq. 2.45 yields $N_s^1(\varepsilon)$

$$0 = k_s O_s(\varepsilon) g_2 * N_s^0(\varepsilon) - [k_s F(\varepsilon) + k_r'] N_s^1(\varepsilon) + \alpha n_d(\varepsilon).$$

In general, using $N_s^{(n)}$ in the first term of Eq. 2.45, yields N_s^{n+1}. As shown in Fig. 2.8(a) and 2.8(b) ($\xi = 2$ was used in the calculation), $\chi^2 = \int_0^\infty [N_s^n(\varepsilon) - N_s^{n-1}(\varepsilon)]^2 d\varepsilon$ decreases rapidly as n increases, suggesting a rapid convergence of the recurrence, even for large $k_s/k_{r'}$ value. Since the emission processes in the model is described by a simple radiative decay process with single lifetime, the QDs' PL intensity, $I(\varepsilon)$ is given by

$$I(\varepsilon) = k_r N_s(\varepsilon). \tag{2.47}$$

As k_s increases, the center of $N_s(\varepsilon)$ moves to lower energy. Therefore, by fitting the data from the CdSe/CdS QD samples, $k_s = 0$ was used in the model. As a consequence, k_r' and α only adjust the amplitude of the simulated PL lineshape. So, the only fitting parameters left are ξ and σ_s.

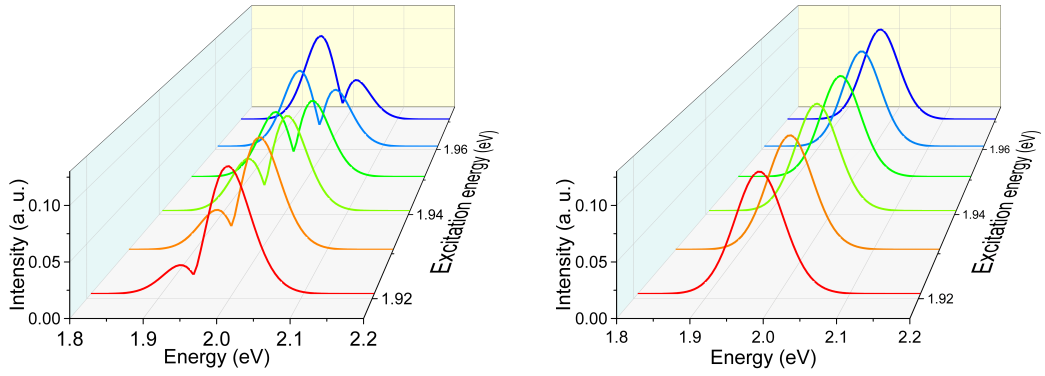

(a) (b)

Figure 2.9. Simulated PL spectra with (a) $\xi = 3$ and (b) $\xi = 2$. The calculation was carried out with $\varepsilon_{\mathrm{ex}} = 1.971$ eV, 1.961 eV, 1.951 eV, 1.941 eV, 1.931 eV and 1.921 eV. $\varepsilon_{\mathrm{d}} = 2.059$ eV, $\varepsilon_{\mathrm{s}} = 2.023$ eV, $\sigma_{\mathrm{d}} = 0.034$ eV, $\sigma_s = 0.45$ eV were used in the calculation.

The option of ξ are integers 2 and 3, corresponding to the surface and bulk phonon modes respectively. As shown in Fig. 2.9(a), a dip was observed at ε_{a} in the simulated PL spectra with $\xi = 3$. When $\varepsilon \to 0$, $g_3(\varepsilon) \to \frac{\varepsilon^2}{\varepsilon} \to 0$. The dip is more pronounced than observed due to numerical precision. However, the dip was not observed in the PL spectra of our sample. The experimental data of sample with $\varepsilon_{\mathrm{d}} = 2.059$ eV, $\varepsilon_{\mathrm{s}} = 2.023$ eV, FHWM= 0.082 eV (equivalent to $\sigma = 0.034$ eV for a Gaussian) is shown in Fig. 2.10. A smooth PL lineshape was observed, while the emission peak is slightly red shifted as the $\varepsilon_{\mathrm{ex}}$ decreased. The spikes observed in the PL spectra were attributed to the scattered laser light and their intensity is negligible compared to the PL intensity (experimental details and the sample information will be discussed in Chapter 3). Therefore, $\xi = 3$ does not work for high quality CdSe/CdS QDs. The dips are removed if $g_\xi(0)$ has a finite non-zero value, which is the case for $\xi = 2$.

The simulation results with $\xi = 2$ are shown in Fig. 2.9(b), where a smooth lineshape and the redshift in emission energy were successfully recovered by the model. The value of σ_{s} was determined by fitting the experimental results (only one σ_{s} was used for all data sets). As shown in Fig. 2.11, the simulated result showed a good

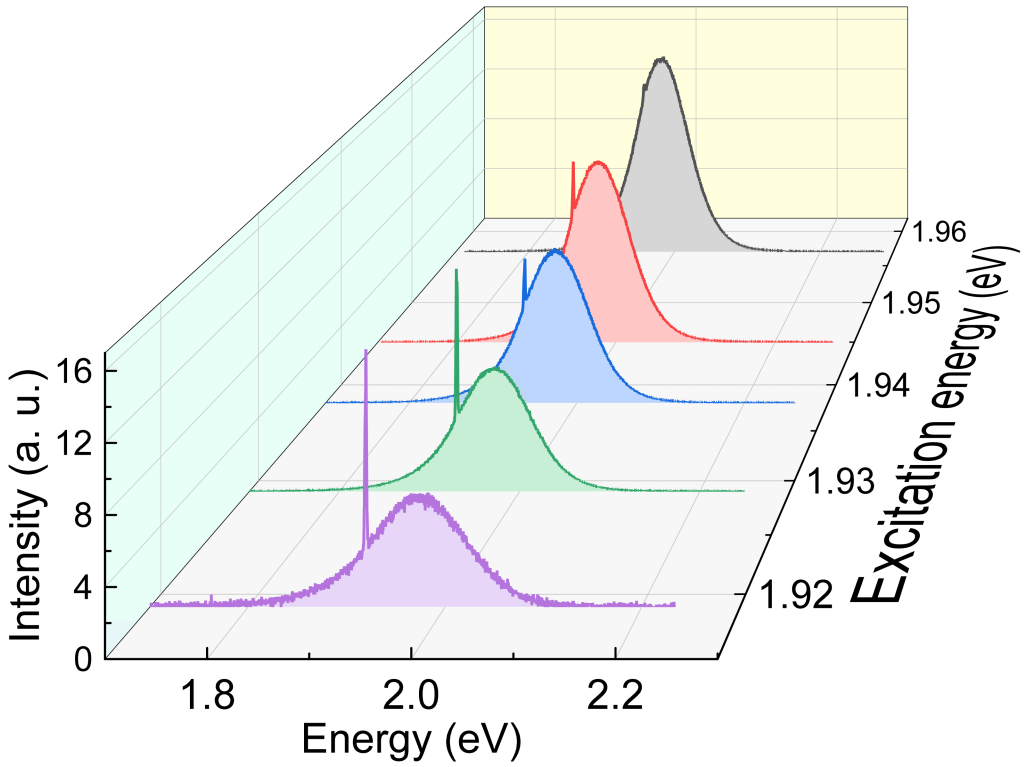

Figure 2.10. Photoluminescence spectra (experimental result) of CdSe/CdS QDs sample with sub-band excitation at $\varepsilon_{ex} = 1.957$ eV, 1.946 eV, 1.938 eV, 1.929 eV and 1.919 eV. The sample was from batch 2 with $\varepsilon_d = 2.059$, $\varepsilon_s = 2.023$, FHWM= 0.082 eV.

agreement with the experimental data, and the best fit was achieved at $\sigma_s = 0.045$ eV. The most significant deviation between the model and experimental data was observed at $\varepsilon_{ex} = 3.05$ eV, which was expected (the assumption of only having LOP coupled photon absorption no longer holds as the absorption efficiency increased significantly).

According to the model, at SBE, single LOP absorption processes are coupled to the photon absorption creating a net energy up-conversion. However, it is not the major source of the significant up-conversion observed in the QDs samples. Without introducing multiphonon absorption (because in CdSe QDs, as reported, their $S < 1$ [63, 65]) the up-conversion processes are heavily influenced by the acoustic phonon assisted surface inter-band transition processes.

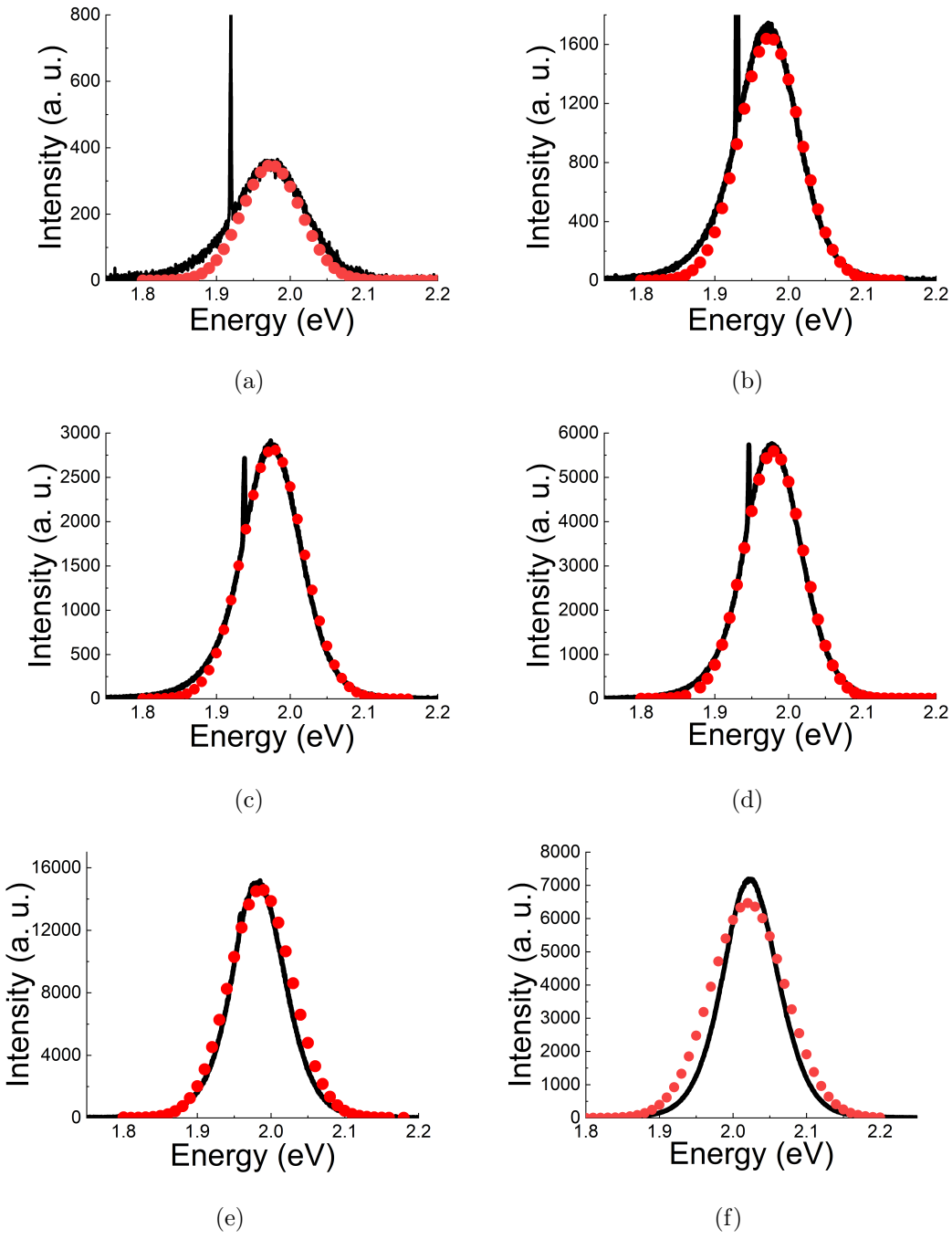

Figure 2.11. Fitting result with $\sigma_{\mathrm{s}} = 0.045$ eV for experimental data at $\varepsilon_{\mathrm{ex}} =$: (a) 1.919 eV, (b) 1.929 eV, (c) 1.938 eV, (d) 1.946 eV, (e) 1.957 eV and (f) 3.05 eV. $\varepsilon_{\mathrm{d}} = 2.059$, $\varepsilon_{\mathrm{s}} = 2.023$ and $\sigma_d = 0.034$ eV derived from experimental data were used in the calculation.

2.5 Cooling efficiency calculation

According to section 1.2, the cooling efficiency of OR is defined as

$$\eta_{\mathrm{c}} = \eta_{\mathrm{eff}} \frac{1}{(1+\alpha_{\mathrm{b}}/\alpha)} \frac{\bar{\varepsilon}_{\mathrm{em}}}{\varepsilon_{\mathrm{ex}}} - 1. \tag{2.48}$$

With the help from the model, $\bar{\varepsilon}_{\mathrm{em}}$ can be obtained for all possible SBE energies. Here PL mean emission energy $\bar{\varepsilon}_{\mathrm{em}}$ is defined as

$$\bar{\varepsilon}_{\mathrm{em}} = \frac{\int_0^\infty \varepsilon I(\varepsilon) d\varepsilon}{\int_0^\infty I(\varepsilon) d\varepsilon}. \tag{2.49}$$

Therefore, by combining Eq. 2.48 and 2.49, for a given set of η and α_{b}, η_c can be plotted versus $\varepsilon_{\mathrm{ex}}$ and the region with a positive value is considered as the cooling zone (α is obtained from absorption spectroscopy, which will be discussed in Chapter 3). In the case of perfect QY ($\eta = 1$), as shown in Fig. 2.12(a), the cooling zone disappeares when $\alpha_{\mathrm{b}}/\alpha$ is larger than 3000 ppm (part per million), while a maximum $\eta_c > 1\%$ is accessible if $\alpha_{\mathrm{b}}/\alpha < 1000$ ppm. On the other hand, with a finite $\alpha_{\mathrm{b}}/\alpha =$ 500 ppm, a minimum value of $\eta = 99\%$ is required to achieve net cooling, while the maximum cooling efficiency is located around 1.93 eV. Hence, net cooling is achievable in CdSe/CdS QDs.

2.6 Calculation of possible heating processes

OR can be realized in CdSe QDs system when a positive η_{c} value is achieved. The actual final temperature is determined by the existence of heating processes. Therefore, to ensure the OR effect is experimentally observable, possible parasitic heating processes and the heat flow from the environment due to the temperature gradient introduced by OR needs to be evaluated.

A major heating introduced into the system is phonon-creation through energy down-conversion PL (DCPL) or non-radiative decay processes. DCPL decreases $\bar{\varepsilon}_{\mathrm{em}}$, and non-radiative decay processes are reflected in η, the QY of the system.

Besides the heating process from the QDs themselves, the substrate of the QDs, the sample holder, the suspension solvent and the supporting matrix also absorb

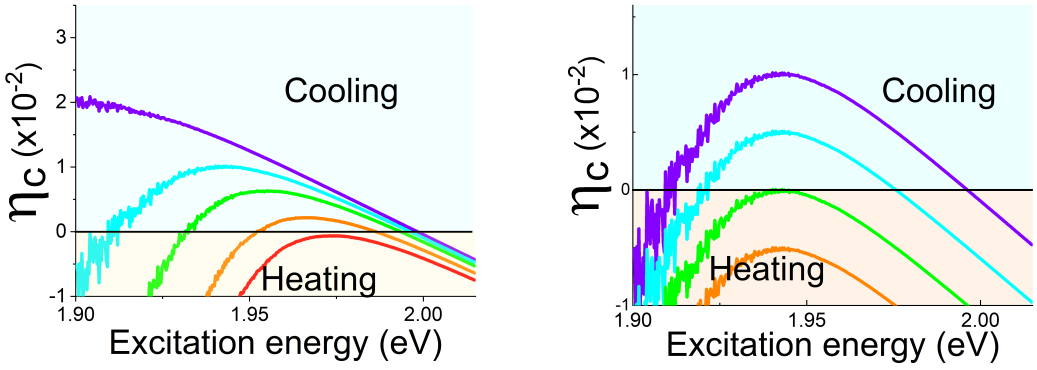

(a) (b)

Figure 2.12. Cooling efficiency versus excitation energy at: (a) α_b/α = 100 ppm (purple), 500 ppm (cyan), 1000 ppm (green), 2000 ppm (orange) and 3000 ppm (red) with $\eta = 1$. (b) η = 100% (purple), 99.5% (cyan), 99% (green) and 98.5% (orange) with α_b/α = 500 ppm.

incident light. A part of this is transferred to the QDs, resulting in heating processes. Fortunately, materials with very limited absorption rate at the laser wavelength of the experiment (around 650 nm) are accessible. For example, the absorption rate of regular BK7 glass (boronsilicate) at wavelength of 650 nm is less than 20 parts per million per millimeter [89]. And this number can be further reduced by focusing the laser beam, which would reduce unwanted multi-reflections inside the capillary and the glass wall. The heating power associated to background absorption is taken into account in the calculation of the cooling efficiency by introducing the background absorption rate α_b. If a positive cooling efficiency of the system can be achieved by including the heating process from the QDs and the sample holders, net cooling of the system would be achieved.

Heat transfer due to the thermal non-equilibrium between the sample and the environment were also evaluated. Heat transfer through thermal radiation is one important heating source. For a black-body at temperature T, the radiation power

dP_{sb} emitted from its surface (considering the case where the surface is flat) element da is given by Stefan-Boltzmann law

$$dP_{\mathrm{sb}}(T) = \int_0^{\infty} I_{\mathrm{b}}(\omega, T)d\omega \int_0^{2\pi} d\phi \int_0^{\frac{\pi}{2}} \cos\theta \sin\theta d\theta da. \tag{2.50}$$

This fomula is derived by treating the the emission body as a Lambertian (black bodies yield the Lambert's cosine Law [90]). Here, $I_{\mathrm{b}}(\omega, T)$ denotes the intensity of the emitting radiation at angular frequency ω with temperature T, which is governed by Plank's law

$$I_{\mathrm{b}}(\omega, T) = \frac{\hbar}{4\pi^3 c^2} \frac{\omega^3}{e^{\frac{\hbar\omega}{k_{\mathrm{b}}T}} - 1}. \tag{2.51}$$

By substituting $\zeta = \frac{\hbar\omega}{k_{\mathrm{b}}T}$ into Eq. 2.51, Eq 2.50 can be written as

$$dP_{\mathrm{sb}} = \frac{k_{\mathrm{b}}^4 T^4}{4\pi^2 c^2 \hbar^3} \int_0^{\infty} \frac{\zeta^3}{e^{\zeta} - 1} d\zeta da. \tag{2.52}$$

The integral in Eq. 2.52 is the Riemann zeta function, which solution is $\frac{\pi^4}{15}$. Hence,

$$dP_{\mathrm{sb}} = \sigma_{\mathrm{sb}} T^4 da, \tag{2.53}$$

where $\sigma_{\mathrm{sb}} = \frac{\pi^2 k_{\mathrm{b}}^4}{60 c^2 \hbar^3} \simeq 5.67 \times 10^{-8}\,\mathrm{W/(m^2K^4)}$ is the Stefan-Boltzmann constant. In a more realistic situation where the material surface is acting like a grey body, (not all the radiation reaching it being absorbed and emitted), Eq. 2.53 is modified by the emissivity ϱ,

$$dP_{\mathrm{sb}} = \varrho \sigma_{\mathrm{sb}} T^4 da.$$

Therefore, the net heat flow P_{sb} between the sample and the environment is given by,

$$P_{\mathrm{sb}} = \sigma_{\mathrm{sb}} \int_{A_{\mathrm{sa}}} \Upsilon(\varrho_{\mathrm{en}} T_{\mathrm{en}}^4 - \varrho_{\mathrm{sa}} T_{\mathrm{sa}}^4) da. \tag{2.54}$$

The subscripts "sa" and "en" denote the sample and environment respectively. Υ is the view factor. Eq. 2.54 is a surface integral, which must integrated over the entire surface of the sample. In our application, samples are QDs suspended inside organic solvent, such that the surface used in the calculation is the surface of the loading capillary and ϱ_{sa} is the emissivity of the capillary glass. On the other hand, the

environment (cryostat chamber) is complicated in both geometry and materials (*i. e.* brass plates, anodized aluminum substrate and copper cold finger), in consequence the calculations were done with the simulation software Comsol Multiphysics.

Heat conduction through the substrate is another possible heating source. With a given geometry and known material of the support of the sample, the conduction heat power P_{h} can be calculated by

$$P_{\mathrm{h}} = k_{\mathrm{c}} \frac{a_{\mathrm{c}}}{L_{\mathrm{c}}} \Delta T, \tag{2.55}$$

where k_{c} is the thermal conductivity of the support, a_{c} and L_{c} are the effective cross-sectional area and the effective length of the support.

Given the geometry of our system, it is not possible to analytically find the heat transfer. The numerical evaluation was performed with Comsol Multiphysics program. As shown in Fig. 2.13(a), a 3-dimensional model which is a replica of the sample and sample holder with the surrounding enclosure was built in the program. Materials' parameters, such as thermal conductivity and emissivity were assigned from the default values from the program material package. The mesh size was customized to give better precision: 2μm for the laser path, $8\,\mu$m for the contacting surface between different materials. It needs to be pointed out that the software considered the mesh to be insufficient for the laser path, while it was not able to provide finer meshing. For the remaining surface (*i. e.* the disc and the chamber), the auto mesh was used.

By assuming $\eta_{\mathrm{c}} \approx 1.5\%$, and using 3 mW input pump laser power and a 30% absorption efficiency (derived from the sample's absorption spectrum), a net cooling power of $12\,\mu$W was obtained to the laser path region (8μm beam size, determined as the 68% intensity of a Gaussian beam). As shown in Fig. 2.13(c), a temperature drop of 0.1 K was suggested by the software. Therefore, a thermoetry technique with at least 0.1 K sensitivity is required to observe the cooling effect. However, the calculation showed a strong dependence on the size of the cooling zone. Since the power of the pump laser was not uniformly distributed through the path (focus to

the entrance part), and the software is not able to run a finer mesh, we stopped here and considered it an estimation.

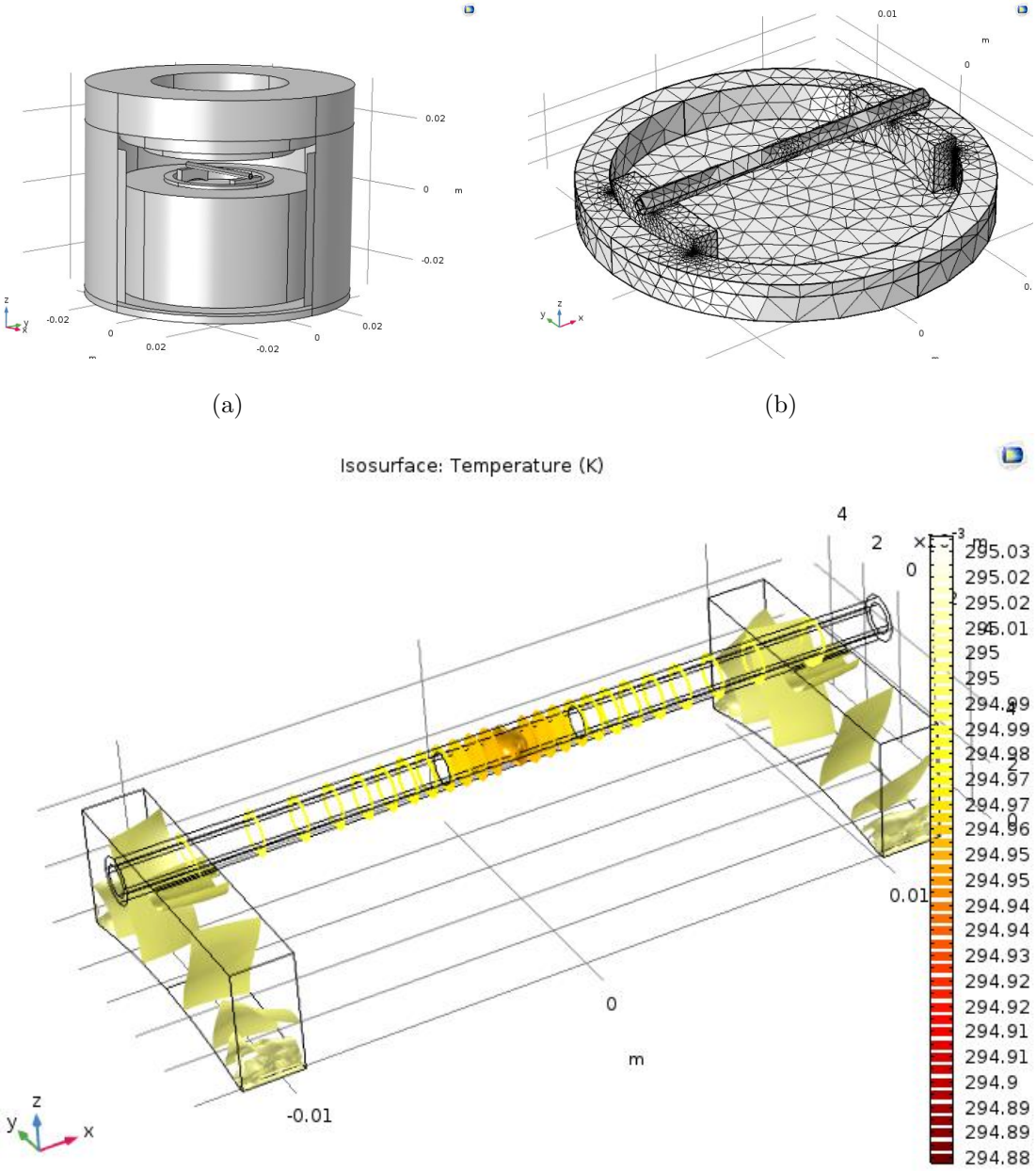

(a) (b)

(c)

Figure 2.13. Simulation result from Comsol software. (a) 3-D model of the experimental setup, (b) Mesh of the sample and sample holder, (c) Simulation result of the temperature gradient with a cooling power of 10 μW uniformly distributed along the laser path. The ambient and initial temperature used in the calculation were both 295 K. The software version is Comsol Multiphysics v 5.3 a.

3. EXPERIMENTAL DETAILS AND SAMPLE CHARACTERIZATION

To realize OR in CdSe/CdS QDs, a synthesis reactor was set up to produce high quality samples with unity QY. The production was based on the procedure developed by Peng's group [2] and modified by us according to our lab conditions and feedback obtained from the characterization results of the synthesized QDs. The homemade samples' UCPL properties were characterized by an enhanced off-axis collecting system designed and built in our lab. Characterization data showed good agreement with the model developed and reinforced the possibility of realizing OR on QDs. Accordingly, an OR experiment by using the homemade CdSe/CdS QDs samples was set up and performed, where the net cooling effect was observed. In this chapter, the synthesis procedures, QDs characterization techniques and most importantly, the OR experiment setup implemented will be discussed in detail.

3.1 Quantum dots synthesis

As mentioned in section 1.3.1, the QDs synthesis was carried out through the wet-chemical method. Our synthesis procedure is a modified approach based on the methods proposed by Cao's group [43] and improved by Peng *et al.* [1]. In this method, CdSe monomers are generated by mixing chemically active elementary Se with Cd-carboxylate at a specific temperature determined by the length of the carbon chain of the corresponding carboxylic group (*i. e.* the reaction temperature of using cadmium myristate is above 220 °C). By maintaining the reaction temperature and applying vigorous stirring, the monomers react with the excess precursors left in the solvent, gradually growing into bigger nanocrystals. Since the monomer creation processes (nucleation processes mentioned in section 1.3.1) always exists, as the reaction time

Table 3.1.
Chemicals used in the zinc-blende CdSe/CdS QDs synthesis. Acetone and toluene were used to perform the washing and cleaning processes of the QDs and the glassware, they were not directly used in the synthesis processes.

Chemical's name	Purity	Vendor	Abbreviation
Acetone	99.5%	Sigma-Aldrich	
Cadmium oxide	99.999%	Strem Chemicals	CdO
Cadmium diethyldithiocarbamate	96%	Gelest	$Cd(DDTC)_2$
Cadmium formate	98%	Gelest	CdFt
Dodecane	98%	Sigma-Aldrich	
Hexane anhydrous	95%	Sigma-Aldrich	
Methanol anhydrous	99.5%	Sigma-Aldrich	
Myristic acid	99%	Sigma-Aldrich	MA
Oleic acid	90%	Sigma-Aldrich	
Oleylamine	70%	Sigma-Aldrich	OAM
Octylamine	98%	Sigma-Aldrich	
Selenium dioxide	99.9%	Sigma-Aldrich	SeO_2
Tributylphosphine	95%	Sigma-Aldrich	TBP
1-octadecene	90%	Sigma-Aldrich	

increases, if no further action is taken, the size distribution of the QDs becomes more and more dispersed. Different from the "hot-injection" method, to harvest QDs with better monodispersity in size distribution, a small amount of oleic acid is introduced to reduce the reaction speed to a level where the creation process of monomers is eliminated [91], only allowing the growth of existing QDs. The typical dispersity on the size distribution of the method is 5% [91]. To eliminate surface defects, CdSe cores were coated with a CdS shell and finished with a monolayer of cadmium formate to perfect the samples' QY.

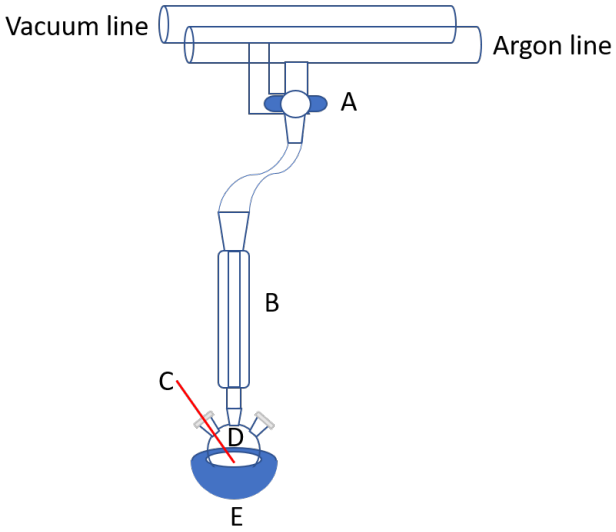

Figure 3.1. Schematic of QDs synthesis setup. A: double-line manifold; B: Liebig condenser; C: thermometer; D: 50 mL 3-neck flask; E: heat mantle.

3.1.1 Chemicals for synthesis and precautions to be observed

The chemicals used in the synthesis are listed in table 3.1. Selenium dioxide (SeO_2) must be stored with desiccant as it efficiently absorbs water from air, ruining the quality of the synthesized QDs. Most chemicals used in QDs synthesis are toxic, they must be operated inside a fume hood. The person who is synthesizing QDs must wear protective clothes, including nitrile gloves, goggles and lab coat. Dodecane and tributylphosphine (TBP) are highly flammable, they must be operated under an inert gas environment.

3.1.2 Synthesis equipment setup

The setup is schematically shown in Fig. 3.1. The synthesis was performed in a 50 ml 3-neck flask. A side neck of the flask was covered by a silicone-rubber septum (Sigma-Aldrich), allowing the injections of chemicals. The other side neck was connected to a glass adapter to hold a thermometer to monitor the temperature

of the reaction mixture. The glass adapter is made from a nuclear magnetic resonance (NMR) test tube, which size is small enough to fit inside the septum with an air tight joint.

The synthesis environment needs to be switched between low pressure ($\sim$ 20 mbar) and inert gas atmosphere. It was achieved by using a glass double-line manifold. Low pressure was obtained by a diaphragm pump (Pfeiffer MVP-035-2). A needle valve was installed in the vacuum line to regulate the pressure in the range of $10 - 100$ mbar, precluding significant evaporation of the solvents. To protect the pump from the chemicals, a cold trap cooled with dry ice-acetone mixture was installed before it. Argon (Ar, 99.999% purity, Praxair) was used for inert gas protection and was exhausted through a gas bubbler filled up with mineral oil to prevent Ar reflux. Before connecting the flask to the manifold, a Liebig condenser was mounted between them, to recirculate chemicals evaporated due to the elevated reaction temperature. Heat was generated from the heat mantle (where the flask is seated) and powered by a PID (proportional-integral-derivative) controller system (Briske Heat SDC 120JC-A). The feedback loop was established by attaching the controller's thermometer to the contacting surface between the flask and the heat mantle. The temperature of the solvent is measured with another digital thermometer through the glass adapter. A temperature difference was expected and observed between the solvent and the heat mantle, the calibration data is listed in table 3.2. The tests were carried out with 20 mL solvent loaded into the flask. The solvent was stirred by a magnetic stirrer at a speed of 800 rpm. This process was implemented by heating up the solvent from room temperature to the target value using the maximum output power of the controller. Therefore, the values recorded are considered as worst case senarious of the system. In standard synthesis, deviations as small as $\pm 1\,^{\circ}\mathrm{C}$ were achieved in any applicable temperature range with real-time adjustment of the controller, such as dividing the heating process into multiple stages.

Table 3.2.
Calibration data of the temperature control system. During the test, 20 mL ODE was loaded into the flask with magnetic stirring at a speed of 800 rpm. The solvent temperatures are the target values and the deviations are obtained as the maximum temperature difference from the target values observed during the test. The data was obtained by heating the solvent from room temperature to the target temperature with the maximum heating power.

Solvent temperature (°C)	Heat mantle temperature (°C)
$50 + 5/-1$	$90 + 35/-5$
$80 + 2/-1$	$135 + 30/-5$
160 ± 1	$295 + 26/-5$
246 ± 1	$390 + 20/-5$

3.1.3 Preparation of chemicals

The quantity of each solid chemical was measured by a balance (Mettler AE240) with a reading precision of ± 0.00001 g. Limited by operator's skill, the quantity of the chemicals used in the experiment had a typical deviation of ± 1 mg from the required values. Liquid chemicals were measured with a glass syringe (Hamilton Gastight syringe model 1010) with a readout accuracy of 0.1 mL. All chemical quantities listed in this thesis without any specific indication represent required values with deviations discussed above.

The reaction mixture would be contaminated by air (particularly oxygen) dissolved in the chemicals, damaging the quality of the produced QDs. Consequently, chemicals used in the synthesis must be pre-degased before the reaction procedure, except for the ones which are stored under inert gas protection with a sure-seal cap (*i. e.* TBP and methanol anhydrous).

Two kinds of precursor solutions ($Cd(DDTC)_2$ solution and CdFt solution) and two stabilizers (oleic acid solution and Dodecane-octylamine mixture) were injected during the reaction. Therefore, they need to be prepared before the synthesis.

•Oleic acid solution: 0.1 mL was added into 0.5 mL OAM. Then the solution was degased under vacuum (100 mbar) for 1 hour followed by an argon purge (inject argon into the solvent while vacuuming) for 10 s to remove dissolved air.

•Dodecane-octylamine mixture: 2.4 mL dodecane and 7.6 mL octylamine were mixed and degased under vacuum (100 mbar) for 1 hour followed by an argon purge.

•$Cd(DDTC)_2$ solution (0.15 mol/L): 0.613 g (1.5 mmol) of $Cd(DDTC)_2$ was dissolved into 10 mL mixture of OAM and octylamine (volume ratio of 1:1). Then the solution was degased under vacuum (100 mbar) for 1 hour followed by an argon purge.

•CdFt solution (0.15 mole/L): 121.4 mg (0.6 mmol) was dissolved into 4 mL octylamine. Then the solution was degased under vacuum (30 mbar) for 1 hour followed by an argon purge.

3.1.4 Zinc-blend CdSe seeds synthesis

The procedure of CdSe seed synthesis is well documented [92]. Minor modification were introduced to the existing procedure according to our lab conditions. The steps of the procedure are:

1. 39 mg of CdO, 137 mg of MA and 5 ml of ODE were loaded into the 50 ml 3-neck flask. Then the mixture was degased at 90 °C at 100 mbar for 30 min to remove dissolved air.

2. The reaction mixture was heated up to 250 °C (about 17 °C/min) while stirring at 800 rpm under argon flow.

3. After the reaction mixture showed a clear pale yellow (Cd-myristate) color, the heat mantle was removed, and the mixture was allowed to reach room temperature (typically within an hour or 10 min with air cooling).

4. Another 37 ml of ODE was added into the flask.

5. The reaction mixture was degased for 30 min at 90 °C at 100 mbar to remove the dissolved air inside the newly added ODE.

6. 33 mg SeO_2 was added swiftly into the flask.

7. The reaction mixture was degased for 30 min at 50 °C at 100 mbar to remove the air introduced in step 6.

8. The vacuum line was closed and Ar flow was established into the flask to provide inert gas protection. The reaction mixture was heated up to 220 °C at a rate of 20 °C per min. When the mixture reached the temperature of 220 °C, a rapid change in solution's color from yellow to red was observed, indicating the nucleation of CdSe seeds.

9. As the color started to change, 0.1 mL oleic acid was injected, with a rate of one droplet[1] every ten seconds to gradually reduce the reaction speed (slow growth rate reduces the structural defects introduced during the synthesis), and provide stability to the existing CdSe seeds (oleic acid is strongly bonded to the Cd dangling atoms, increasing the spatial separation between seeds).

10. The reaction mixture was allowed to react for another 30 min at 220 °C after the injection to get seeds with size around 3.0 nm [92]. Larger seeds can be achieved by extending the reaction time.

11. The reaction was stopped by removing the heat mantle. The reaction mixture was allowed to cool to room temperature (typically within an hour).

A ±10 meV deviation for the absorption edge was found in the absorption spectra of different batches synthesized with identical reaction time (step 10), while identical deviation (the same direction and amplitude) was found in their respective PL spectra. On the other hand, the size of the QDs can also be adjusted by changing the amount of ODE added in step 4 (changing the precursors' concentration). The test details are shown in table 3.3. According to the data, good consistency was observed in our QDs production. Typical PL and absorption spectra are shown in Fig. 3.2(a) (sample from test batch 2), where a well defined absorption maximum was observed at the absorption edge, indicating the existence of CdSe QDs. However, a limited, but long low energy tail was observed in the PL spectrum. It is reasonable as no

[1] 10.3 μL with a 21 gauge syringe needle. The amount of solvent per droplet was determined by counting the number of droplets (97) one by one for 1 mL of the solution being ejected from the syringe.

Table 3.3.
Energies of QDs samples' first absorption maximum with different synthesis condition. Test batches 1, 2 and 3 were carried out to check the repeatability of the core synthesis procedure. Test batch 4 was carried out with longer synthesis time, test batch 5 was carried out with higher precursor concentration.

Test batch	Reaction time (min)	ODE added (mL)	Energy of the first absorption maximum (eV)
1	30	42	2.25
2	30	42	2.24
3	30	42	2.24
4	45	42	2.20
5	30	19	2.21

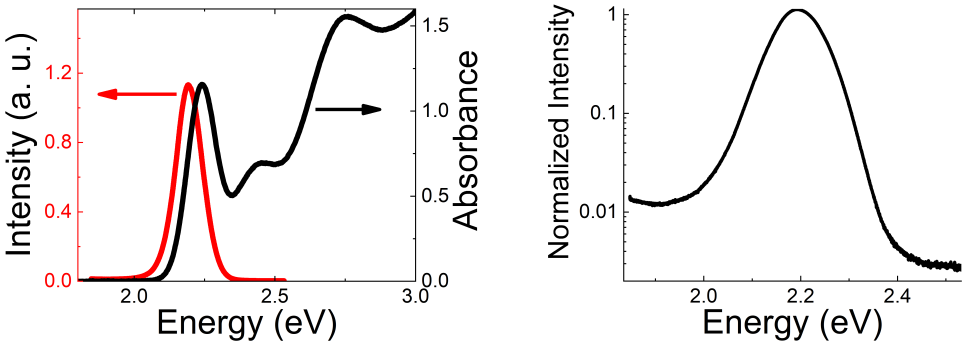

(a) (b)

Figure 3.2. (a) Absorption (red curve) and PL (black curve) spectra of CdSe seeds synthesized in our lab. (b) Normalized PL spectrum plotted in logarithm scale. The QDs sample used was synthesized in test batch 2. The PL spectrum was obtained with $\varepsilon_{ex} = 3.05$ eV

surface treatment was yet applied to the CdSe QDs. To perfect the QDs' quality, surface passivation was carried out.

3.1.5 Washing process of CdSe seeds

Limited by the size of the flask, 20 mL seeds suspension was kept for the washing process (in the case where 19 mL ODE was added in total, all the seeds were kept). It was performed within the same flask used for seed synthesis to prevent possible oxidation [1]. All steps were performed in Ar gas flow. The steps are:

1. 0.3 mL of TBP and 0.3 mL of octylamine were added into the flask to remove the molecular ligands attached to the seeds' surface[2].

2. 6 mL anhydrous hexane and 12 mL anhydrous methanol were added into the flask to separate the TBP, oleic acid, octylamine and possible byproducts (ketone) from the suspension.

3. The mixture was heated up to 50 °C while stirring at 800 rpm for 5 min.

4. Stirring was stopped, while keeping the temperature of the mixture at 50 °C. The mixture separated into two layers, where the top red layer is mainly ODE containing CdSe seeds and the methanol bottom layer dissolving the TBP, octylamine and other byproducts. The bottom layer was removed by using the syringe.

5. Steps 2 to 4 were repeated once more to ensure the removal of the injected TBP and octylamine.

6. Steps 1 to 5 were repeated once more, then the cleaned seed suspension was heated to 60 °C and the pressure was reduced to around 50 mbar to remove the excess methanol and hexane left in the solvent[3].

After the cleaning procedure, typically 10 mL suspension with seeds was left in the flask.

[2]TBP solvent was directly withdrawn from the container by using a syringe through the sure-seal cap. The syringe must be cleaned and filled with inert gas before being operated.

[3]The pressure must be regulated above 10 mbar during the vacuum process. Otherwise, solvents other than hexane and methanol would also be significantly removed through evaporation. Furthermore, with a pressure lower than 10 mbar, the flask would be significantly cooled down due to the violent evaporation of methanol.

3.1.6 CdS shell growth

The shell growth procedure was developed by Peng's group [1,2]. It was modified by us to better adapt it to our conditions. The concentration of CdSe seeds $\mathcal{C}_{\text{seed}}$ were determined by the extinction rate of the sample at 340 nm using the semi-empirical equations [40]

$$\begin{aligned} \varepsilon_{\text{g}} &= 1.74 + \frac{1}{0.89 - 0.36r_{\text{core}} - 0.22r_{\text{core}}^2}, \\ \varsigma &= 154400r_{\text{core}}^3, \end{aligned} \tag{3.1}$$

where ς (L/(mol· cm)) is the extinction coefficient of the CdSe seeds, ε_{g} is in eV, and r_{core} is in nm. Thus, $\mathcal{C}_{seed} = \mathcal{A}/(\varsigma d_{\text{cuv}})$, where d_{cuv} is the size of the cuvette used for the absorption test, and $\mathcal{A}$ denotes the measured absorbance. According to the calculation, the amount of Cd(DDTC)_2 solution (the precursor of the CdS shell) was calculated by using the method suggested by Chen *et al.* [93]. Here the thickness of the CdS layer was estimated with the bulk material parameter of 0.35 nm [69], and by considering the QDs to be perfect spheres, the volume $\mathcal{V}_{\text{mo}}(\text{n})$ of the n^{th} CdS monolayer is given by

$$\mathcal{V}_{\text{mo}}(n) = \frac{4\pi}{3}\Big\{\big[r_{\text{core}} + \text{n} \times 0.35\,\text{nm}\big]^3 - \big[r_{\text{core}} + (\text{n}-1) \times 0.35\,\text{nm}\big]^3\Big\}, \tag{3.2}$$

Thus the number of CdS molecules, n_{CdS} needed for growing the monolayer is

$$\text{n}_{\text{CdS}} = \frac{\mathcal{V}_{\text{mo}}}{\mathcal{V}_{\text{CdS}}}\mathcal{V}_{\text{seed}}\mathcal{C}_{\text{seed}}. \tag{3.3}$$

Where $\mathcal{V}_{\text{seed}}$ denotes the volume of the CdSe seed suspension. Since one mol of Cd(DDTC)_2 provides one mol of Cd^{2+}, the volume of Cd(DDTC)_2 solution, $\mathcal{V}_{\text{Cd}}$ needed for growing the monolayer is given by

$$\mathcal{V}_{\text{Cd}} = \frac{n_{\text{CdS}}}{0.15\text{mol/L}}. \tag{3.4}$$

With the typical $r_{\text{core}} = 1.5$ nm, $\mathcal{C}_{\text{seed}} \approx 1.5 \times 10^{-5}$ mol/L and $\mathcal{V}_{\text{seed}} = 20$ mL, the amount of Cd(DDTC)_2 solution for the 1st, 2nd, 3rd and 4th CdS layers are 113 μL, 216 μL, 350 μL and 515 μL respectively.

The steps for the procedure are:

1. 10 ml pre-degased dodecane and octylamine mixture were loaded into the flask with the washed CdSe seeds.

2. The temperature was raised to 80 °C (about 10 °C/min) while stirring at 800 rpm, the required amount of $Cd(DDTC)_2$ solvent was added to grow a single monolayer of CdS. The temperature was maintained for 5 min to allow the $Cd(DDTC)_2$ molecules to attach to the seeds.

3. The mixture was then heated up to 140 °C as quickly as possible while stirring to initiate the reaction of the shell growth. After the temperature reached 140 °C, it was maintained for 20 min to complete the growth process. Then the mixture was allowed to be cooled down to 80 °C.

4. The attach-growth procedure (steps 2 and 3) was repeated until the desired thickness of the CdS shell has been achieved.

5. When finished, the heat mantle was removed to stop the reaction.

During the growth of the CdS shell, QY of the sample increases significantly. The effect was so noticeable that after the growth of the first CdS monlayer, fluorescence of the QDs can be observed with white light, resulting in a glittering appearance of the suspension (similar to high QY dye solutions, such as Rhodamine 560). It was also used as a quality check of the seed synthesis and cleaning procedure. However, each $Cd(DDTC)_2$ molecule contains one Cd and four S atoms ($Cd(DDTC)_2$ is the precursor for both Cd and S), excesive amount of S was provided to the reaction mixture, generating unwanted byproducts, such as H_2S. To perfect the following surface passivation procedure, an extra cleaning process is required.

3.1.7 Surface treatment of the CdSe/CdS (core/shell) QDs

H_2S is a byproduct generated during CdS shell growth. Peng *et al.* [2] suggested that this byproduct can optically quench the QDs by providing ion-traps on QDs'

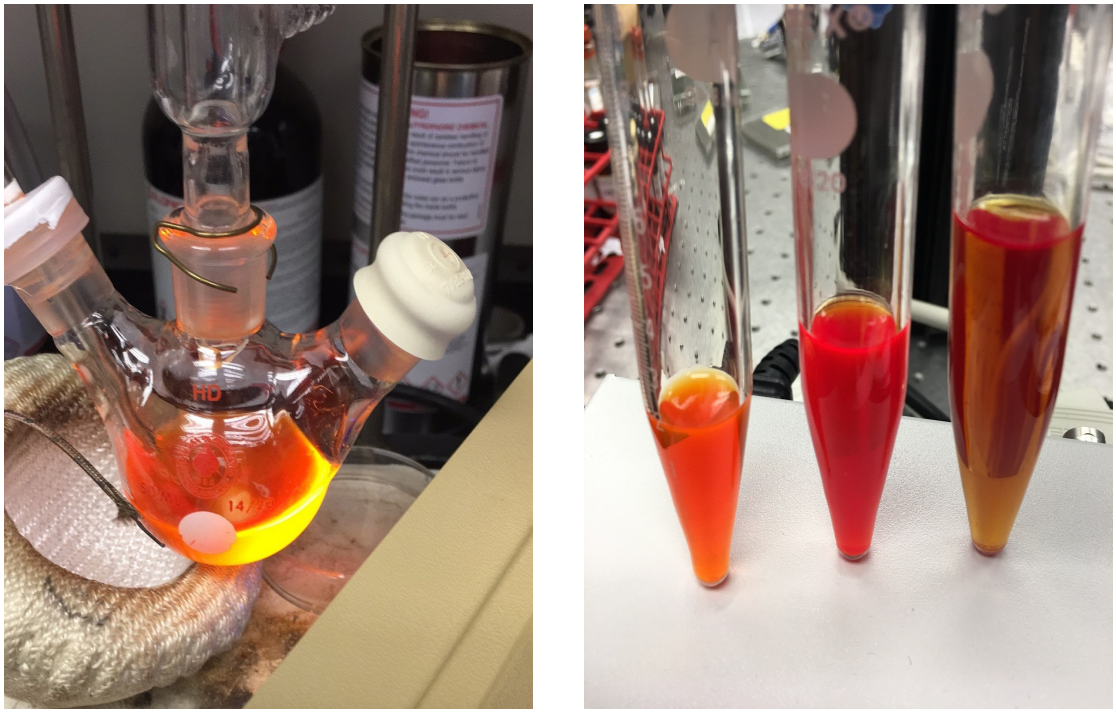

(a) (b)

Figure 3.3. Pictures of the CdSe/CdS QDs samples synthesized in our lab. (a) The sample right after synthesis (the bright yellow band is obtained by illuminating with an UV lamp from the bottom right side) (b) Three batches of CdSe/CdS QDs samples. The shell thickness of the orange (left), red (middle) and brown (right) samples are identical (4 monolayers) with $r_{\text{core}} \approx 1.33$ nm (orange), 1.52 nm (red) and 1.62 nm (brown) respectively. r_{core} is determined by using the "partical-in-a-sphere" model.

surfaces. Ar purging has been proved to be an efficient way to remove H_2S from the suspension.

To further improve the QY of QDs, CdFt was used to finish the surface treatment [1,2]. Its amount was calculated by considering it as the fifth CdS monolayer, leading to a typical value of 690 μL. The specific steps are:

1. The solvent was purged with Ar at 80 °C (H_2S can be removed more effectively at high temperature, but a temperature above 80 °C may lead to undesired growth in CdS) for 15 min to remove the H_2S generated during the synthesis.

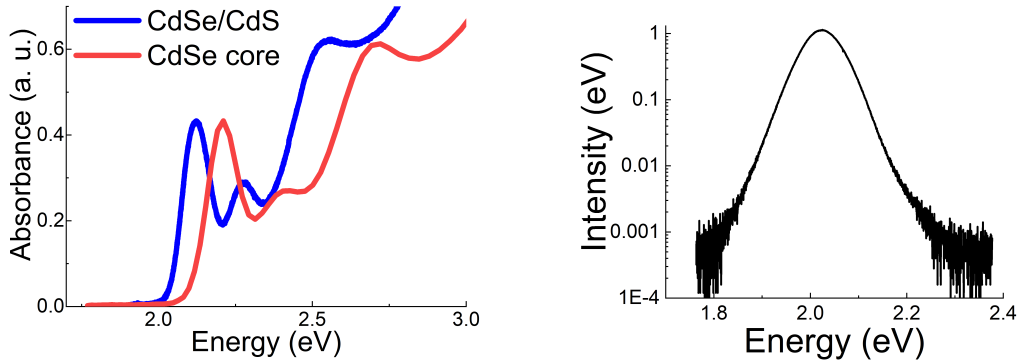

(a) (b)

Figure 3.4. (a) Absorption spectra of the CdSe QDs sample before (red) and after (blue) growth of CdS shell. The sample was synthesized on Jan-4-2018, with $r_{\text{core}} \approx 1.32$ nm ($\varepsilon_{\text{g}}^{\text{eff}} = 2.13$ eV) and an 80 meV red shift was observed in QDs absorption spectra after the shell growth. (b) PL spectrum plotted in logarithm scale. The sample was from batch 2. The PL spectrum was obtained with $\varepsilon_{\text{ex}} = 3.05$ eV.

2. 690 μL of CdFt solution was added.

3. The QD suspension was heated up to 50 °C (about 5 °C/min) for 10 min to complete the attachment of the CdFt.

4. The heat mantle was removed to stop the process.

5. Finally, the argon purged QDs suspension was transferred into amber glass vials with inert gas protection.

A picture of the sample ($r_{\text{core}} \approx 1.32$ nm) after complete synthesis is shown in Fig. 3.3(a). The existence of QDs was proved by illuminating the suspension with a UV lamp, where a bright stripe was observed on the right bottom corner facing the UV lamp. This and other two samples with different sizes, $r_{\text{core}} \approx 1.52$ nm (red) and 1.62 nm (brown) respectively, are shown in Fig. 3.3(b). Here r_{core} is determined by using the "particle-in-a-sphere" model.

Typical absorption spectra of the CdSe seeds and corresponding CdSe/CdS sample are shown in Fig. 3.4(a) (from batch 1, absorption spectra of samples from different batches are shown in the appendix). A redshift and narrowing of the sample's ab-

sorption features are observed, indicating a successful growth of CdS shell with size narrowing effect [1]. On the other hand, no observable absorption feature associated to CdS was found, indicating there is no nucleation of CdS seeds during the shell growth procedure. The PL spectra of the CdSe/CdS QDs is shown in Fig. 3.4(b). The low energy tail observed in CdSe seed's PL spectrum has disappeared, showing strong evidence of complete surface passivation.

QDs ensembles' first absorption maximum (defined as the absorption edge) and PL spectral center (defined as the PL emission energy) are used to describe the samples. There were six batches of CdSe/CdS samples in total synthesized in our lab, which information is listed in table 3.4. There's about 0.1 nm difference in QDs' effective radius estimated by Eq. 3.1 and the "particle-in-a-sphere" model. The values derived from the "particle-in-a-sphere" model was used instead of as the lattice structure is more distorted (expansion) close to the surface (one end is free), expecting a core contraction after the shell growth. On the other hand, it needs to be pointed out that the difference between Eq. 3.1 and the "particle-in-a-sphere" model can be removed by adjusting the intrinsic band gap value to 1.7 eV, as reported in Sze's book [94]. Spectroscopic techniques used to acquire the data will be discussed in section 3.3 and 3.5.

3.2 X-ray diffraction (XRD) test

The crystal structure of the QDs seeds were determined by XRD (Bruker D8 Discover A25). QDs samples were cleaned twice with methanol before XRD measurements to remove the oleic acid and other ligands inside the suspension, hence reducing background noise. After cleaning, the sample was first transferred into hexane, then deposited onto a piece of (100) silicon wafer. To get enough signal from the QDs sample, multiple depositions were performed, followed by air-drying to create a thick (hundreds of μm) layer of stacked QDs. The XRD scanning rate was chosen to be 0.5 s to 1 s per 0.02 deg in 2θ. Power of the X-ray beam was set to be 50 kW. A

Table 3.4.
PL information of the QDs synthesized in six batches.

Batch	Absorption energy (ev)	PL emission energy (eV)	Effective core radius (nm)
1	2.133	2.077	1.33
2	2.059	2.021	1.52
3	2.022	1.981	1.62
4	2.129	2.077	1.34
5	2.053	2.010	1.53
6	2.097	2.048	1.41

typical result is shown in Fig. 3.2, where three broad peaks can be observed at 2θ

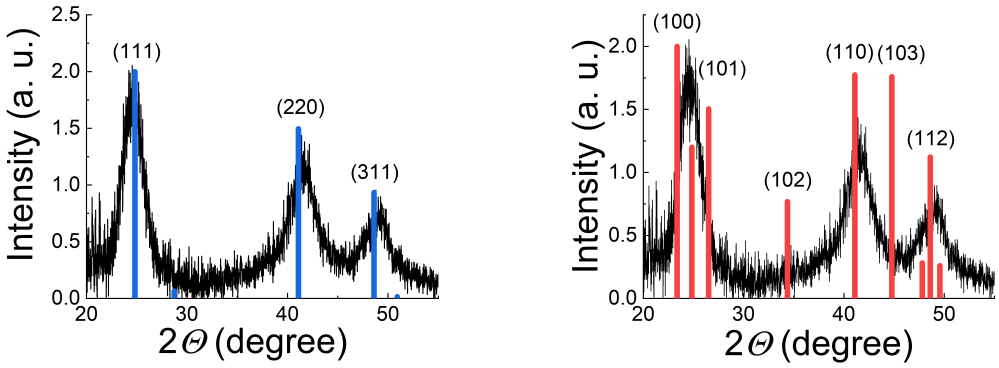

(a) (b)

Figure 3.5. Typical X-ray diffraction result of the homemade CdSe seeds with the characteristic XRD signal of CdSe with (a) zinc-blende crystalline structure (blue), (b) wurtzite crystalline structure (red).

values of 25°, 43° and 50°, which correspond to the characteristic signals of the (111), (220) and (311) directions of the zinc-blende CdSe crystals. The broadening of the peaks arises from the limited periodical structure of the QDs due to their small size. When comparing to the characteristic signals of wurtzite CdSe crystals (Fig. 3.5(b)),

missing (102) and (103) peaks is a strong evidence of the absence of the wurtzite crystalline structure for the QDs. The signal from the (100) silicon substrate was obtained by scanning the silicon wafer only in the same orientation and with the same parameters, then subtracted from the sample's XRD result. As a conclusion, grown CdSe QDs do have zinc-blende crystalline structure.

3.3 Absorption spectroscopy

The information of QDs samples' band edge was obtained using absorption spectroscopy. During an absorption test, the spectrometer compares the light intensity passing through an optical window with (I_s) and without (I_0) the sample. The data is typically recorded in the form of absorbance, $\mathcal{A} = -\log\frac{I_\mathrm{s}}{I_0}$. Quartz cuvettes with 1 cm optical path were used as the sample holders for absorption spectroscopy experiment.

In the case of CdSe seeds, although the Ar flow was on during the entire synthesis, observable degradation (precipitation of ligands) was observed overnight. To minimize the time gap between the seed synthesis and the following cleaning and coating procedures, absorption spectroscopy was performed right after synthesis (Varian Cary 50 Bio UV-visible spectrometer was used as a field equipment). For the same reason, the spectral resolution was set to be 1.5 nm with a scanning rate of 60 nm/s to provide a fast scan. The scanning light of the spectrometer is generated by a built-in Xenon lamp working together with a monochromator. The baseline of the absorption spectra I_0 was obtained by scanning a cuvette loaded with hexane only. Then the sample was diluted in hexane 20 times by volume as the raw suspension of the seeds was too concentrated to achieve an $\mathcal{A}$ value within the dynamical range of the spectrometer (diluting the sample by 20 times was empirical).

The absorption spectra of the CdSe/CdS QDs samples were obtained by using a Thermal Scientific Evolution 600 UV-Vis spectrometer. The base absorption line I_0 was obtained by testing the cuvettes with solvent (*i. e.* hexane) only. After that, typically 100 μL of the QDs suspension was added into the same cuvette to derive

a maximum absorbance in the range of $1.5 \sim 3$ (an apparatus error occur when the absorbance is higher than 3, and the signal to noise level is not good below 1.5). The light source of the spectrometer is a built-in Xenon lamp sent through the built-in monochromator followed by a slit to generate a 2 nm bandwidth beam. The spectral resolution was chosen to be 0.1 nm at a scanning rate of 1 nm/s. As the scanning time was long enough, the collected data was already averaged by the machine (20 data points for each pixel) before saving the data.

3.4 Photoluminescence quantum yield measurement

PL QY describes the efficiency of the induced exciton to decay radiatively. To measure the QY of our QDs samples, a relative method was used [95]. The method assumes that for a given experimental setup the collection efficiency through PL emission is fixed for all samples. Therefore, the total PL intensity,$I_{\mathrm{PL}}^{\mathrm{total}}$ and the absorption of the excitation light $\mathcal{A}(\varepsilon_{\mathrm{ex}})$ satisfy the relation,

$$I_{\mathrm{PL}}^{\mathrm{total}} = \Lambda \eta \mathcal{A}(\varepsilon_{\mathrm{ex}}), \tag{3.5}$$

where Λ is the collection coefficient determined by the experimental setup. By assuming Λ only depends on the geometry of the system, a dye solution with well documented QY η_{ref} is introduced as the reference for the measurement,

$$I_{\mathrm{PL,\,ref}}^{\mathrm{total}} = \Lambda \eta_{\mathrm{ref}} \mathcal{A}_{\mathrm{ref}}(\varepsilon_{\mathrm{ex}}). \tag{3.6}$$

In the fluorescence spectrometer, the collection window (round shape) faces one side of the cuvette. As shown in Fig. 3.6, only PL light emitted within the angle θ will enter the collection window. The cuvette's size is much smaller than the windows diameter, where

$$\sin\theta = \sin\theta_{\mathrm{c}} \sqrt{\frac{\epsilon}{\epsilon_{\mathrm{s}}}}. \tag{3.7}$$

θ_{c} denotes the maximum incident angle will enter the collection window from the cuvette's wall (refraction inside the cuvette's wall is ignored). ϵ_{a} and ϵ_{s} are the

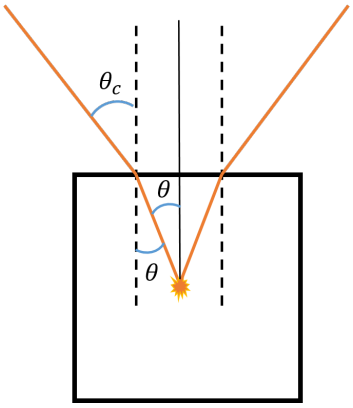

Figure 3.6. Schematic plot of the emission light path inside the fluorescence spectrometer (top view).

dielectric constants of the air and the suspension solvent respectively. Since θ_c and ϵ_a are fixed, then the solid angle Ω_c sub by the spectrometer is

$$\Omega_c = 2\pi \int_0^{\theta} \sin\theta' d\theta' = 2\sin^2\frac{\theta}{2} \approx 2\left(\frac{\theta}{2}\right)^2 = \frac{1}{2}\frac{\epsilon_a}{\epsilon_s}. \tag{3.8}$$

Here the condition that θ_c is small (the collection window is 10 cm away from the cuvette) was applied. Therefore, the sample's QY can be derived from Eq. 3.5, Eq. 3.6 and Eq. 3.8

$$\eta = \frac{I_{PL}^{toal}}{\mathcal{A}(\varepsilon_{ex})} \frac{\mathcal{A}_{ref}(\varepsilon_{ex})}{I_{PL,\,ref}^{total}} \frac{\epsilon_s}{\epsilon_{ref}} \eta_{ref}. \tag{3.9}$$

where, ϵ and ϵ_{ref} are the permittivities of the solvents for the sample and the reference dye respectively. In practice, the excitation provided by the PL spectrometer has a given bandwidth with a specific spectrum based on the type of lamp used. Hence, the effective absorption rate at the excitation energy should be redefined as

$$\mathcal{A}^{eff} = \int_{\varepsilon_{ex}-\delta\varepsilon}^{\varepsilon_{ex}+\delta\varepsilon} \mathcal{A}(\varepsilon_{ex}) d\varepsilon_{ex}. \tag{3.10}$$

$\varepsilon_{ex} \pm \delta\varepsilon$ is the upper/lower limit of the energy of the excitation light. On the other hand I_{PL}^{total} is derived by integrating the whole PL spectrum,

$$I_{PL}^{total}(\varepsilon) = \int_{\varepsilon_-}^{\varepsilon_+} I_{PL}(\varepsilon) d\varepsilon, \tag{3.11}$$

where ε is the energy. Therefore, according to Eq. 3.10 and Eq. 3.11, Eq. 3.9 can be rewritten as,

$$\eta = \frac{\int_{\varepsilon_-}^{\varepsilon_+} I_{\mathrm{PL}}(\varepsilon)d\varepsilon}{\int_{\varepsilon_{\mathrm{ex}}-\delta\varepsilon}^{\varepsilon_{\mathrm{ex}}+\delta\varepsilon} \mathcal{A}(\varepsilon_{\mathrm{ex}})d\varepsilon_{\mathrm{ex}}} \frac{\int_{\varepsilon_{\mathrm{ex}}-\delta\varepsilon}^{\varepsilon_{\mathrm{ex}}+\delta\varepsilon} \mathcal{A}_{\mathrm{ref}}(\varepsilon_{\mathrm{ex}})d\varepsilon_{\mathrm{ex}}}{\int_{\varepsilon_-}^{\varepsilon_+} I_{\mathrm{PL,ref}}(\varepsilon)d\varepsilon} \frac{\epsilon_{\mathrm{s}}}{\epsilon_{\mathrm{ref}}}\eta_{\mathrm{ref}}.$$

To increase the precision of the measurement, $I_{\mathrm{PL}}^{\mathrm{total}}$ and $\mathcal{A}^{\mathrm{eff}}$ are measured with different concentrations of the sample and the reference dye. As a function of concentration $I_{\mathrm{PL}}^{\mathrm{total}}$ is linear in $\mathcal{A}^{\mathrm{eff}}$,

$$I_{\mathrm{PL}}^{\mathrm{total}}(\varepsilon) = s \times \mathcal{A}^{\mathrm{eff}}(\varepsilon) + y_0. \tag{3.12}$$

In Eq. 3.12, y_0 should be zero, a good indicator for a proper measurement. The QY of the sample η can be calculated with the slopes, s, s_{ref} of the linear fits of the data points for the sample and reference respectively,

$$\eta = \frac{s}{s_{\mathrm{ref}}} \frac{\epsilon_{\mathrm{s}}}{\epsilon_{\mathrm{ref}}}\eta_{\mathrm{ref}}. \tag{3.13}$$

PL and absorption spectra of the QDs are usually heavily overlapped, such that re-absorption processes are significant when the concentration of the sample is high. According to our experiments, the effect of the re-absorption can be neglected when the absorbance of the excitation light is less than 0.15 (equivalent to 29% abosrption rate). As shown in Fig. 3.7, significant non-linearity was observed when the sample's absorbance is higher than 0.15. On the other hand, PL and absorption spectra of the reference dye used in the measurement should be similar to the ones of QDs samples to ensure the assumption of the identical geometrical Λ value.

Absorption measurements were carried out with the same absorption spectrometer used for the CdSe/CdS QDs samples absorption spectroscopy. PL spectra were taken with a Varian Cary Eclipse Fluorescence Spectrometer system. Limited by the lab condition Rhodamine 560 (also known as Rhodamine 110) dye purchased from Exciton was used as the reference dye in our measurement. The absorption and emission spectra of the dye is around 530 nm, which is much a higher energy than the absorption edge of the QDs samples. Meanwhile, due to the configuration of the QDs, surrounded with CdFt, the surface ligands could be detached with heavy dilution (diluted more than 1 : 300), degrading the QDs' QY significantly. Therefore, the test

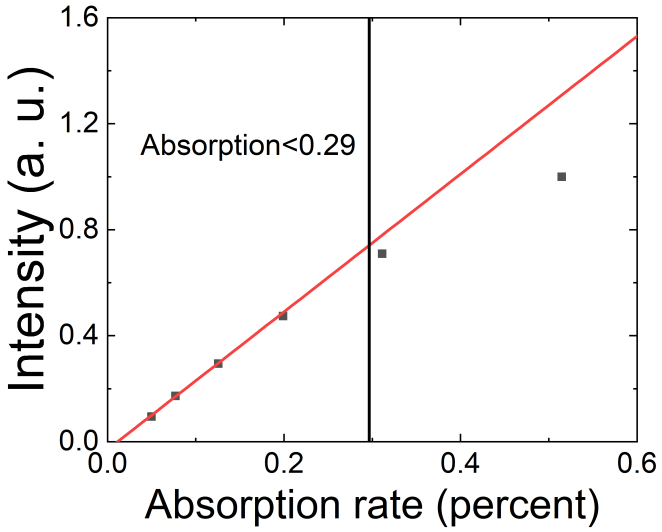

Figure 3.7. Plot of the sample's PL intensity versus absorption. Data was obtained with the QDs synthesis in batch 2 with excitation wavelength of 495 nm.

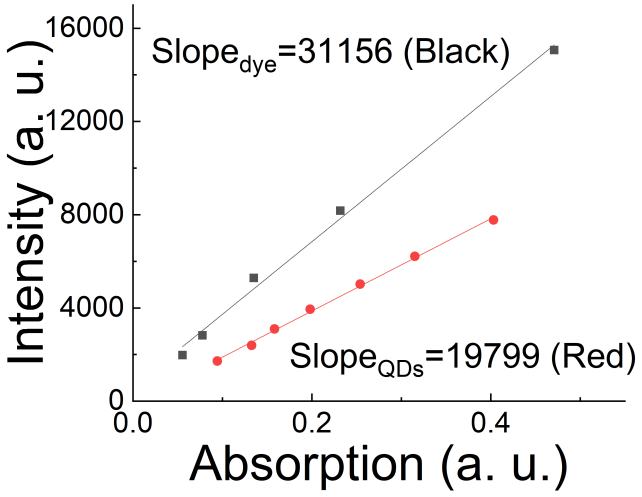

Figure 3.8. QY measurement data of the QD samples from batch 1. Black squares: dye, red dots: QDs.

was used as an rough evaluation of the QD quality. The dye was dissolved in ethanol (70%, Sigma-Aldrich), with a well documented QY of 0.92 [96] and diluted to the

Table 3.5.
Samples' QYs measrued with the relative method.

Batches	QY (%)	Nominal size (nm)
1	47.5	1.33
2	60.7	1.52
3	55.5	1.62
4	52.3	1.34
5	39.7	1.53
6	59	1.41

proper concentration values. QDs samples were diluted with hexane to 1 : 300 of the original concentration at the beginning, and diluted by another 1 : 2 to 1 : 10 according to the former absorption measurement. The samples and the dye solution were loaded in the quartz cuvettes mentioned before. Data of a typical QY measurement of the sample from batch 1 is shown in Fig 3.8, where both the sample (red dots) and the dye (black squares) solution's PL intensity was found to be linearly dependent on the absorption. The measurement results of all the batches are shown in table 3.5. Except for batch 5, a QY around $50-60\,\%$ was observed in all batches, and best QY were achieved in the batches with nominal size larger than 1.4 nm (except batch 5), however, not enough for OR.

As mentioned above, the dye solution used was improper, the measurement did not provide a reliable result for our samples. Furthermore, the QY of QDs has been found to be significantly higher at SBE (QDs' QY approaches unity as the excitation energy decreases below the absorption edge [97, 98]), since non-radiative pathways are reduced. Among different batches, however, their quality can be evaluated with their relative measured QY values. Therefore, samples from batch 2 were used as the candidate for OR experiments.

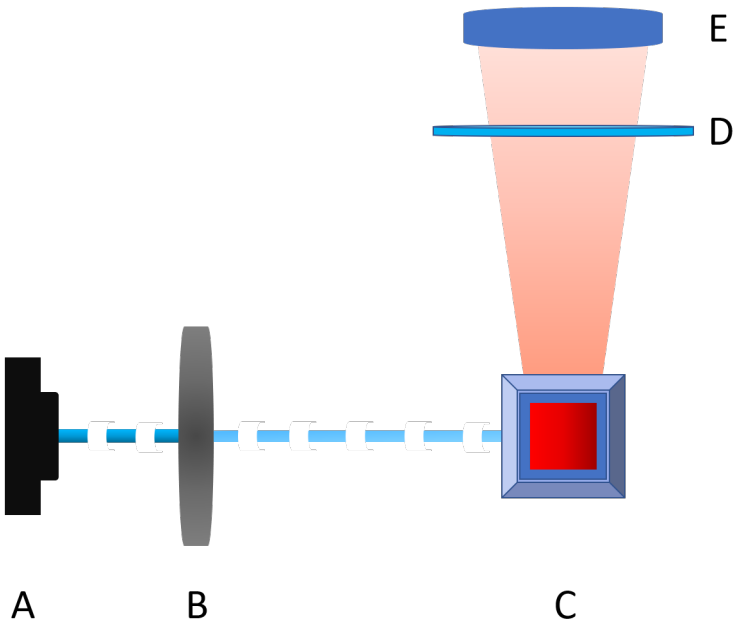

Figure 3.9. Schematic plot of the fluorescent lifetime system. A: Horiba 405 nm delta diode, B: neutral density filter, C: cuvette mount, E: long pass filter (to filter out excitation light), D: photo detector.

3.5 Photoluminescence lifetime measurements

The PL lifetime of the QDs samples was measured by doing time-resolved PL experiments. A Horiba Delta Pro Fluorescent Lifetime system was used to perform such measurement. The system works with a built-in Horiba 405 nm delta diode as the excitation light source, generating as short as 15 ps pulses. A schematic plot is shown in Fig. 3.9, where the sample was placed in the cuvette. The excitation pulse generated from the laser diode was attenuated by the neutral density filter before reaching the sample. Fluorescent photons are detected perpendicularly to the excitation path with a long pass filter inserted to reduce the scattered and back reflected excitation light [99]. However to optimize the measurement, especially for fast decay processes, which are temporally close to the scattering and back reflection, silica particles with mean size of 40 nm suspended in hexane were used to obtain the instrumental response function (IRF). All test samples were loaded in quartz cuvettes

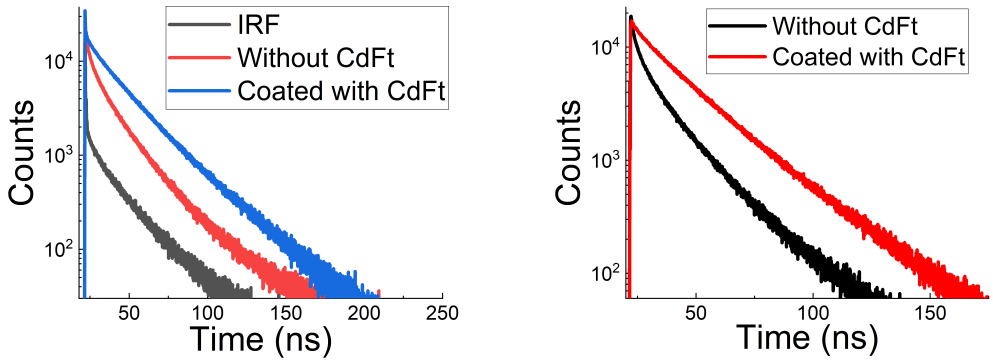

(a) (b)

Figure 3.10. (a) Decay curves of the instrumental response function(black), sample before CdFt treatment (red) and sample after CdFt (treatment). (b) Decay curves of the sample before (black) and after CdFt treatment (red) subtracted by the instrumental response function. The sample used in the test were from batch 1.

used for running the experiment with QDs. The concentration of the sample was controlled to give an absorbance value which is less than 0.1 [95] to ensure scattering and re-absorption are negligible. During the test, significant differences were found between samples with and without CdFt treatment. As shown in Fig. 3.10(a) where the IRF curve (black) is plotted together with the raw radiative decay data (red and blue). A much more linear profile in the log scare was observed in the sample after CdFt treatment. By taking into account the IRF, the samples' radiative decay lifetime was derived by exponentially fitting the data, where a radiative single decay lifetime of 24 ns was found. The observation agrees with the report from Peng's group [1], suggesting the successful production of high quality QDs.

3.6 Photoluminescence spectroscopy [100]

PL spectroscopy is the most critical measurement in our application, which provides information of our samples' PL mean emission energy. The optical thermometry for probing QDs's temperature without physical contact was also developed using this

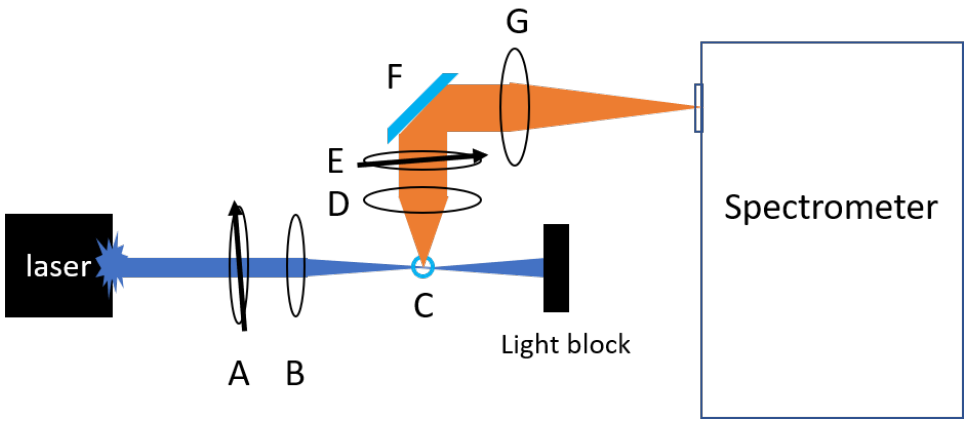

Figure 3.11. Schematic of photoluminescence spectroscopy. A: laser polarizer; B: focusing lens; C: capillary tube; D: collimating objective; E: analyzer; F: high-reflective mirror; G: adapting objective

technique. Regular PL spectroscopy with high energy excitation (ε_{ex} = 3.05 eV) is straight forward (the excitation energies is not inside the observable PL spectrum) and well documented. Therefore, this section is focused on the enhanced off-axis collecting system designed for SBE PL spectroscopy.

3.6.1 Enhanced off-axis collecting system

According to sections 1.5 and 2.4, net cooling can be potentially achieved in CdSe/CdS QDs with SBE. To examine it, the samples' PL properties under SBE needs to be evaluated. However, at SBE, the excitation energy is typically within the range of the PL spectrum. Since the laser light is much stronger than the PL signal, a homemade off-axis collecting system was built to avoid stray incident laser light. The collection schematic is as shown in Fig 3.11. A HeNe laser or laser diodes with emission wavelengths at 405 nm (3.05 eV), 635 nm (1.95 eV), 650 nm (1.91 eV) and 685 nm (1.81 eV) were used as different excitation sources. Laser diodes were powered by a Thorlabs LCD205C laser diode driver. A Thorlabs TEC200C temperature controller was used to control the temperature of the laser diodes and slightly tune their emission

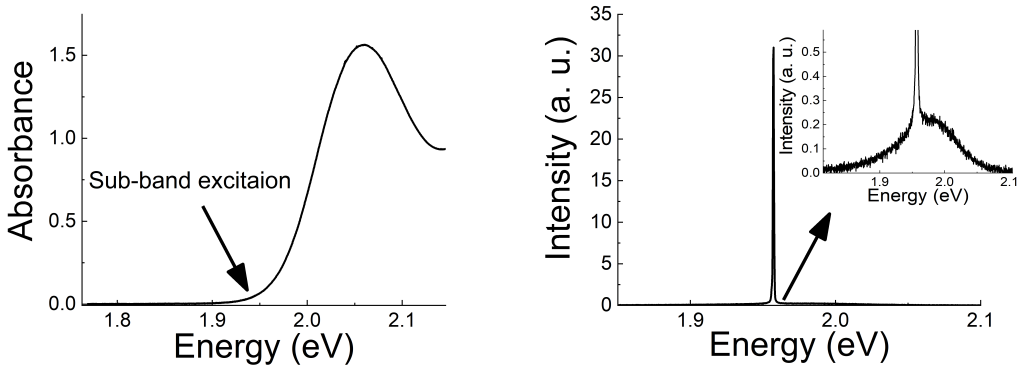

(a) (b)

Figure 3.12. (a) QDs' absorption strength at a typical sub-band excitation energy compared to their first absorption maximum. (b) Sub-band excitation photoluminescence spectra acquired with the off-axis collecting system without adding any polarizer. The insert plot is the negligible photoluminescence spectrum, when compared with the laser peak, shown in the same scale as the main plot.

energy by $\sim \pm 30$ meV. Due to the low absorption efficiency (as shown in Fig. 3.12(a), typical value is around 2% of the first absorption maximum), even scattered laser light is strong enough to affect the shape of the PL spectra (Fig. 3.12(b)). Therefore, further filtering is needed to separate PL and scattered laser light.

Since the QDs are small ($< 1/10$ of the excitation wavelength), the scattering is predominately Rayleigh scattering. Intensity of the scattered light by a single dot within the solid angle Ω, $I_{s,\Omega}$ is

$$I_{s,\Omega} d\Omega = \frac{\pi^4 d^6 I_{in}}{8\lambda^4} \sin^2\theta d\Omega \frac{(\epsilon - 1)^2}{(\epsilon + 2)^2}, \tag{3.14}$$

where d denotes the diameter of the QD, λ denotes the wavelength of the incident light, I_{in} is the intensity of the incident light, and ϵ denotes the permittivity of the material. The angle θ is between the polarization of the incident light and the direction of the scattered light. According to Eq. 3.14, $I_{s,\Omega}$ can be reduced by using smaller dots, excite the light with longer wavelength and making $\theta \to 0$. Smaller dots have larger size dispersity [41, 43], while the surface tension would also be enhanced

due to the larger curvature, which may cause structural defects (cracks) in QDs [101]. On the other hand, according to section 2.1, the effective energy band gap increases as the size of the QDs decreases. For this reason and also limited by the available light sources, making d much smaller is not an option. The wavelength of the incident light is constrained by the QDs' size and SBE, such that the adjustable range is also limited. To minimize the $\sin^2\theta$ term, the polarization of the incident light should be along the collection axis (the direction perpendicular to the laser beam and parrallel to the paper in Fig. 3.11). We define the orientation of sending incident light with its polarization along the collecting axis as P polarization and the perpendicular case as T polarization. Therefore, with P polarized incident light, the scattered light along the collecting axis would be zero. However, to maximize the collection efficiency of the PL light, the solid angle of light collection needs to be as large as possible, leading to a limited extinction ratio of the scattered light. To separate the PL light from scattered light, another property of Rayleigh scattering is used in the setup. In Rayleigh scattering, the polarization of the scattered light is along the θ direction of the incident light. The property does not help when the incident light is P polarized, where the scattered light is uniformly polarized along the radial direction in the view of the collimating objective (see Fig. 3.13(a)). In the case of T polarized incident light, the scattered light is polarized along the azimuthal direction (consider the collecting axis as the z-axis, see Fig. 3.13(b)). Although the intensity of the scattered light along the collecting axis is lager for T polarization, it is preferentially polarized in the direction perpendicular to the laser beam. Hence, after using a polarizer, the extinction efficiency of the scattered light would be significantly higher than the one for the PL light (arbitrarily polarized).

To test that, an experiment was carried out with the setup shown in Fig. 3.11. A pair of New Focus 5525 Glan-Thompson calcite polarizers were used in the experiment with a nominal extinction ratio of 100000 : 1. One was placed at the location A to adjust the polarization of the incident laser light, defined as the polarizer. The other one was placed right above the collimating objective, used as an analyzer. T

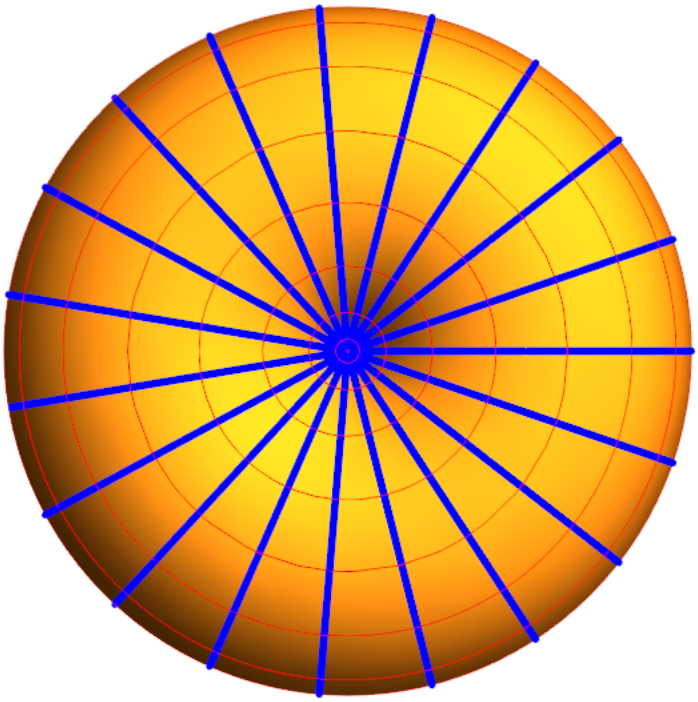

(a)

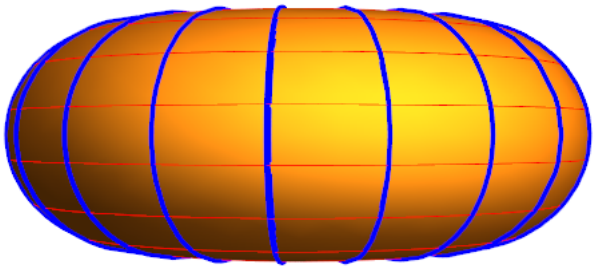

(b)

Figure 3.13. Intensity distribution of the scattered light in solid angle. The QD is located at the geometry center, while the blue mesh indicates the polarization direction of the scattered light. Polarization of the scattered light (blue mesh) viewed by the collimating objective: (a) With P polarized incident light. (b). With T polarized incident light. Intensity of the scattered light is indicated by the radius of the shape.

polarization is defined as the zero degree for the polarizer, and the direction along the laser beam was defined as the zero degree for the analyzer. Laser light with energy 3.05 eV was used as the incident light because the spectrum of the scattered light is well isolated from the PL spectrum. The experimental data are shown in Fig. 3.14, where the intensity of the scattered light yields a sine square curve with respect to the analyzer's angle when the polarizer is at 0° (the incident light is T polarized). A sine square curve with smaller amplitude was observed when the angle of the polarizer was at 40°. When the light is P polarized, no explicit dependence on the analyzer was found (results show a constant with noise). Accordingly, the idea was proved by the experimental results and an extinction ratio of 127 : 1 was achieved when the analyzer is set at 0°.

By integrating the polarizers into the off-axis collecting system, the complete setup for SBE PL spectroscopy was built. During the experiment, the laser was first sent through a polarizer to generate T (into the paper in Fig. 3.11) polarized light. Then, a lens with a focal length of 0.8 cm focused the polarized light onto the sample (a capillary filled with QDs suspension. The capillary has a reported wall thickness of 0.15 mm with an inner diameter of 1 mm). The emitted PL light was collected and collimated by the collimating objective (with a numerical aperture of 0.5) perpendicularly to the laser path. Right above the collimating objective an analyzer was placed (polarization plane parallel to the laser beam, part E in Fig. 3.11). Then, the PL light was sent through a coupling objective, which has the same f-number as the spectrometer does, into the entrance slit of the spectrometer. To align the system, the laser with an energy of 3.05 eV was always introduced first to help find the focal point of the excitation beam. A typical experimental PL result is shown in Fig. 3.15, with the laser signal substantially suppressed and negligible compared to the PL signal. Most importantly, significant UCPL, which is much stronger than the DCPL was observed.

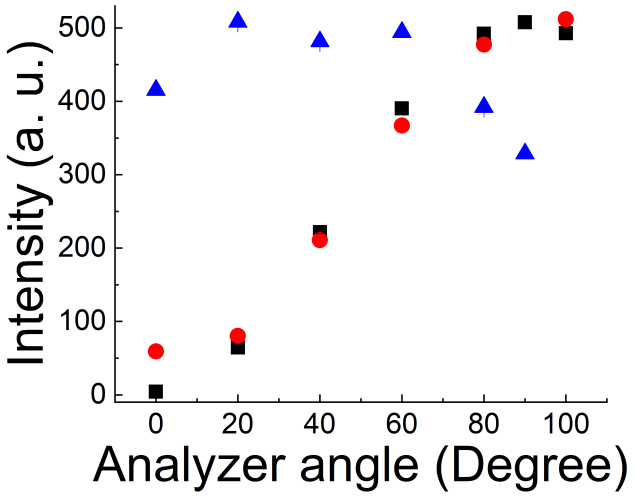

Figure 3.14. Variation of the scattered intensity versus the angle of analyzer when the polarizer is at 0° (black squares), 40° (red dots) and 90° (blue triangles). Laser with energy 3.05 eV was used in the experiment.

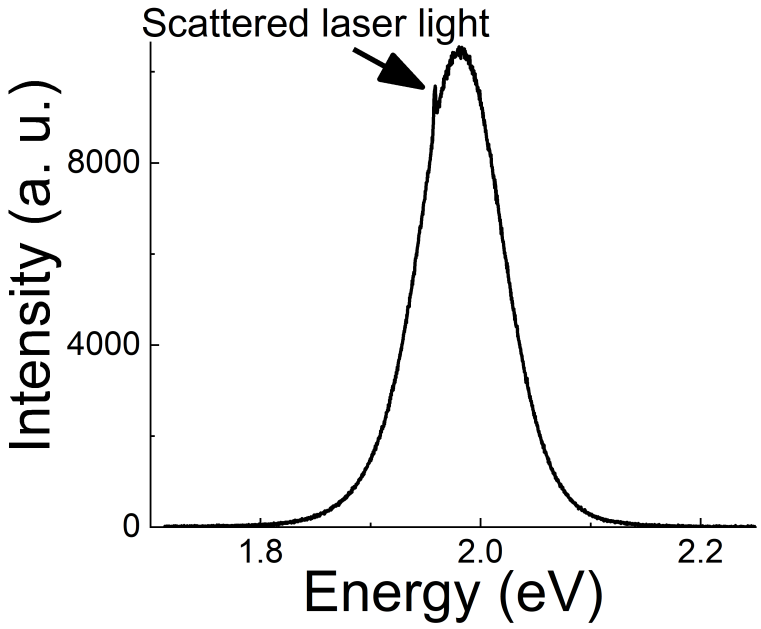

Figure 3.15. Photoluminescence spectra of the sample from batch 2 with $\varepsilon_{ex} = 1.956$ eV.

3.6.2 Specifics of the PL spectrometer [100]

The resolution of the spectrometer directly defines the precision of our measurement. To achieve sub-meV resolution, a custom designed PL spectrometer was used.

The spectrometer was assembled with a Horiba Jobin Yvon Triax 550 monochromator (effective focal length is 550 mm) and a Horiba SpectrumOne CCD 3000 imaging system. As shown in Fig. 3.16, the collected PL light was first pre-focused with an objective which matches the focal number (6.4) of the monochromator, then sent through the entrance slit. Inside the monochromator, the light was collimated by a concave mirror (M1) and sent onto the grating (G2 in the scheme) to transfer its energy distribution into spacial distribution along the horizontal direction. A low resolution grating (G1), and a high resolution grating (G2) with groove densities of 300 and 1200 grooves/mm respectively, were mounted on the rotary turret driven by a high precision stepper motor, providing tunable spectral resolution and range. The light was focused onto a 2000×800 (width$\times$height) CCD array. With this spectrometer, a waveledngth resolution of ~ 0.16 nm (~ 0.05 nm) with a band width of ~ 180 nm (~ 45 nm) was achieved by using G1 (G2). In working conditions, the CCD array is cooled with liquid nitrogen to 150 K to achieve a dark current noise < 3 electrons per hour per pixel and a readout noise around 4 to 10 electrons per pixel. The entrance slit, rotary turret and the array are controlled by the CCD 3000 controller, while the whole system is remotely controlled by a computer through a GPIB card.

3.6.3 Temperature dependent photoluminescence spectroscopy (optical thermometry)

Temperature dependent PL spectroscopy was used to detect the changes in the PL signal of the QDs sample at different temperatures, providing calibration for the optical thermometry.

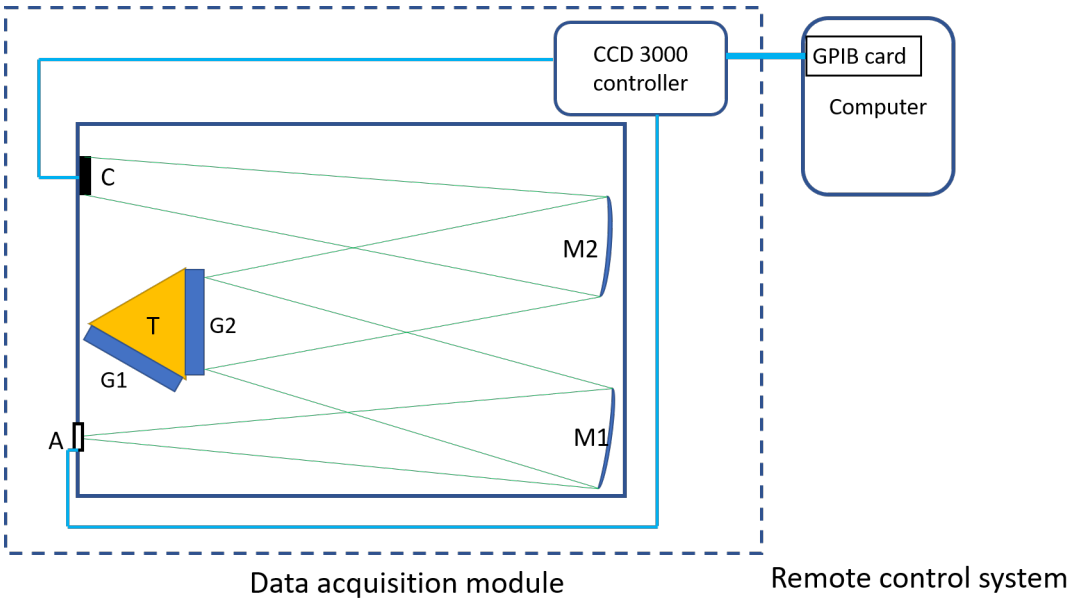

Figure 3.16. Schematic top view of the inside of the monochromator. A: entrance slit, C: CCD chip, M1 and M2: concave mirrors, G1: low resolution grating mirror, G2: high resolution grating mirror, T: rotary turret.

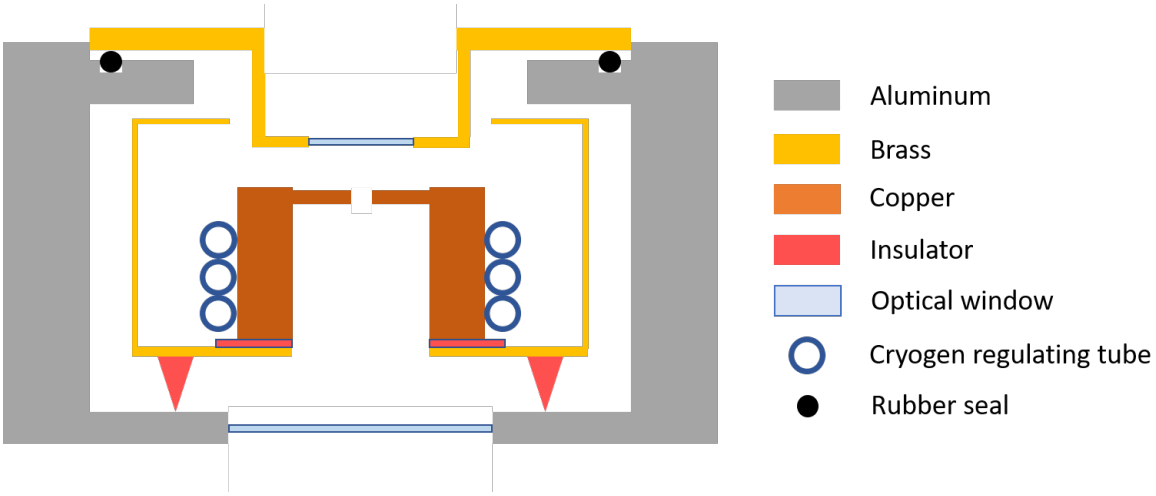

Figure 3.17. Schematic of the vertical cross-section of the cryostat.

A Janis Supertran, which includes a ST-500 Microscopy Cryostat System was used to control the temperature of the QDs samples. The schematic plot of the vertical cross-section of the cryostat is shown in Fig. 3.17. The sample holder is a copper disc machined with a center hole, connecting to a copper cold finger. Cryogen was regulated in the copper tube surrounding the cold finger to provide cooling power, meanwhile a heater with maximum heating power of 5 W was mounted onto the cold finger to provide heating power. The heater with a negative slope thermal resistor attached onto the cold finger were controlled by a Lakeshore 331S temperature controller to regulate the temperature of the system, while the controller itself was remotely controlled through a GPIB connection by using Labview on a computer. Since the absolute temperature of the system was not critical in our measurement, the manufacturer's calibration of the temperature sensor was used. The temperature data of the system was recorded at a rate of 20 samples per second and stored in the computer. According to our application, where the targeting temperature range was from 100 K to 300 K, liquid nitrogen was used as the cryogen of the system. The cryostat was evacuated to a pressure around 5×10^{-6} mbar to avoid condensation and to thermally decouple the sample from the environment.

First, a preliminary experiment was carried out with QDs samples bought from NNlab to characterize the samples' general temperature dependent PL properties within a wide range of temperature (from 200 K to 300 K). The experiment could not be carried out while keeping the QDs in the suspension, because the melting points of the organic solvents forming the suspension are typically around the freezing point of water (OAM and ODE are even higher around 290 K). Hence, samples were pre-deposited onto a glass cover-slip, using a similar process as for XRD. A droplet of the sample was deposited onto the cover-slip, and air-dried, the process was repeated until a visible QDs layer appeared. A thin layer of vacuum grease was applied to the copper disc before placing the cover-slip onto it to increase thermal conductivity, minimizing the temperature difference between the cold finger and the tested sample. The QD layer was placed right above the center hole of the copper

disc sample holder. It is well known that the energy gap of semiconductors are a function of temperature, which decreases monotonically as the temperature increases. The property was also observed in semiconducting QDs [85, 102, 103]. Therefore, the temperature dependence of the QDs' PL emission energy was investigated. During the test, the target temperature was remotely set from the Labview, and the real-time temperature of the cold finger was monitored and recorded simultaneously. After turning on the temperature control, a 20 min delay was granted to allow the system to reach thermal equilibrium. An argon laser ($\varepsilon_{\text{ex}} = 2.41$ eV) was used as the excitation source with its power attenuated to $50\,\mu$W. In fact, the PL processes as excited by the argon laser, is dominated by DCPL, introducing the heating effect from phonon emission processes [63, 77, 104]. Due to the good thermal contact provided by the grease layer, the temperature change was negligible. The experiment was carried out with two trials, first the sample's temperature was increased from 200 K to 300 K with a step size of 10 K, second, the temperature was decreased from 300 back to 200 K with the same step size. At each temperature, five PL spectra were collected with a typical 10 s gap between them. The results are shown in Fig. 3.18(a), where the sample's emission energy decreased as the temperature increased, also the cooling and heating trials agreed with each other. Hence, our setup was able to detect the change in QD's PL spectra with varying temperature. $\bar{\varepsilon}_{\text{em}}$ and σ showed a monotonic dependence on temperature, while a better sensitivity was observed in $\bar{\varepsilon}_{\text{em}}$. The measurement precision increases with a higher intensity of the probe beam and is inversely proportional to the square root of the number of measurements. In another word, the more energy introduced by the probe beam, the better the measurement precision would be. Ideally, any desired precision can be achieved. However, the PL processes excited by the probe beam are energy down-conversion processes, creating a net heating effect. Therefore, the smallest measurable temperature change in the sample is the competition result between the precision improvement and the extra heating power introduced by the increased energy of the probe beam being used. This is important to us as the temperature change in the sample is expected to be small.

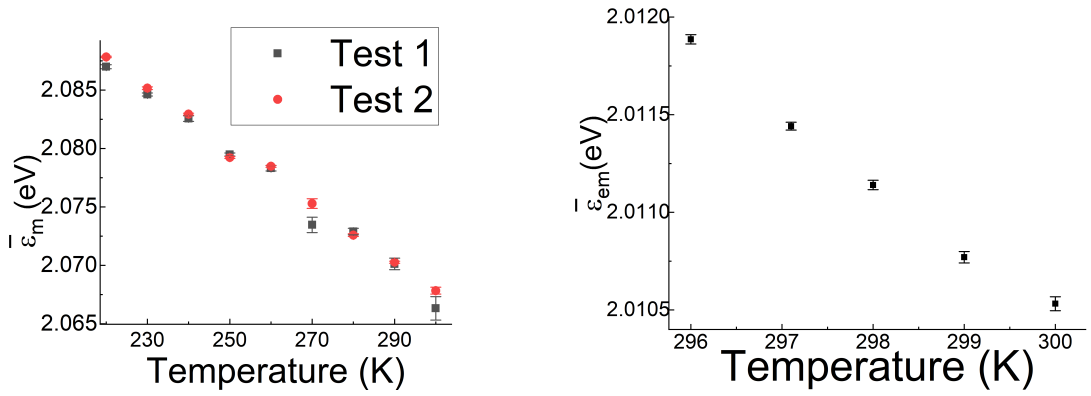

(a) (b)

Figure 3.18. QD sample's meam emission energy versus temperature. (a) preliminary test with CdSe QDs sample purchased from NNlab (b) Calibration data within the temperature range of the OR experiment (around room temperature), where a proportionality of $-360\,\mu$eV/K was found with a typical uncertainty of $\pm 35\,\mu$eV. The sample used in the measurement was from batch 2.

A test was carried out in our system to determine the optimal input power of the probe beam and the details will be discussed in chapter 4.

It was reported that the optical properties of QDs, especially the QY usually degrades significantly after removing them from the suspension [1]. The sample was washed with acetone followed by precipitation, then re-suspended into hexane. The phenomenon was also found in our sample. As shown in Fig. 3.19, a noticeable decrease in the PL intensity was observed after moving them out of the original solvent. Also $\bar{\varepsilon}_{\mathrm{rm}}$ changes, σ_{s} changes, etc. Thus, in the OR experiment the samples were directly prepared with the synthesis suspension (in which the best QY were reported [2]). Consequently, calibration of the optical thermometer was carried out by using a sample prepared with the same method and in the same conditions for OR experiment (which will be described in the section 3.7.1). The capillary was attached to the copper disc with the help of a layer of vacuum grease and the portion containing the QD samples was placed right above the center hole. The temperature of the cold

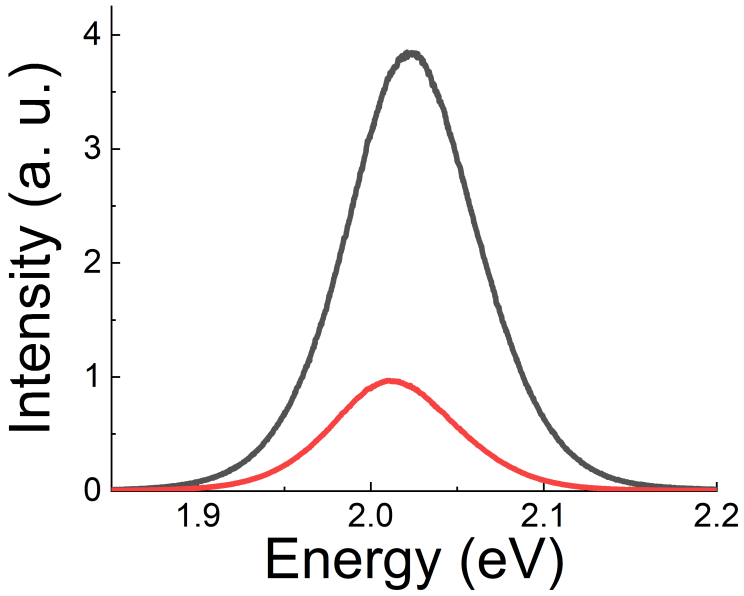

Figure 3.19. Photoluminescence spectra of the QD sample before (black) and after (red) washing process. The plot was obtained using the sample from batch 2.

finger was monitored and controlled with the temperature controller. For a given temperature, 30 min was granted to allow the system to reach thermal equilibrium. Then 10 PL spectra with $\varepsilon_{\text{ex}} = 2.41$ eV (Ar laser) and a power of $50\,\mu$W were taken. Data are shown in Fig 3.18(b). The mean emission energy of the sample was slightly lower than the value shown in table 3.4 (excited with $\varepsilon_{\text{ex}} = 3.05$ eV) due to the lower excitation energy of the Ar laser. Small deviation (± 5 meV) in the mean emission energy was also found in different samples withdrawn from the same batch, which might come from the sample inhomogeneity. Since the experiment relies on measuring energy difference, the vaiation was not important.

Here the mean emission energy was calculated with Eq. 2.49 and the standard error of the mean was used as the error bars. As shown in Fig. 3.18(b), a typical proportionality factor of $-348.0 \pm 16.4\,\mu$eV/K was found for our sample, which confirms Wang *et al.*'s report [85].

3.7 Experiment of optical refrigeration

The experimental setup to realize optical refrigeration is described in this section, including the data acquisition system.

3.7.1 Sample preparation

Capillaries pre-cut to 25 mm long (originally 10 cm long) were used as the sample container. Their wall thickness and inner diameter are identical to the ones used for the temperature dependent PL test. A small amount ($\sim 4\,\mu$l) of sample was transferred to the center of the capillary (the length of the sample section is about 3 mm long), under inert gas protection. Then the capillary was sealed with superglue on both ends to make it compatible with the vacuum environment.

3.7.2 Thermal isolation system

To make the cooling effect at SBE observable, the OR experiment was carried out inside the cryostat with a pressure of $\sim 7.4 \times 10^{-6}$ mbar and a thermal radiation shield (a brass shell inside the cryostat covering the sample zone).

As shown in Fig. 3.20, the copper disc with center hole was replaced by a new disc made of anodized aluminum. Between the disc and the cold finger, thermal conductive grease was applied to create a uniform ambient temperature around the sample and fix the disc. The aluminum disc has an opening on the bottom close to the edge to allow the laser light to pass through. To prevent the pump laser beam from directly shooting into the collection system, the laser light was send through the opening and turned 90 degrees by a flat aluminum coated plate (working as a reflective mirror). To reduce the thermal conductivity through the sample holder, the capillary was supported by 2mm×3mm×4mm (width×length×height) pieces of polystyrene at both ends.

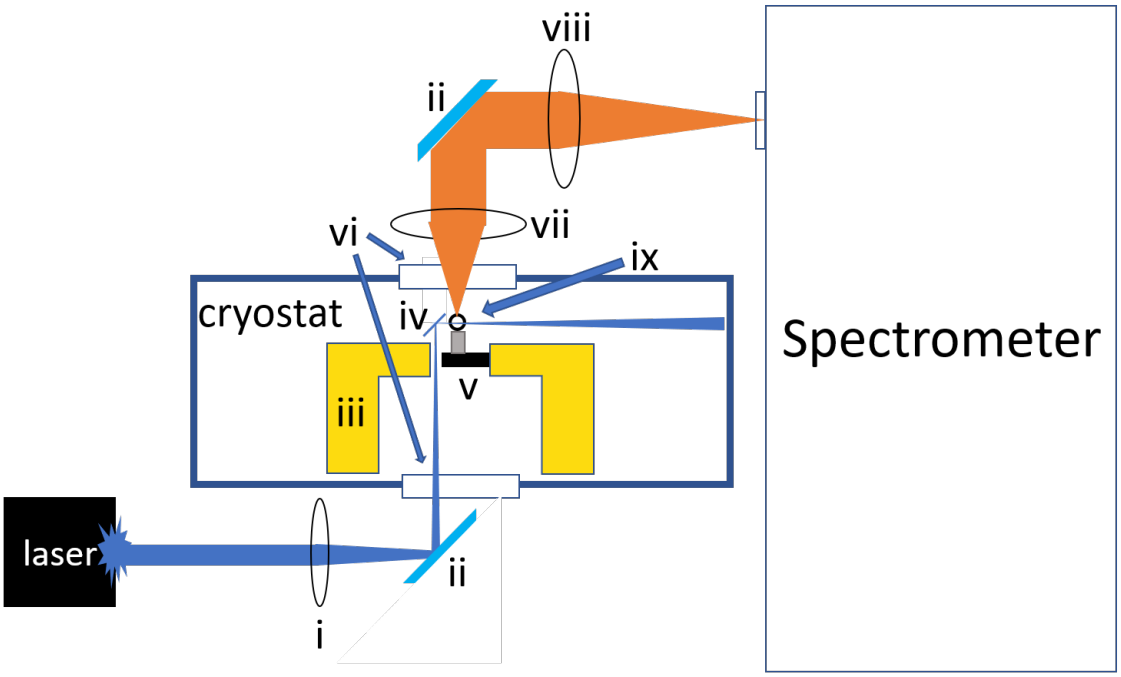

Figure 3.20. Schematic plot of the OR experiment's collection system. i, focusing lens; ii, high reflective mirrors; iii, copper cold finger; iv, polished aluminum coated plate; v, sample substrate including an anodized aluminum plate and a thermal insulting support made of expanded polystyrene; vi, optical windows; vii, collimating objective; viii, adapting objective; ix, capillary loaded with QDs sample.

3.7.3 Alignment of the cooling pump laser with the optical thermometry

The schematic plot of the pumping and monitoring (optical thermometry) system is shown in figure 3.21 (pictures of the real equipment are shown in Fig. 3.22(a) and 3.22(b)).

According to the calculation result (section 2.5), a diode laser with typical emission energy of 1.945 eV or a HeNe laser were used as the cooling pump. The optical thermometry was applied by sending a much weaker Ar laser beam as a probe (typically, $7\,\mu$W) colinear with the major pump beam by using a beam splitter. A pair of high reflective mirrors were used to guide the probe beam into the beam splitter, providing adjustment in both the beam location and direction. After placing the

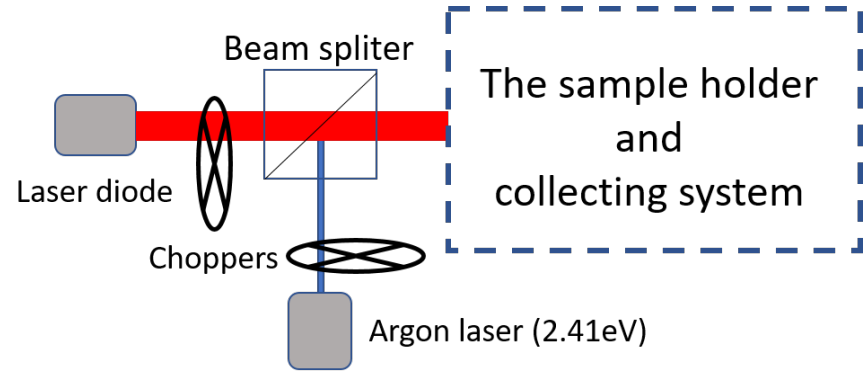

(a)

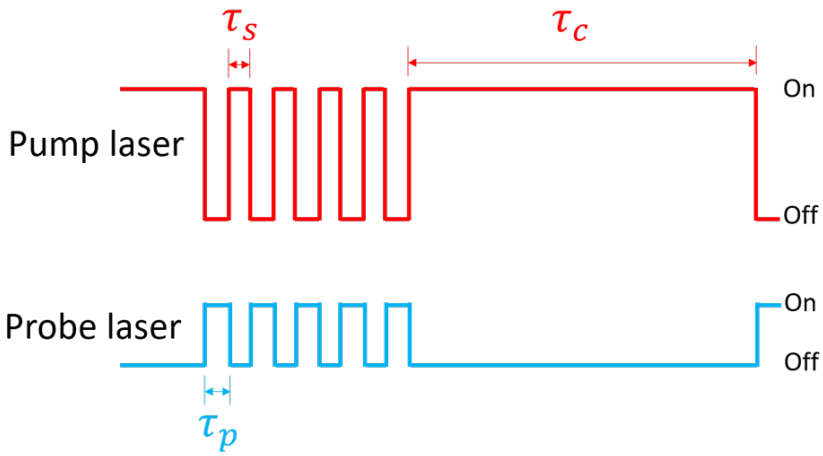

(b)

Figure 3.21. Schematic of the cooling and monitoring system: (a) Orientation of the pump beam (diode laser), the probe beam (argon laser) and controlling chopper, (b) programmed time sequence for alternating the excitation sources between the pump laser and the probe laser, where each measurement contains five consecutive pules of probing laser with length τ_p and gap τ_s between two consecutive probings. τ_c is the length between two measurement, during which the cooling pump was on.

sample onto the sample holder, both lasers were sent into the system before vacuuming the system. The beams were aligned by eye. Afterwards both laser beams were blocked and the system was pumped down. After the system's pressure reached the base value (7.4×10^{-6} mbar), the pump beam (attenuated to 100 μW) was sent into

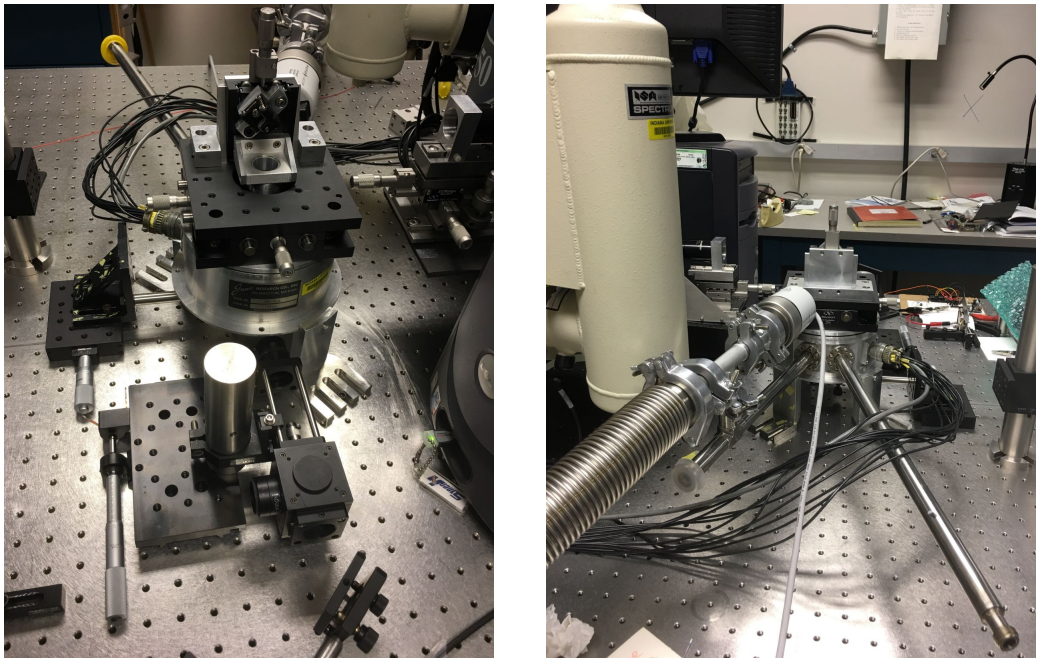

(a) (b)

Figure 3.22. Pictures of the collection system, (a) light entrance of the cryostat (b) vacuum and cryogen transfer line of the cryostat.

the system again while the probe beam remained blocked. By using the polarization technique described in section 3.6.1, the collecting system (collimating objective) was aligned first by maximizing the PL signal. Then, the pump beam was blocked, the polarizers was removed and the probe beam was sent into the system. By adjusting the guiding mirrors, the probe laser was further aligned by finding the maximum PL intensity.

3.7.4 Time sequenced optical thermometry

A computer programmed chopper was used to alternate the excitation source between the pump beam and the probe beam. During a complete OR experiment, the temperature of the sample was monitored every τ_c seconds (typically, 30 s, 60 s or 120 s). For each temperature measurement, five consecutive optical thermometry

pulses were applied with the same exposure duration $\tau_p = 0.3$ s and $\tau_s = 3.1$ s (remove the gap between two consecutive pulses, limited by the data acquisition time of the spectroscopy system) to provide five data points. The entrance slit of the spectrometer was triggered by the same computer program used for the chopper, such that it only collected spectra while the probe laser was on. At the beginning of the OR experiment, one or more temperature measurement were obtained while blocking the pump beam to obtain the system's base temperature. The pump laser was unblocked right after the end of the final base temperature measurement, initiating the OR process. The length of the experiment was preset into the computer program by defining τ_c and the number of repetitions, while the OR process was terminated by blocking the pump laser beam. The data were collected by the CCD controller and transferred to the computer through the GPIB connection. Results from the OR experiments will be presented and discussed in the next chapter.

4. RESULTS AND DISCUSSION

4.1 Precision of the optical thermometry

As mentioned in section 3.6.3, the optical thermometry's precision is improved as the input energy of the probe light (Ar laser) increases. However, the heating effect generated from the DCPL processes introduced by the probe beam would mask the OR process, leading to a difficulty in observing cooling. An important reason to use an Ar laser instead of the diode laser with 3.05 eV emission energy, is to reduce heating. Therefore, the first experiment carried out with the OR setup was optimizing the optical thermometry.

The solution was to introduce multiple probings with low total energy input (short duration and low input power). Therefore, the heating effect of each probing was not significant. Furthermore, in between the gap of two consecutive probing, the pump laser can be introduced to reduce the overall effect of the heating processes. However, limited by the spectrometer acquisition time, the shortest gap between two exposures was around 3.3 s, five PL spectra would take over 15 s, therefore, to give a statistically meaningful analysis without a significant data acquisition time, the number of PL spectra taken for each measurement was limited to 5. According to section 3.6.3, to be able to distinguish a temperature difference of 0.1 K, a typical resolution better than 35 μeV was required. With an input power of 5 μW, the required resolution can be achieved by setting the probe duration to 0.3 s. As shown in Fig. 4.1, an average resolution of $\pm 15\,\mu$eV was achieved, where the standar error of the mean is used. The fluctuation of the mean emission energy between measurements was attributed to the temperature change of the environment, and not a reflection of the change of the T_{QDs} due to the thermometry processes. A time gap $\tau_{\mathrm{c}} = 120$ s between two measurements was used in the test. To increase the time resolution of the optical thermometry,

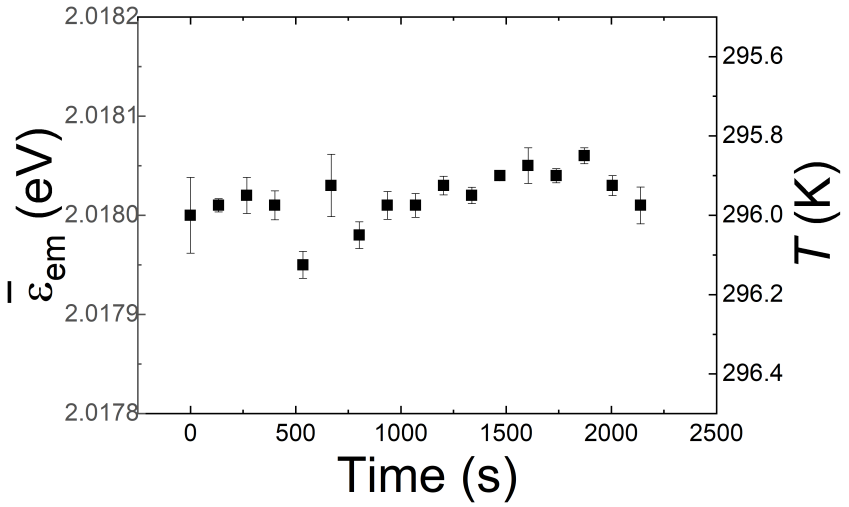

Figure 4.1. QDs' mean emission energy measurement result. Each data point is the mean value derived from five photoluminescence spectra taken consecutively (3.3 s gap), with a duration of 0.3 s for excitation and a input power of 5 μW. The temperature was obtained according to the sample's own calibration data. The sample was from batch 2.

shorter τ_c was used in the OR experiment and as a consequence, the effective heating power was increased. Since a complete OR measurement cycle includes five probings (five τ_ps and four τ_ss) and a pumping stage (τ_c), the mean heating power $\bar{P}_{h,o}$ can be calculated by

$$\bar{P}_{h,o} = \alpha(\varepsilon_{ex}) P_{ex} \frac{5\tau_p}{5\tau_p + 4\tau_s + \tau_c} (1 - \frac{\bar{\varepsilon}_{em}}{\varepsilon_{ex}}). \tag{4.1}$$

Here, $P_{ex} = 5\,\mu$W, $\varepsilon_{ex} = 2.41$ eV, $\bar{\varepsilon}_{em} = 2.023$ eV (for sample from batch 2) and $\bar{P}_{h,o} \approx 48.0$ nW was derived with $\tau_c = 10$ s.

As shown in Fig. 4.2, a limited heating effect of $-29.6 \pm 27.4\,\mu$eV was observed when the time gap was set to be 10 s. The situation was improved when increasing the step to 30 s, the net energy down-conversion suggested by the data was $-16.9 \pm 25.2\,\mu$eV. In both cases, the heating effect was indistinguishable from the environmental temperature fluctuation. Therefore, with the optical thermometry temporal gap (τ_c) longer than 10 s per data point (not including the data acquisi-

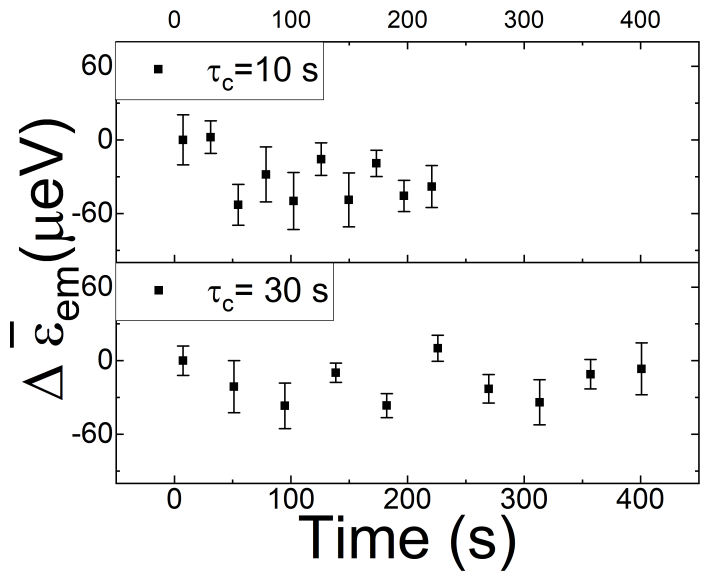

Figure 4.2. Change in QD's mean emission energy measured with optical thermometry with a time gap (τ_c) of 10 s (upper pannel) and 30 s (lower pannel).

tion time), the heating effect was considered to be negligible and no correction was necessary.

4.2 Cooling effect observed in the OR experiment

To achieve a better temporal resolution of the sample's temperature (in terms of the mean emission energy) information, $\tau_c = 10$ s was used. As shown in Fig. 4.3(a), three trials were carried out and their data points were plotted in three different colors (black, red and blue). All of them were performed with the same sample, with a 30 min relaxation time between each trial to allow the sample to relax to its original temperature. Therefore, each trial was considered to be independent to the others, and the effectiveness of the relaxation procedure was confirmed by the observation that the starting mean emission energy of all three trials did coincide with each other (within the experimental error). During the experiment, the pump laser $\varepsilon_{ex} = 1.943$ eV was introduced right after the first optical thermometry with a

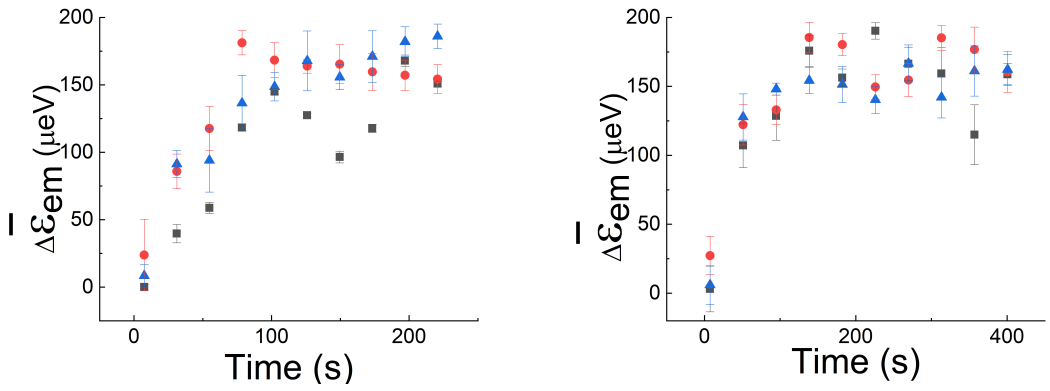

(a) (b)

Figure 4.3. Change of sample's $\bar{\varepsilon}_{em}$ during the OR experiment with (a) $\tau_c = 10$ s, (b) $\tau_c = 30$ s. The experiment was carried out with $\varepsilon_{ex} = 1.943$ eV (1.5 mW), $\tau_p = 0.3$ s and $\tau_s = 3.4$ s. The sample is from batch 2. Standard error of the mean was used for the error bar. Different colors denote different trials of the experiment.

power of 1.5 mW. A noticeable increase in the sample's mean emission energy was observed with a typical value, $\Delta\bar{\varepsilon}_{em} = 154.7 \pm 6.7\,\mu$eV (determined by averaging the data points after 150 s, standard error of the mean was used for the error bar). When calculating $\Delta\bar{\varepsilon}_{em}$, the initial value of the first trial was assigned as the reference. All trials trended to stabilize around the value of 155 μeV, suggesting good repeatability of the experiment. To confirm the thermal equilibrium was established during the OR process, experiments with longer τ_c value were carried out with the same sample. Being identical to the experiment with $\tau_c = 10$ s, three trials with 30 min gap between each of them were performed. As shown in Fig. 4.3(b), with $\tau_c = 30$ s, a similar sample mean emission energy growth pattern was observed, and the saturation was confirmed. Meanwhile, an increase of $\Delta\bar{\varepsilon}_{em} = 158.4 \pm 4.4\,\mu$eV (determined by averaging the data points after 150 s, where the standard error of the mean was used as the error) was found in the mean emission energy, which showed excellent agreement to the ones with $\tau_c = 10$ s. According to the calibration data of the optical thermometry, a temperature change of -0.45 ± 0.02 K was observed. As the results among different trials were

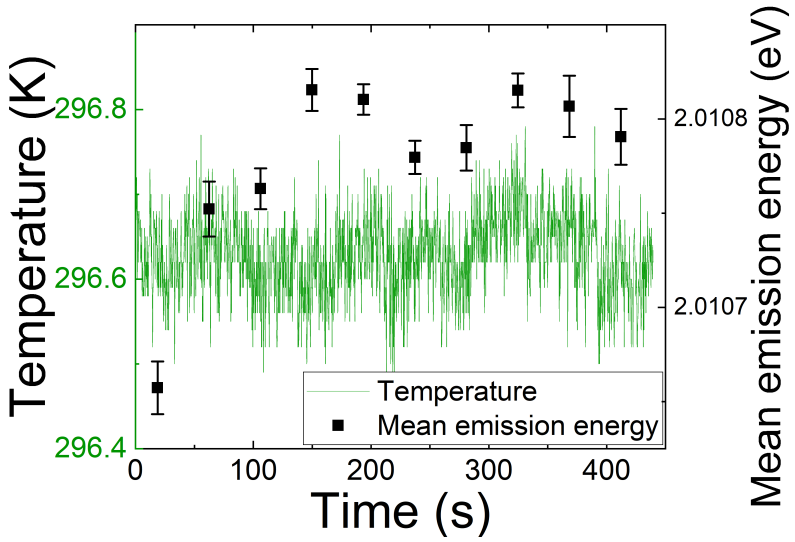

Figure 4.4. Temperature of the environment (cryostat, measured from the thermister attached to the cold finger) during a typical experiment ($\tau_c = 30$ s).

very consistent, the possibility of the observed temperature change originating from the environment was precluded. Another direct evidence came from the temperature of the cold finger. The sample is covered by the brass shield, and all parts inside the shield (except for the sample) were thermally well connected to the cold finger, the environment temperature was treated to be identical to the one of the cold finger. Shown in Fig. 4.4 is a typical plot of the environment temperature during a trial ($\tau_c = 30$ s) of the experiment. A mean value of 296.63 K with a standard deviation of 0.05 K was found, while no observable correlation to the sample's mean emission energy was found. Therefore, the increase in the mean emission energy was generated by the OR cooling processes and the fluctuation of the environmental temperature was introduced as an error source. By combining all the data above, a complete plot describing the sample's temperature change under OR procedure are shown in Fig. 4.5, where the starting value was averaged over the trials from both $\tau_c = 10$ s and $\tau_c = 30$ s experiments. Accordingly, a cooling effect of -0.42 ± 0.05 K was observed in our sample.

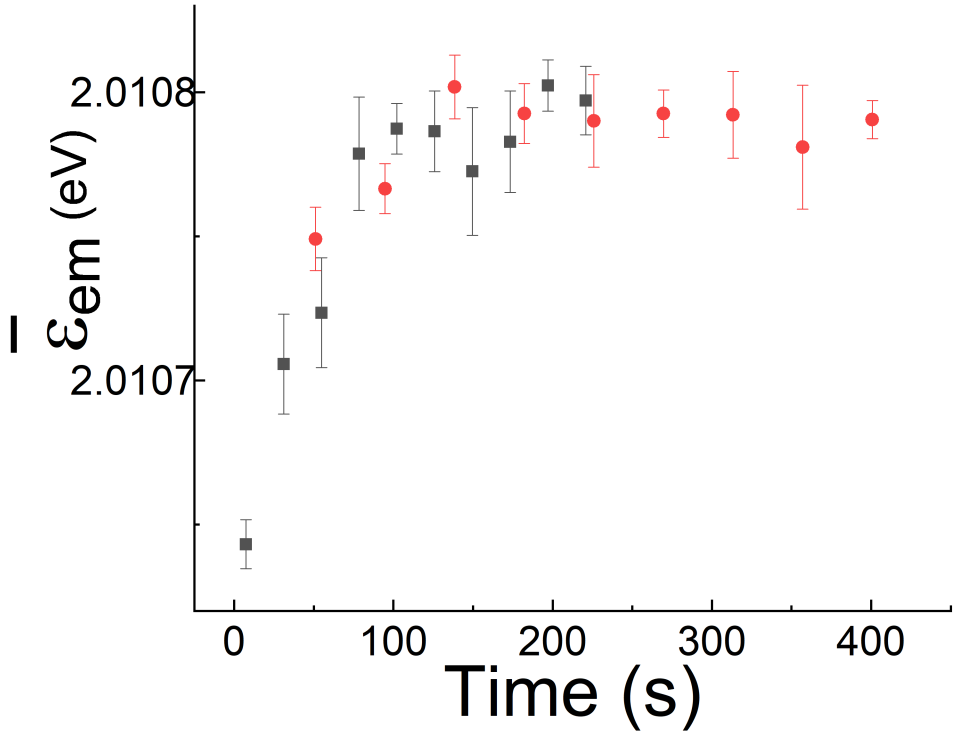

Figure 4.5. Mean emission energy change produced by OR from experiments with $\tau_c = 10$ s (black squares) and $\tau_c = 30$ s (red circles). The first data point was averaged over trials for both $\tau_c = 10$ s and $\tau_c = 30$ s experiments.

OR experiments with different excitation energies were also carried out. Experimental parameters and results are summarized in Table 4.1. The normalized cooling efficiency of the system gradually decreased to zero as ε_{ex} decreased. This is an evidence of the non-zero background absorption from the sample, which is true for all practical systems. As shown in Fig. 4.6, since the temperature change of the system was small (less than 1 K), the heat power due to the temperature gradient is proportional to the temperature difference between the sample and the environment. Therefore, the relative cooling power of the sample at each excitation energy can be derived with the stabilized $\Delta\bar{\varepsilon}_{em}$ at the thermal equilibrium. By comparing them

Table 4.1.
Experimental parameters and results for different excitation energies.
The experiment was carried out with the sample from batch 2.

$\varepsilon_{\mathrm{ex}}$ (eV)	Excitation power (mW)	$\Delta\bar{\varepsilon}_{\mathrm{em}}$ (μeV)	Temperature change (K)
1.957	1.0	132.7 ± 26.3	-0.38 ± 0.08
1.943	1.5	158.4 ± 4.4	-0.42 ± 0.05
1.941	2.9	236.4 ± 25.7	-0.68 ± 0.07
1.930	3.0	90.0 ± 30.0	-0.26 ± 0.09
1.926	1.9	61.8 ± 24.8	-0.18 ± 0.07
1.918	1.0	-13 ± 27.8	$+0.04 \pm 0.08$

with the calculation results predicted by our model (section 2.5), a QY of 99.8% and a $\alpha_{\mathrm{b}}/\alpha = 700$ ppm was suggested by the experimental data.

4.3 Analysis of the OR experimental result

Thermal equilibrium is established when the heating power introduced by the temperature gradient is identical to the cooling power. As mentioned in section 2.6, analytical calculation of the system's heating power through thermal conduction and radiation processes are not doable. Therefore, simulations using Comsol Multiphysics were used to evaluate the final temperature of an OR experiment at thermal equilibrium. Although the experimental data showed strong evidence of the cooling effect, it was not confirmed by the simulation result, where a 0.1 K temperature change per $10\,\mu$W incident laser power was predicted. A 0.68 K temperature change was observed, which according to our model, yields a net cooling power of $4.6 \pm 0.5\,\mu$W ($\varepsilon_{\mathrm{ex}} = 1.941$ eV with incident laser power 2.9 mW). Possible causes of the difference between the experimental result and the simulation need to be investigated. First, as mentioned in section 2.6, the model does suggest a much larger temperature change when the size of the cooling zone (the laser path inside the sample) is reduced. In

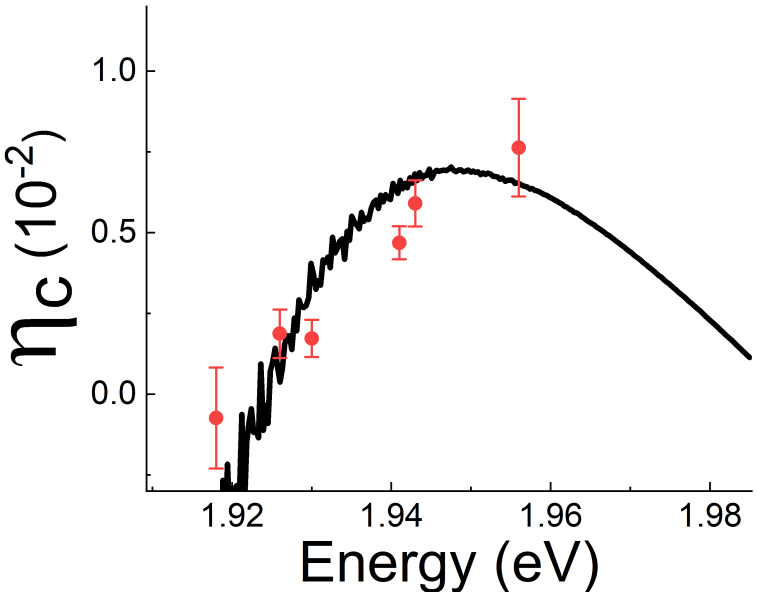

Figure 4.6. Calculated cooling efficiency of the system according to the experimental data (red dots) and the predicted cooling efficiency curve from the semi-empirical model. The model was calculated with $\eta = 99.8\%$ and $\alpha_b/\alpha = 700$ ppm. The experiment was carried out with the sample from batch 2.

the experiment, according to absorption measurements, the absorption efficiency of the system was 33.9% at $\varepsilon_{ex} = 1.941$ eV, therefore the intensity of the light can no longer be considered to be uniform through the path inside the sample. However, the mesh of the program cannot be made fine enough to provide a proper simulation of the system. At the same time, the high absorption efficiency would suggest that the reabsorption could be significant. To test it, the PL spectra at different concentrations (diluted with hexane) were taken. As shown in Fig. 4.7, the sample's PL intensity is linearly dependent on its concentration, suggesting negligible reabsorption (refer to Eq. 1.10), when combined with unity QY, it would lead to a perfect effective quantum efficiency.

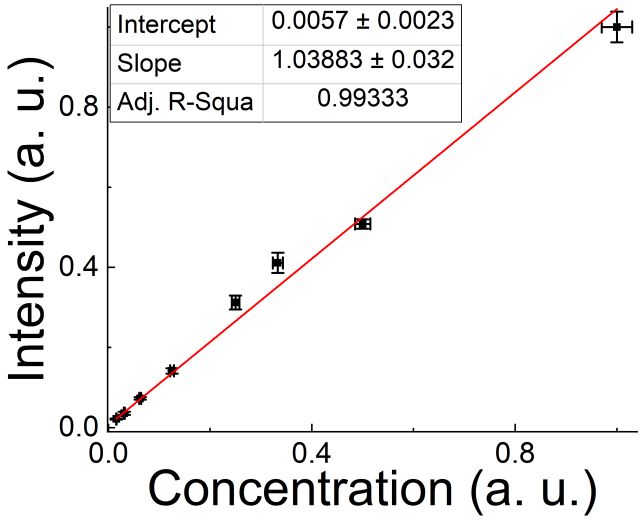

Figure 4.7. PL intensity of the sample at different concentrations. The concentration is normalized with respect to the original (suspension after synthesis) concentration of the sample. The sample is identical to the one used in the OR experiment (from batch 2).

4.3.1 Thermal radiative processes of a quantum dot

Another possibility is that the thermal conduction at the scale of the QDs is very different from the macroscopic situation, where the heat flow through the surface of QDs (surrounded by ligands) is small. A considerable amount of the heat transfer due to the temperature gradient is due to thermal radiation.

Considering the extreme case that the heat transfer between the QDs and the environment is only contributed by thermal radiation. Since the size of QDs is much smaller than the wavelength of the thermal radiation (room temperature), Stefan-Boltzmann law is no longer applicable. According to Chang's paper [105], the radiation absorption power $P_{\mathrm{b}}(T)$ of a nanosphere (blackbody) is given by

$$P_{\mathrm{b}} \approx \frac{75}{\pi^2}\frac{\mathcal{V}}{c^3\hbar^4}\mathrm{Im}(\frac{\epsilon-1}{\epsilon+2})(k_{\mathrm{B}}T)^5. \tag{4.2}$$

Here the permittivity of nano-spheres (QDs) is assumbed to be an energy independent constant, $\epsilon(\varepsilon) \approx \epsilon_{\mathrm{b}}$ through the thermal radiation spectrum. $\mathcal{V}$ denotes the volume of

the sphere and Im denotes the imaginary part of the expression. The imaginary part of bulk CdSe and CdS's relative permittivities, are around 4.1×10^{-7} and 3.7×10^{-6} respectively [106] at infrared. Therefore, $\mathrm{Im}(\epsilon_{\mathrm{b,core}}) = 10^{-6}$ and $\mathrm{Im}(\epsilon_{\mathrm{b,shell}}) = 10^{-5}$ were assigned to the CdSe core and the CdS shell in the calculation respectively as the upper bounds. The thermal radiation power of a QD is just the negative $P_{\mathrm{b}}(T_{\mathrm{q}})$, where T_{q} is the temperature of the QDs. Therefore, heat transfer due to thermal radiation for a QD $P'_{\mathrm{sb}}(T, T_{\mathrm{q}})$ is

$$\begin{aligned} P'_{\mathrm{sb}}(T, T_{\mathrm{q}}) &= P_{\mathrm{b}}(T) - P_{\mathrm{b}}(T_{\mathrm{q}}) \\ &= \frac{75k_{\mathrm{B}}^5}{\pi^2 c^3 \hbar^4} \Big[\mathcal{V}_{\mathrm{core}} \mathrm{Im}\Big(\frac{\epsilon_{\mathrm{b,core}} - 1}{\epsilon_{\mathrm{b,core}} + 1}\Big) + \mathcal{V}_{\mathrm{shell}} \mathrm{Im}\Big(\frac{\epsilon_{\mathrm{b,shell}} - 1}{\epsilon_{\mathrm{b,shell}} + 1}\Big) \Big] (T^5 - T_{\mathrm{q}}^5). \end{aligned}$$

$\mathcal{V}_{\mathrm{core}}$ and $\mathcal{V}_{\mathrm{core}}$ denote the volume of the CdSe core and the CdS shell respectively. In the case of $\varepsilon_{\mathrm{ex}} = 1.941$ eV, where a temperature drop of 0.68 K ($T = 296.6$ K) was achieved, $P'_{\mathrm{sb}} \approx 4.5 \times 10^{-24}$ W. The radius of the QDs used in the calculation was 2.9 nm ($r_{\mathrm{core}} = 1.5$ nm and $r_{\mathrm{shell}} = 2.9$ nm), while the QDs were treated as blackbodies.

On the other hand, the average cooling power of each QD $\bar{P}_{\mathrm{sc}}$ was calculated by

$$\bar{P}_{\mathrm{sc}} = \bar{\alpha}_{\mathrm{p,s}} \times \Delta\bar{\varepsilon}_{\mathrm{u}}, \tag{4.3}$$

where a unit QY was used in the calculation. Here $\bar{\alpha}_{\mathrm{p,s}}$ is the mean photon absorption rate and $\Delta\bar{\varepsilon}_{\mathrm{u}}$ is the mean PL conversion energy. $\bar{\alpha}_{\mathrm{p,s}}$ is defined as

$$\bar{\alpha}_{\mathrm{p,s}} = \alpha_{\mathrm{p}} / N_{\mathrm{QD}}, \tag{4.4}$$

where α_{p} is the sample's total photon absorption rate and is given by

$$\alpha_{\mathrm{p}} = \alpha(\varepsilon_{\mathrm{ex}}) P_{\mathrm{ex}} / \varepsilon_{\mathrm{ex}} = 3.17 \times 10^{15}\,\mathrm{s}^{-1}. \tag{4.5}$$

N_{QD} is the total number of QDs inside the laser path. To calculate it, the volume of the laser path through the sample $\mathcal{V}_{\mathrm{ex}}$ and the sample's concentration $\mathcal{C}_{\mathrm{QD}}$ are required. For the case of our setup, the laser was expanded to a beam size of 1 cm, then focused on to the sample with a focal distance $f = 15.2$ cm. By considering the

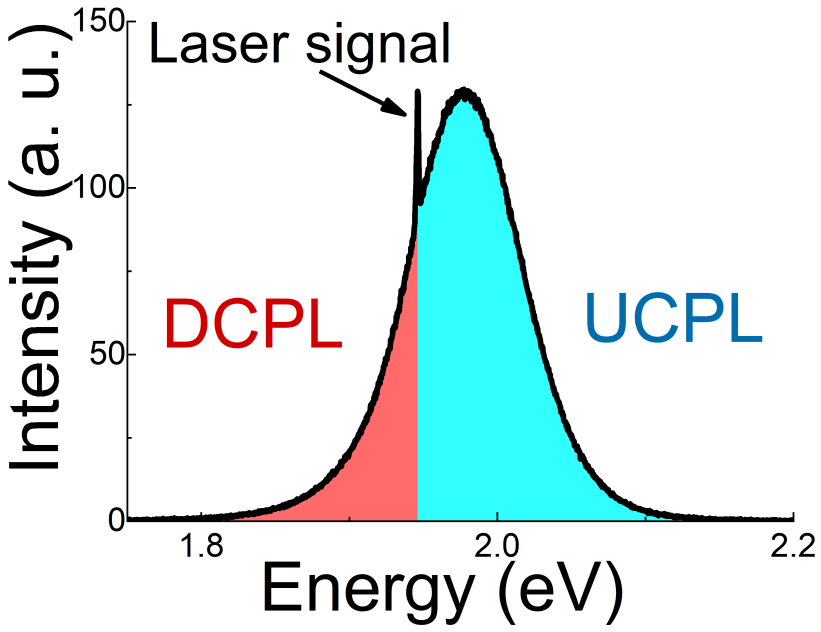

Figure 4.8. UCPL spectrum of CdSe/CdS QDs sample (batch 2) with $\varepsilon_{ex} = 1.945$ eV.

laser had a Gaussian beam profile, the size of the beam waist, $2w_0$ at the focal point is given by

$$2w_0 = \frac{4\lambda}{\pi}\frac{f}{D}. \tag{4.6}$$

Here, D denotes the beam size at the focal length (1 cm), and $\lambda = 632.8$ nm is the wavelength of the laser. According to Eq. 4.6, $w_0 = 6.12\,\mu$m was obtained. The radius of a Gaussian beam w at distance x from the beam waist is given by

$$w(x) = \sqrt{w_0^2\Big[1 + \big(\frac{\lambda x}{\pi w_0}\big)^2\Big]}. \tag{4.7}$$

According to Eq. 4.6 and 4.7, $w(\mathrm{x} = 0.5\,\mathrm{mm}) = 0.037$ mm (assuming the beam's focal point is at the center of the capillary), which is much smaller comparing to the radius of the capillary. Hence, $\mathcal{V}_{ex}$ is approximately

$$\mathcal{V}_{ex} \approx \int_{-0.5\,\mathrm{mm}}^{0.5\,\mathrm{mm}} \pi w(x)^2 dx = 1.18 \times 10^{-10}\,\mathrm{L}.$$

As the volume of the QDs suspension was almost unchanged before and after CdS shell growth, (see section 3.1), $\mathcal{C}_{QD}$ was considered to be identical to the seeds concen-

tration $\mathcal{C}_{\text{seed}} = 1.5 \times 10^{-5}$ mol/L. Therefore, about 1.07×10^{9} QDs were illuminated by the laser. With an incident laser power of 2.9 mW, the mean photon absorption rate of a single QD was $2.96 \times 10^{6}\,\text{s}^{-1}$.

$\Delta\bar{\varepsilon}_{\text{u}}$ was derived from the PL spectra at SBE obtained with the enhanced off-axis collecting system for (technical details see section 3.6.1). The typical spectrum shown in Fig. 4.8, where the UCPL is much more significant than the DCPL processes. According to the data, $\Delta\bar{\varepsilon}_{\text{u}}$ with $\varepsilon_{\text{ex}} = 1.941$ eV was 28 meV. Since the QY of the system in OR experiment was almost unity, we consider all the photons absorbed participated into the OR processes. Thus a net cooling power of 1.33×10^{-14} W was expected for a single QD, which is almost ten orders of magnitude higher than the heat transfer through thermal radiation. As a conclusion, the thermal processes inside the QDs samples are in between the classical heat conduction scenario (adapted by Comsol Mutiphysics simulation) and the pure thermal radiation scenario.

4.3.2 Evaluation of multi-exciton processes

The result from section 4.3.1 can be used to evaluate the possibility of having multi-exciton processes (also known as multiphoton processes), which could lead to heating effects such as Auger processes. As shown in Fig. 4.9, the radiative decay processes of the CdSe/CdS QDs sample yield a single exponential decay curve, with a typical radiative decay lifetime of 24 ns, equivalent to a radiative decay rate of $4.17 \times 10^{7}\,\text{s}^{-1}$, which is more than one order of magnitude faster than α_{s} calculated in section 4.3.1 ($2.96 \times 10^{6}\,\text{s}^{-1}$). Therefore, multi-exciton processes were precluded from our system.

4.3.3 QDs' PL lineshape properties in OR experiment

Besides the change in mean emission energy at high energy excitation, another evidence of cooling effect is come from the PL lineshape at SBE.

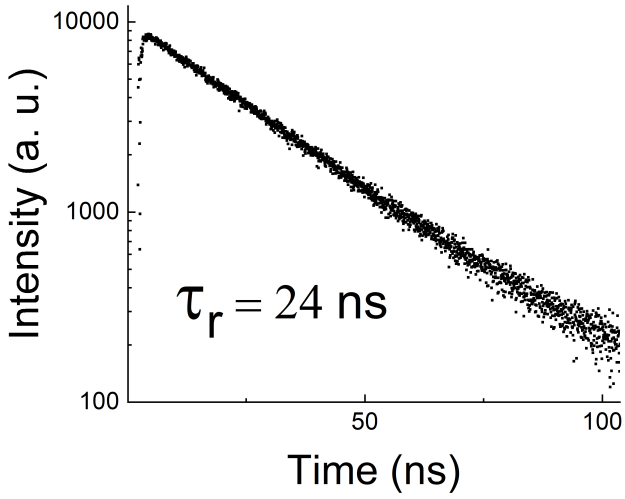

Figure 4.9. Typical radiative decay lifetime data of the CdSe/CdS QDs from batch 2. A radiative decay lifetime, $\tau_r = 24$ ns was observed.

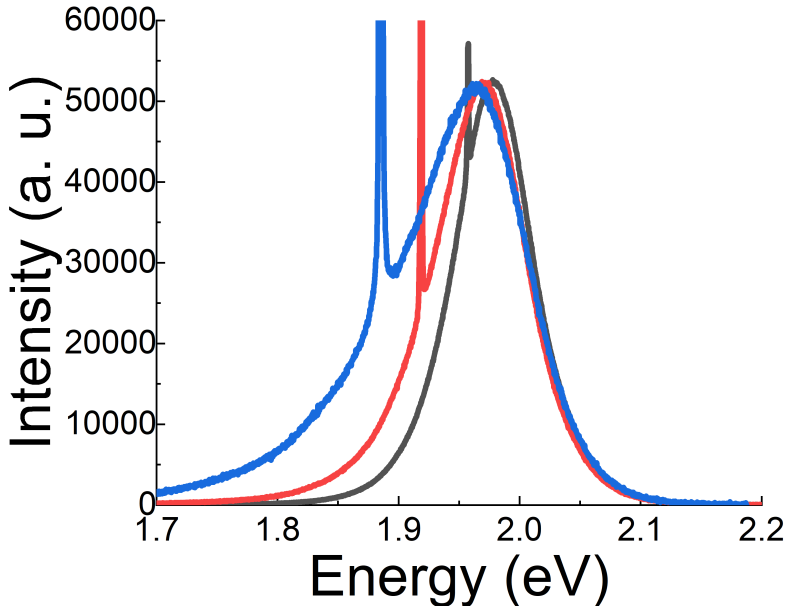

Figure 4.10. QDs sample's PL spectrum obtained with $\varepsilon_{ex} = 1.957$ eV (black), 1.918 eV (red) and 1.884 eV (blue). The sample used was from batch 2.

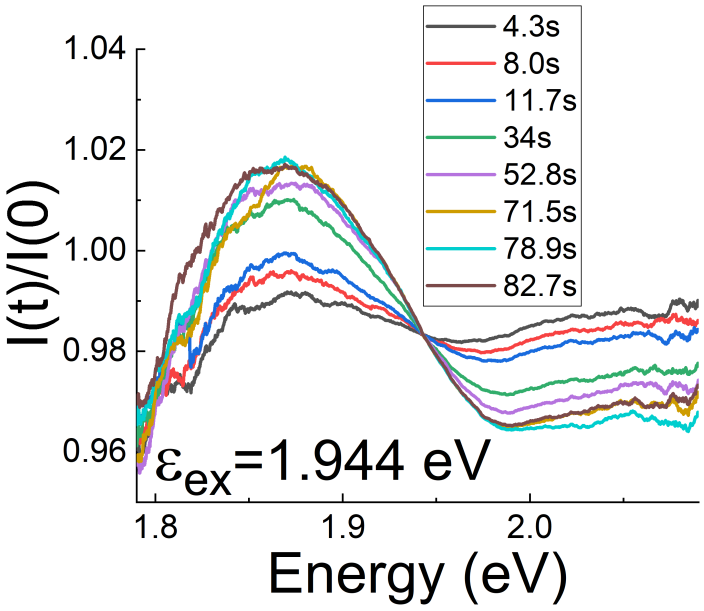

Figure 4.11. Photoluminescence intensity ratio spectra of the QD sample with $\varepsilon_{ex} = 1.944$ eV. The curves are the ratios of photoluminescence intensity after running the OR experiment for 4.3 s (black), 8 s (red), 11.3 s, 34 s, 52.8 s, 71.5 s, 78.9 s and 82.7 s normalized to the first spectrum. The sample used was from batch 2.

The PL spectra of the QD samples at SBE were displayed in section 2.4 to show the validity of our semi-empirical model. According to the data, the DCPL signal become more significant as the excitation energy is decreased further away from the absorption edge. As shown in Fig. 4.10, more asymmetric shape of the sample's (from batch 2) PL spectrum was observed at lower excitation energy, where the DC part decayed much slower than the UC part. The observation is not fully described by the semi-empirical model (still showing good agreement to the UCPL part) as a Gaussian DOS was assigned to the surface states, leading to a rapid decrease of the available excitonic states. At any rate, it can be used to analyze the cooling effect of the OR experiment.

An increase on the energy gap due to a temperature decrease is equivalent to effectively reducing ε_{ex}. Hence, a cooling effect would change QD's PL shape at SBE,

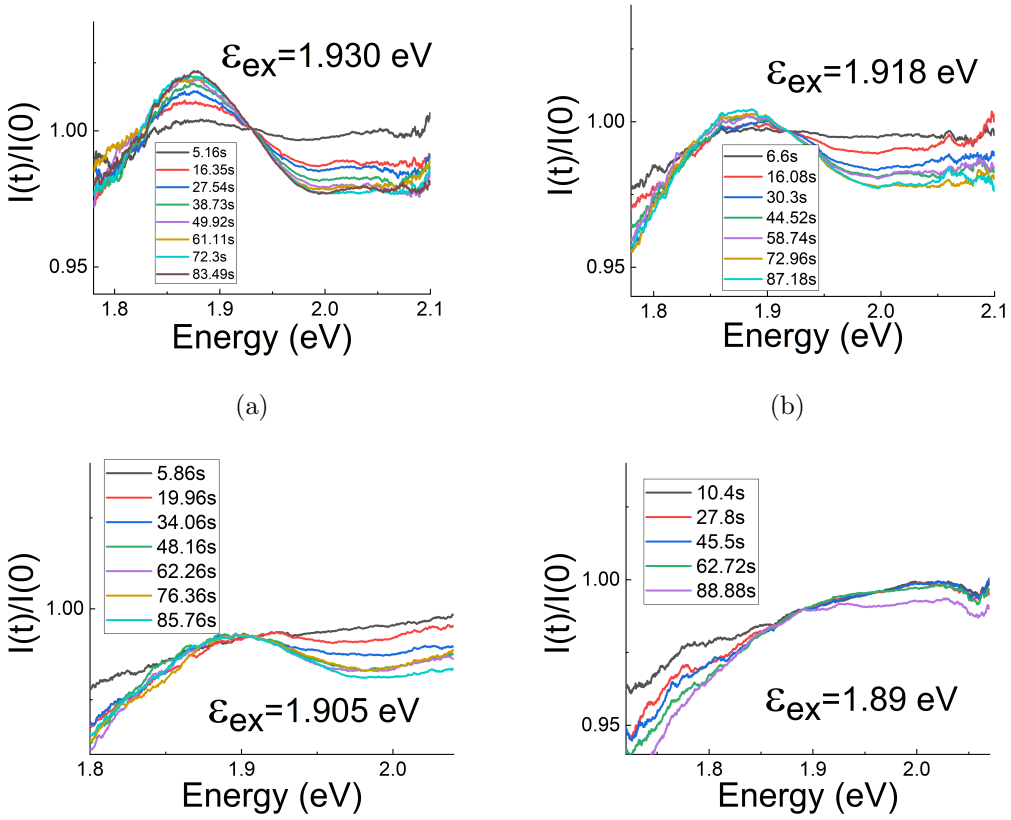

Figure 4.12. Photoluminescence intensity ratio spectra of the sample (a) ε_{ex} = 1.930 eV (b) 1.918 eV (c) 1.905 eV (d) and 1.89 eV for different times where the pump is on. The sample used in the test were from batch 2.

leading to an increase in the relative strength of the DCPL. As shown in Fig. 4.11, an unambiguous growth in the relative strength of the DCPL intensity was observed, while the change saturated around 80 s, confirming the observation derived from the optical thermometry. The values of the ratios between spectra were adjusted in such way that they match at the excitation energy. The noise close to the edge of the spectra is due the low photoluminescence intensity (the electronic noise is constant). As shown in Fig. 4.12, when reducing the excitation energy, the enhancement in the DCPL's relative intensity also decreased and showed a net decrease below $\varepsilon_{ex} <$

1.905 eV. The observation confirmed the OR experimental results where the cooling efficiency reduced to zero around $\varepsilon_{\text{ex}} = 1.905$ eV as the excitation energy decreased.

Meanwhile, from the data a saturation for both SBE and optical thermometry (high energy excitation). Therefore, the change in the sample's PL spectra lineshape also confirms the cooling effect observed by optical thermometry.

4.4 Investigation of the system's relaxation processes after OR experiment.

According to the data, the cooling effect observed in the OR experiments were very limited. Therefore, the heat flow P_{H} is linearly dependent on the temperature difference ΔT,

$$P_{\text{H}} = H\Delta T,$$

where H is the heating coefficient. Hence, the heating rate $\frac{dQ}{dt}$ of the QD sample during an OR experiment is,

$$\frac{dQ}{dt} = H(T_{\text{en}} - T) - P_{\text{c}}. \tag{4.8}$$

Here T_{en} and T denote the temperatures of the environment and the QD sample respectively. By assuming thermal processes of the system following the Ohm's law, Eq. 4.8 becomes

$$C\frac{dT}{dt} = H(T_{\text{en}} - T) - P_{\text{c}}. \tag{4.9}$$

Here C is the effective heat capacitance of the sample. Applying the boundary condition, $T(0) = T_{\text{en}}$, the solution of Eq. 4.9 is

$$T(t) = T_{\text{en}} - \frac{P_{\text{c}}}{H}(1 - e^{-\frac{H}{C}t}). \tag{4.10}$$

According to Eq. 4.10, the temperature change of the sample due to OR processes is expected to follow a single exponential curve with a characteristic time $\tau = \frac{C}{H}$.

The experimental setup to examine the prediction was identical to a regular OR experiment. In order to reveal the relaxation processes of the system, the optical

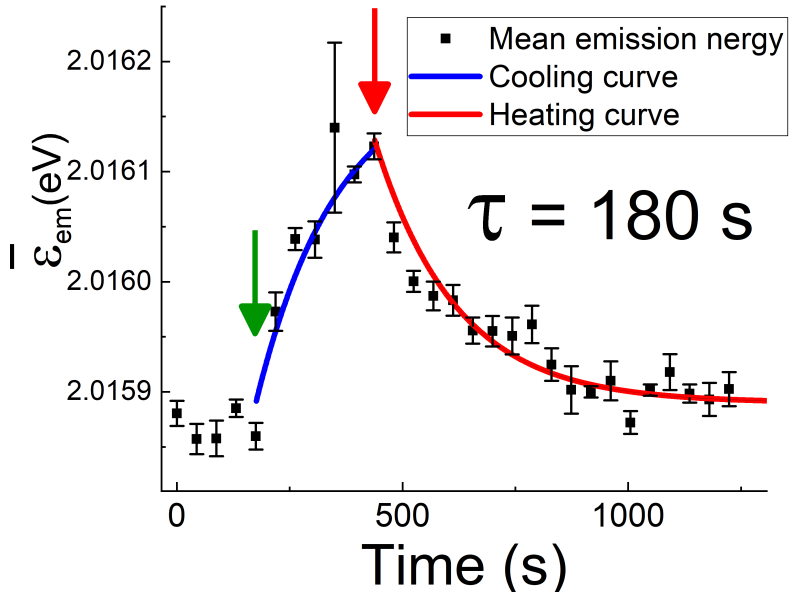

Figure 4.13. Mean emission energy of the sample's PL spectra during the experiment. $\tau_c = 30$ s was used in the experiment, where the pump laser ($\varepsilon_{ex} = 1.941$ eV) was introduced right after the fifth temperature measurement (green arrow) and turned off right after the eleventh measurement (red arrow).

thermometry measurements were collected after the pump laser was blocked. Several optical thermometry measurements were performed before the pump laser being applied to characterize the original state of the system. As shown in Fig. 4.13, the sample's mean emission energy increased right after introducing the pump laser (right after the fifth temperature measurement, green arrow. After the pump laser was removed (right after eleventh temperature measurement, red arrow), the sample's mean emission energy gradually recovered to the base value following a similar pattern. Both the $\bar{\varepsilon}_{em}$ increasing and decreasing processes can be described by exponential curves with a characteristic time $\tau = 180$ s. Another trial was carried out with longer OR procedure and the result is shown in Fig. 4.14. A similar pattern of the sample's mean emission energy was found as the pump laser was introduced (right after the forth temperature measurement, green arrow) and removed (right af-

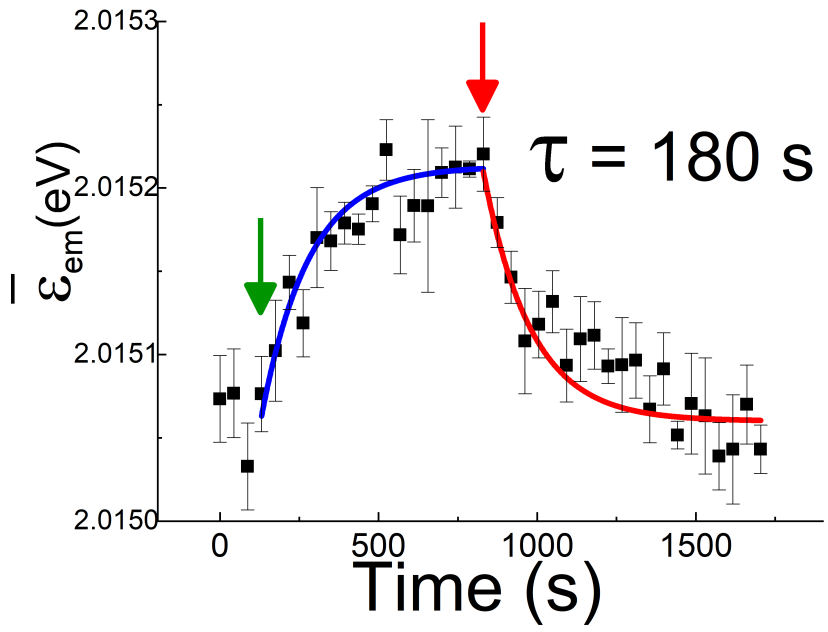

Figure 4.14. Mean emission energy of the sample's PL spectra during the experiment with longer duration. During the experiment $\tau_c = 30$ s was used in the experiment, where the pump laser ($\varepsilon_{ex} = 1.941$ eV) was introduced right after the fourth temperature measurement (green arrow) and turned off right after the eleventh measurement (red arrow).

ter the twentieth temperature measurement, red arrow). In this trial, the cooling and the heating patterns can still be described by the exponential curves with the same $\tau = 180$ s. As a conclusion, though the magnitude of the temperature change remains unclear, a thermal response was observed as evidenced by the sample's mean emission energy during the OR experiment. The data showed strong evidence that the net cooling effect was achieved in our OR experiment, with a maximum temperature drop of 0.68 ± 0.07 K.

5. SUMMARY AND PROSPECTS

Implementation of OR in QD materials was achieved for the first time. An OR experiment was designed and carried out in our lab and a maximum temperature drop of 0.68±0.07 K was observed in the zinc-blende crystalline CdSe/CdS (core/shell structure) QD samples under laser excitation ($\varepsilon_{ex} = 1.941$ eV).

A modified synthesis procedure based on a recently developed method [1, 2], was used to produce QDs samples. The method was reported to be able to ensure a perfect PL QY of the QDs, by removing any surface defects through surface passivation (an almost perfect PL QY is the most important criterion for a system to achieve OR according to the existing theoretical models of OR in solids). The characterization data of our homemade samples suggested a complete surface passivation was accomplished during our QDs production. However, the QY tests did not confirm the result, yielding a QY value of 60% for our sample. The research was able to be carried on based on a QDs property being reported by Loomis's group [97] that the QY of core/shell structure QDs approaches unity as the excitation energy decreases below the absorption edge.

The net cooling effect in the zinc-blende CdSe/CdS QDs was provided by the net energy up-conversion in QDs' mean emission energy at SBE, which was observed in our lab with the help of an enhanced-off-axis-collecting system developed for this research. The possible cooling mechanism was evaluated with a semi-empirical model developed in our lab. The model suggested that the dominating UCPL process observed in the QD samples' PL spectra with SBE needed to take into account both the LOP annihilation process and the acoustic phonon mediated exciton thermalization. Furthermore, the optimized excitation energy for OR cooling efficiency was also provided by the model, where a positive cooling efficiency was predicted with ε_{ex} around 1.94 eV with a maximum cooling efficiency close to 1%.

Based on the calculation result, the predicted net cooling power that could be achieved in the sample was limited. Thus, an OR experiment where the sample was thermally isolated was designed and built. To test the small temperature change produced by OR in the presence of heat exchange, an optical thermometry technique based on the temperature dependent energy bang gap of CdSe QDs was developed. A net cooling effect was observed within the range of the predicted excitation energies. Despite a deviation in the sample's temperature change between the experimental data and the simulation result from Comsol Multiphysics software, solid experimental evidence supports the observation that the net cooling effect in our sample was due to the OR processes.

As a conclusion, OR was achieved in our sample, while a maximum cooling power of $4.6 \pm 0.5\,\mu$W has been observed in our experiment. Data analysis suggests a cooling power of 1.26×10^{-14} W per dot. Therefore, significant cooling power can be achieved with a reasonable amount of QDs samples (*i. e.* 1 mol QDs from our sample could produce 7.6×10^9 W cooling power under proper illumination conditions), as the production of the QDs samples is suited for mass production.

This work has proved the capability of QDs materials to be used as a cooling substance for OR, which significantly expanded the possible candidates for OR (OR had only been reported in three kinds of solids systems [11, 22, 107]). The QD materials also provided a much wider selections of possible light sources for OR as their absorption and emission spectra are tunable by adjusting their size. The basic application of the technique could be used to cooling systems by using laser light. With the help of metamaterials, which can produce quasi-monochromatic light, the technique may also been used in harvesting cooling effect from sun light. Another possible application is using OR to cool the QDs in optical traps, where the heating effect due to background absorption limits the trapping capability. OR can help realizing strong spatial confinement of QDs (reaching quantum ground-state of QDs' mass of center motion) [105,108,109], which may help to develop new ultra-sensitive sensors [110,111] and application for quantum information science [112].

REFERENCES

[1] W. Nan, Y. Niu, H. Qin, F. Cui, Y. Yang, R. Lai, W. Lin, and X. Peng. Crystal structure control of zinc-blende CdSe/CdS core/shell nanocrystals: Synthesis and structure-dependent optical properties. *J. Am. Chem. Soc.*, **134**(48):19685–19693, 2012.

[2] C. Pu and X. Peng. To battle surface traps on CdSe/CdS core/shell nanocrystals: Shell isolation versus surface treatment. *J. Am. Chem. Soc.*, **138**(26):8134–8142, 2016.

[3] W. D. Phillips. Nobel lecture: Laser cooling and trapping of neutral atoms. *Rev. Mod. Phys.*, **70**:721–741, 1998.

[4] E. A. Cornell and C. E. Wieman. Nobel lecture: Bose-einstein condensation in a dilute gas, the first 70 years and some recent experiments. *Rev. Mod. Phys.*, **74**:875–893, 2002.

[5] P. Pringsheim. Zwei bemerkungen fiber den untersehied yon lumineszenz- und temperaturstrahlung. *Zeitschrift für Physik*, **57**:739–746, 1929.

[6] S. Vavilov. Some remarks on stokes law. *J. Phys.(Moscow)*, **9**:68–72, 1945.

[7] L. D. Landau. On the thermodynamics of photoluminescence. *J. Phys.(Moscow)*, **10**:503–507, 1946.

[8] J. E. Geusic, E. O. Schulz-DuBios, and H. E. D. Scovil. Quantum equivalent of the carnot cycle. *Phys. Rev.*, **156**:343–351, 1967.

[9] R. Epstein and M. Sheik-Bahae. *Optical refrigeration: science and application of laser cooling of solids*. Willey-VCH, Strauss GmbH, Mrlenbach, Germany, 2009.

[10] J. P. Gordon, H. J. Zeiger, and C. H. Townes. The maser—new type of microwave amplifier, frequency standard, and spectrometer. *Phys. Rev.*, **99**:1264–1274, 1955.

[11] R. I. Epstein, M. I. Bucwald, B. C. Edwards, T. R. Gosnell, and C. E. Mungan. Observation of laser-induced fluorescent cooling of a solid. *Nature*, **377**:500–503, 1995.

[12] J. L. Clark and G. Rumbles. Laser cooling in the condensed phase by frequency up-conversion. *Phys. Rev. Lett.*, **76**:2037–2040, 1996.

[13] C. E. Mungan, M. I. Buchwald, B. C. Edwards, R. I. Epstein, and T. R. Gosnell. Laser cooling of a solid by 16 K starting from room temperature. *Phys. Rev. Lett.*, **78**:1030–1033, 1997.

[14] S. R. Bowman and C. E. Mungan. New materials for optical cooling. *Appl. Phys. B*, **71**(6):807–811, 2000.

[15] A. Mendioroz, J. Fernández, M. Voda, M. Al-Saleh, R. Balda, and A. J. García-Adeva. Anti-Stokes laser cooling in Yb^{3+}-doped KPb_2Cl_5 crystal. *Opt. Lett.*, **27**(17):1525–1527, 2002.

[16] C. W. Hoyt, M. P. Hasselbeck, M. Sheik-Bahae, R. I. Epstein, S. Greenfield, J. Thiede, J. Distel, and J. Valencia. Advances in laser cooling of thulium-doped glass. *J. Opt. Soc. Am. B*, **20**(5):1066–1074, 2003.

[17] M. Sheik-Bahae and R. I. Epstein. Can laser light cool semiconductors? *Phys. Rev. Lett.*, **92**:247403, 2004.

[18] S. Bigotta, D. Parisi, L. Bonelli, A. Toncelli, M. Tonelli, and A. Di Lieto. Spectroscopic and laser cooling results on Yb^{3+}-doped BaY_2F_8 single crystal. *J. Appl. Phys.*, **100**(1):013109, 2006.

[19] J. Fernandez, A. J. Garcia-Adeva, and R. Balda. Anti-stokes laser cooling in bulk erbium-doped materials. *Phys. Rev. Lett.*, **97**:033001, 2006.

[20] W. Patterson, S. Bigotta, M. Sheik-Bahae, D. Parisi, M. Tonelli, and R. Epstein. Anti-stokes luminescence cooling of Tm^{3+}doped BaY_2F_8. *Opt. Express*, **16**(3):1704–1710, 2008.

[21] D. V. Seletskiy, S. D. Melgaard, S. Bigotta, A. D. Lieto, M. Tonelli, and M. Sheik-Bahae. Laser cooling of solids to cryogenic temperatures. *Nat. photonics*, **4**:161–164, 2010.

[22] J. Zhang, D. Li, R. Chen, and Q. Xiong. Laser cooling of a semiconductor by 40 Kelvin. *Nat. Lett.*, **493**:504–508, 2012.

[23] A. I. Ekimov, Al. L. Efros, and A. A. Onushchenko. Quantum size effect in semiconductor microcrystals. *Solid State Commun.*, **56**(11):921–924, 1985.

[24] V. I. Klimov, A. A. Mikhailovsky, S. Xu, A. Malko, J. A. Hollingsworth, C. A. Leatherdale, H.-J. Eisler, and M. G. Bawendi. Optical gain and stimulated emission in nanocrystal quantum dots. *Science*, **290**:314–317, 2000.

[25] R. Azmi, S. Oh, and S. Jang. High-efficiency colloidal quantum dot photovoltaic devices using chemically modified heterojunctions. *ACS Energy Lett.*, **1**(1):100–106, 2016.

[26] L. Zan, D. Lin, P. Zhong, and G. He. Optimal spectra of white LED integrated with quantum dots for mesopic vision. *Opt. Express*, **24**(7):7643–7653, 2016.

[27] G. Liakhou, S. Paoloni, and M. Bertolotti. Observations of laser cooling by resonant energy transfer in CO_2-N_2 mixtures. *J. Appl. Phys*, **96**(8):4219–4224, 2004.

[28] C. H. Henry and D. V. Lang. Nonradiative capture and recombination by multiphonon emission in GaAs and GaP. *Phys. Rev. B*, **15**:989–1016, 1977.

[29] N. W. Ashcroft and N. D. Mermin. *Solid State Physics*. Brooks and Cole, Belmont, CA 94002-3098, USA, 1976.

[30] M. Cardona, editor. *Light Scattering in Solids I.* Springer-Verlag, Berlin Heidelberg New York, 2nd edition, 1983.

[31] A.I. Ekimov, A. Onushchehko, and V.A. Tsekhomskii. Exciton absorption of CuCl crystals in a glassy matrix. *Fiz. Khim. Stekl*, **6**:511–512, 1980.

[32] K. Brunner, U. Bockelmann, G. Abstreiter, M. Walther, G. Böhm, G. Tränkle, and G. Weimann. Photoluminescence from a single GaAs/AlGaAs quantum dot. *Phys. Rev. Lett.*, **69**:3216–3219, 1992.

[33] A. Efros and Al. L. Efros. Interband light absorption in semiconductor spheres. *Soviet physics. Semiconductors*, **16**:772–775, 1982.

[34] M. A. Reed, R. T. Bate, K. Bradshaw, W. M. Duncan, W. R. Frensley, J. W. Lee, and H. D. Shih. Spatial quantization in GaAsAlGaAs multiple quantum dots. *J. Vac. Sci. Technol. B Nanotechnol. Microelectron.*, **4**(1):358–360, 1986.

[35] C. B. Murray, D. J. Norris, and M. G. Bawendi. Synthesis and characterization of nearly monodisperse CdE (E = sulfur, selenium, tellurium) semiconductor nanocrystallites. *J. Am. Chem. Soc.*, **115**(19):8706–8715, 1993.

[36] V. K. LaMer and R. H. Dinegar. Theory, production and mechanism of formation of monodispersed hydrosols. *J. Am. Chem. Phys.*, **72**(11):4847–4854, 1950.

[37] H. Liu, J. S. Owen, and A. P. Alivisatos. Mechanistic study of precursor evolution in colloidal group II-VI semiconductor nanocrystal synthesis. *J. Am. Chem. Phys.*, **129**(2):305–312, 2007.

[38] L. Qu and X. Peng. Control of photoluminescence properties of CdSe nanocrystals in growth. *J. Am. Chem. Soc.*, **124**(9):2049–2055, 2002.

[39] Y. A. Yang, H. Wu, K. R. Williams, and Y. C. Cao. Synthesis of CdSe and CdTe nanocrystals without precursor injection. *Angew. Chem. Int. Edit.*, **44**(41):6712–6715, 2005.

[40] K. R. Čapek, I. Moreels, K. Lambert, D. De Muynck, Q. Zhao, V. A. Tomme, F. Vanhaecke, and Z. Hens. Optical properties of zincblende cadmium selenide quantum dots. *J. Chem. Phys. C.*, **114**(14):6371–6376, 2010.

[41] C. R. Bullen and P. Mulvaney. Nucleation and growth kinetics of CdSe nanocrystals in octadecene. *Nano Lett.*, **4**(12):2303–2307, 2004.

[42] I. Coropceanu, A. Rossinelli, J. R. Caram, F. S. Freyria, and M. G. Bawendi. Slow-injection growth of seeded CdSe/CdS nanorods with unity fluorescence quantum yield and complete shell to core energy transfer. *ACS Nano*, **10**(3):3295–3301, 2016.

[43] O. Chen, X. Chen, Y. Yang, J. Lynch, H. Wu, J. Zhuang, and Y. C. Cao. Synthesis of metalselenide nanocrystals using selenium dioxide as the selenium precursor. *Angew. Chem. Int. Edit.*, **47**(45):8638–8641, 2008.

[44] L. E. Brus. A simple model for the ionization potential, electron affinity, and aqueous redox potentials of small semiconductor crystallites. *J. Chem. Phys.*, **79**(11):5566–5571, 1983.

[45] L. E. Brus. Electron-electron and electron-hole interactions in small semiconductor crystallites: The size dependence of the lowest excited electronic state. *J. Chem, Phys*, **80**:4403–4409, 1984.

[46] H. Weller, H. M. Schmidt, U. Koch, A. Fojtik, S. Baral, A. Henglein, W. Kunath, K. Weiss, and E. Dieman. Photochemistry of colloidal semiconductors. Onset of light absorption as a function of size of extremely small CdS particles. *Chem. Phys. Lett.*, **124**(6):557 – 560, 1986.

[47] A. P. Alivisatos, A. L. Harris, N. J. Levinos, M. L. Steigerwald, and L. E. Brus. Electronic states of semiconductor clusters: homogeneous and inhomogeneous broadening of the optical spectrum. *J. Chem. Phys.*, **89**(7):4001–4011, 1988.

[48] W. C. W. Chan and S. Nie. Quantum dot bioconjugates for ultrasensitive nonisotopic detection. *Science*, **281**:2016–2018, 1998.

[49] C. Kittel. *Introduction to Solid State Physics*. John Wiley & Sons, New York, 6th edition, 1986.

[50] S. Baskoutas and A. F. Terzis. Size-dependent band gap of colloidal quantum dots. *J. Appl. Phys.*, **99**(1):013708, 2006.

[51] V. A. Fedorov, V. A. Ganshin, and Y. N. Korkishko. Determination of the point of the zincblende-to-wurtzite structural phase transition in cadmium selenide crystals. *Phys. Status Solidi A*, **126**(1):K5–K7, 1991.

[52] L. Manna, E. C. Scher, and A. P. Alivisatos. Synthesis of soluble and processable rod-, arrow-, teardrop-, and tetrapod-shaped CdSe nanocrystals. *J. Am. Chem. Soc.*, **122**(51):12700–12706, 2000.

[53] Z. A. Peng and X. Peng. Nearly monodisperse and shape-controlled CdSe nanocrystals via alternative routes: nucleation and growth. *J. Am. Chem. Phys.*, **124**(13):3343–3353, 2002.

[54] Z. Adam and X. Peng. Mechanisms of the shape evolution of CdSe nanocrystals. *J. Am. Chem. Soc.*, **123**:1389–1395, 2001.

[55] M. B. Mohamed, D. Tonti, A. Al-Salman, A. Chemseddine, and M. Chergui. Synthesis of high quality zinc blende CdSe nanocrystals. *J. Phys. Chem. B*, **109**(21):10533–10537, 2005.

[56] X. Wang, L. Qu, J. Zhang, X. Peng, and M. Xiao. Surface-related emission in highly luminescent CdSe quantum dots. *Nano Lett.*, **3**:1103–1106, 2003.

[57] T. Rajh, L. X. Chen, K. Lukas, T. Liu, M. C. Thurnauer, and D. M. Tiede. Surface restructuring of nanoparticles: an efficient route for ligand-metal oxide crosstalk. *J. Phys. Chem. B*, **106**(41):10543–10552, 2002.

[58] S. Schmitt-Rink, D. A. B. Miller, and D. S. Chemla. Theory of the linear and nonlinear optical properties of semiconductor microcrystallites. *Phys. Rev. B*, **35**:8113–8125, 1987.

[59] T. Takagahara. Electron-phonon interactions and excitonic dephasing in semiconductor nanocrystals. *Phys. Rev. Lett.*, **71**:3577–3580, 1993.

[60] M. R. Salvador, M. W. Graham, and G. D. Scholes. Exciton-phonon coupling and disorder in the excited states of CdSe colloidal quantum dots. *J. Chem. Phys.*, **125**:184709, 2006.

[61] P. Y. Yu and M. Cardona. *Fundamentals of Semiconductors*. Springer, 2003.

[62] Y. Gao and X. Peng. Photogenerated excitons in plain core CdSe nanocrystals with unity radiative decay in single channel: The effects of surface and ligands. *J. Am. Chem. Phys.*, **137**(12):4230–4235, 2015.

[63] A. P. Alivisatos, T. D. Harris, P. J. Carroll, M. L. Steigerwald, and L. E. Brus. Electron-vibration coupling in semiconductor clusters studied by resonance Raman spectroscopy. *J. Chem. Phys.*, **90**(7):3463–3468, 1989.

[64] K. Huang and R. Han. *Solid state physics*. Higher education press, Beijing, China, 21st edition, 2005.

[65] A. M. Kelley. Electron-phonon coupling in CdSe nanocrystals from an atomistic phonon model. *ACS Nano*, **5**(6):5254–5262, 2011.

[66] J. M. Luttinger and W. Kohn. Motion of electrons and holes in perturbed periodic fields. *Phys. Rev.*, **97**:869–883, 1955.

[67] D. J Norris and V. I. Klimov. *Nanocrystal quantum dots*. CRC press, 2nd edition, 2010.

[68] B. Zorman, M. V. Ramakrishna, and R. A. Friesner. Quantum confinement effects in CdSe quantum dots. *J. Chem. Phys.*, **99**(19):7649–7653, 1995.

[69] K. A. Jackson and W. Schroter. *Handbook of Semiconductor Technology*. Wiley-Blackwell, 2008.

[70] R. L. Liboff. *Introductary quantum mechanics*. Addison-Wesley, Glenview, IL 60025, USA, 4th edition, 2003.

[71] J. J. Sakurai and Jim Napolitano. *Modern Quantum Mechanics*. Addison-Wesley, 2nd edition, 2011.

[72] Al. L. Efros. Luminescence polarization of CdSe microcrystals. *Phys. Rev. B.*, **46**:7448–7458, 1992.

[73] B. Fisher, H.-J. Eisler, N. Stott, and G. M. Bawendi. Emission intensity dependence and single-exponential behavior in single colloidal quantum dot fluorescence lifetimes. *J. Phys. Chem. B*, **108**:143–148, 2003.

[74] M. Califano, A. Franceschetti, and A. Zunger. Temperature dependence of excitonic radiative decay in CdSe quantum dots: the role of surface hole traps. *Nano Lett.*, **5**(12):2360–2364, 2005.

[75] W. Z. Lee, G. W. Shu, J. S. Wang, J. L. Shen, C. A. Lin, W. H. Chang, R. C. Ruaan, W. C. Chou, C. H. Lu, and Y. C. Lee. Recombination dynamics of luminescence in colloidal CdSe/ZnS quantum dots. *Nanotechnology*, **16**(9):1517–1521, 2005.

[76] S. Bounouar, C. Morchutt, M. Elouneg-Jamroz, L. Besombes, R. André, E. Bellet-Amalric, C. Bougerol, M. D. Hertog, K. Kheng, S. Tatarenko, and J. Ph. Poizat. Exciton-phonon coupling efficiency in CdSe quantum dots embedded in ZnSe nanowires. *Phys. Rev. B*, **85**:035428, 2012.

[77] A. M. Kelley, Q. Dai, Z. Jiang, J. A. Baker, and D. F. Kelley. Resonance Raman spectra of wurtzite and zincblende CdSe nanocrystals. *Chem. Phys.*, **422**:272 – 276, 2013. Note: a tribute to Dr. Robin Hochstasser.

[78] A. Giugni, G. Das, A. Alabastri, R. P. Zaccaria, M. Zanella, I. Franchini, E. D. Fabrizio, and R. Krahne. Optical phonon modes in ordered core-shell CdSe/CdS nanorod arrays. *Phys. Rev. B*, **85**:115413, 2012.

[79] J. Zhang, X. Wang, and M. Xiao. Lattice contraction in free-standing CdSe nanocrystals. *Appl. Phys. Lett.*, **81**:2076–2078, 2002.

[80] G. P. Srivastava. *The physics of phonons*. Adam Hilger, New York, NY 10017-3483, USA, 1st edition, 1990.

[81] M. Grabolle, M. Spieles, V. Lesnyak, N. Gaponik, A. Eychmller, and U. Resch-Genger. Determination of the fluorescence quantum yield of quantum dots: suitable procedures and achievable uncertainties. *Anal. Chem.*, **81**(15):6285–6294, 2009.

[82] O. E. Semonin, J. C. Johnson, J. M. Luther, A. G. Midgett, A. J. Nozik, and M. C. Beard. Absolute photoluminescence quantum yields of IR-26 dye, PbS, and PbSe quantum dots. *J. Chem. Phys. Lett.*, **1**(16):2445–2450, 2010.

[83] N. Chestnoy, T. D. Harris, R. Hull, and L. E. Brus. Luminescence and photophysics of cadmium sulfide semiconductor clusters: the nature of the emitting electronic state. *J. Chem. Phys.*, **90**:3393–3399, 1986.

[84] A. Veamatahau, B. Jiang, T. Seifert, S. Makuta, K. Latham, M. Kanehara, T. Teranishi, and Y. Tachibana. Origin of surface trap states in CdS quantum dots: relationship between size dependent photoluminescence and sulfur vacancy trap states. *Phys. Chem. Chem. Phys.*, **17**:2850–2858, 2015.

[85] C. Wang, Y. Jiang, L. Chen, S. Li, G. Li, and Z. Zhang. Temperature dependence of optical properties and size tunability CdSe quantum dots via non-top synthesis. *Mater. Chem. Phys.*, **116**(2):388–391, 2009.

[86] I. Moreels, G. Rain, R. Gomes, Z. Hens, T. Stferle, and R. F. Mahrt. Band-edge exciton fine structure of small, nearly spherical colloidal CdSe/ZnS quantum dots. *ACS Nano*, **5**(10):8033–8039, 2011.

[87] H. Yokota, K. Shimura, M. Nakayama, and D. Kim. Optical properties of self-assembled monolayer of CdSe quantum dots. *Phys. Status Solidi C*, **9**(12):2465–2468, 2012.

[88] O. Chen, J. Zhao, V. P. Chauchan, J. Cui, C. Wong, D. K. Harris, H. Wei, H. Han, D. Fukumura, R. K. Jain, and M. G. Bawendi. Compact high-quality CdSe-CdS core-shell nanocrystals with narrow emission linewidths and suppressed blinking. *Nat. Mater*, **12**:445–451, 2013.

[89] *Optical glass collection datasheets*. Schott, 2014.

[90] F. L. Pedrotti, L. S. Pedrotti, and L. M. Pedrotti. *Introduction to optics*. Pearson Prentice Hall, New Jersey, NJ 07458, USA, 2007.

[91] R. A. Harris, P. M. Shumbula, and H. van der Walt. Analysis of the interaction of surfactants oleic acid and oleylamine with iron oxide nanoparticles through molecular mechanics modeling. *Langmuir*, **31**(13):3934–3943, 2015.

[92] K. Manthiram, B. J. Beberwyck, D. V. Talapin, and A. P Alivisatos. Seeded synthesis of CdSe/CdS rod and tetrapod nanocrystals. *J. Vis. Exp.*, **82**:e50731, 2013.

[93] D. Chen, F. Zhao, H. Qi, M. Rutherford, and X. Peng. Bright and stable purple/blue emitting CdS/ZnS core/shell nanocrystals grown by thermal cycling using a single-source precursor. *Chem. Mater.*, **22**(4):1437–1444, 2010.

[94] S. M. Sze. *Physics of semiconductor devices*. Wiley, New York, USA, 2nd edition, 1981.

[95] C. Wrth, M. Grabolle, J. Pauli, M. Spieles, and U. Resch-Genger. Relative and absolute determination of fluorescence quantum yields of transparent samples. *Nat. Protoc.*, **8**:1535, 2013.

[96] R. F. Kubin and A. N. Fletcher. Fluorescence quantum yields of some rhodamine dyes. *J. Lumin.*, **27**(4):455 – 462, 1982.

[97] J. Hoy, P. J. Morrison, L. K. Steinberg, W. E. Buhro, and R. A. Loomis. Excitation energy dependence of the photoluminescence quantum yields of core and core/shell quantum dots. *J. Phys. Chem.*, **4**:2053–2060, 2013.

[98] D. Geiler, C. Wrth, C. Wolter, H. Weller, and U. Resch-Genger. Excitation wavelength dependence of the photoluminescence quantum yield and decay behavior of CdSe/CdS quantum dot/quantum rods with different aspect ratios. *Phys. Chem. Chem. Phys.*, **19**:12509–12516, 2017.

[99] R. Luchowski, Z. Gryczynski, P. Sarkar, J. Borejdo, M. Szabelski, P. Kapusta, and I. Gryczynski. Instrument response standard in time-resolved fluorescence. *Rev. Sci. Instrum.*, **80**(3):033109, 2009.

[100] Horiba Jobin-Yvon. *Triax Series Spectrometer*.

[101] K. Gong, J. E. Martin, L. E. Shea-Rohwer, P. Lu, and D. F. Kelley. Radiative lifetimes of zincblende CdSe/CdS quantum dots. *J. Chem. Phys. C.*, **119**(4):2231–2238, 2015.

[102] S. F. Wuister, A. V. Houselt, C. de Mello Doneg, D. Vanmaekelbergh, and A. Meijerink. Temperature antiquenching of the luminescence from capped CdSe quantum dots. *Angew. Chem. Int. Edit.*, **43**(23):3029–3033, 2004.

[103] D. Valerini, A. Cretí, M. Lomascolo, L. Manna, R. Cingolani, and M. Anni. Temperature dependence of the photoluminescence properties of colloidal CdSe/ZnS core/shell quantum dots embedded in a polystyrene matrix. *Phys. Rev. B*, **71**:235409, 2005.

[104] C. Lin, K. Gong, D. F. Kelley, and A. M. Kelley. Electronphonon coupling in CdSe/CdS core/shell quantum dots. *ACS Nano*, **9**(8):8131–8141, 2015.

[105] D. E. Chang, C. A. Regal, S. B. Papp, D. J. Wilson, J. Ye, O. Painter, H. J. Kimble, and P. Zoller. Cavity opto-mechanics using an optically levitated nanosphere. *PNAS*, **107**(3):1005–1010, 2010.

[106] Opto Science, Inc. *IR Materials: $AgGaS_2$, $AgGaSe_2$, CdS and CdSe.*

[107] S. Ha, C. Shen, J. Zhang, and Q. Xiong. Laser cooling of organic-inorganic lead halide perovskites. *Nat. Photonics*, **10**:115–121, 2015.

[108] G. Ranjit, D. P. Atherton, J. H. Stutz, M. Cunningham, and A. A. Geraci. Attonewton force detection using microspheres in a dual-beam optical trap in high vacuum. *Phys. Rev. A*, **91**:051805, 2015.

[109] E. Hebestreit, R. Reimann, M. Frimmer, and L. Novotny. Measuring the internal temperature of a levitated nanoparticle in high vacuum. *Phys. Rev. A*, **97**:043803, 2018.

[110] A. A. Geraci, S. B. Papp, and J. Kitching. Short-range force detection using optically cooled levitated microspheres. *Phys. Rev. Lett.*, **105**:101101, 2010.

[111] A. Arvanitaki and A. A. Geraci. Detecting high-frequency gravitational waves with optically levitated sensors. *Phys. Rev. Lett.*, **110**:071105, 2013.

[112] A. N. Cleland and M. R. Geller. Superconducting qubit storage and entanglement with nanomechanical resonators. *Phys. Rev. Lett.*, **93**:070501, 2004.

APPENDIX

Absorption and PL emission information of QDs samples from different synthesis batches.

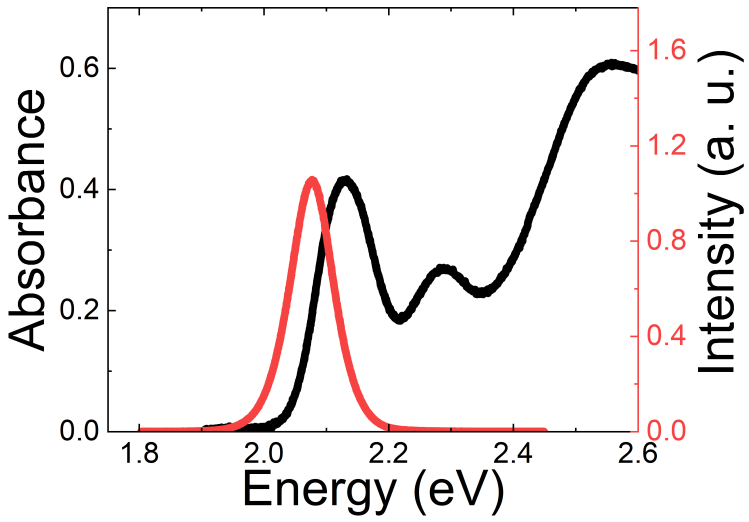

Figure 1. Absorption and PL emission spectra of the QDs synthesized in batch 1. The PL emission spectra was derived with an excitation energy of 3.05 eV.

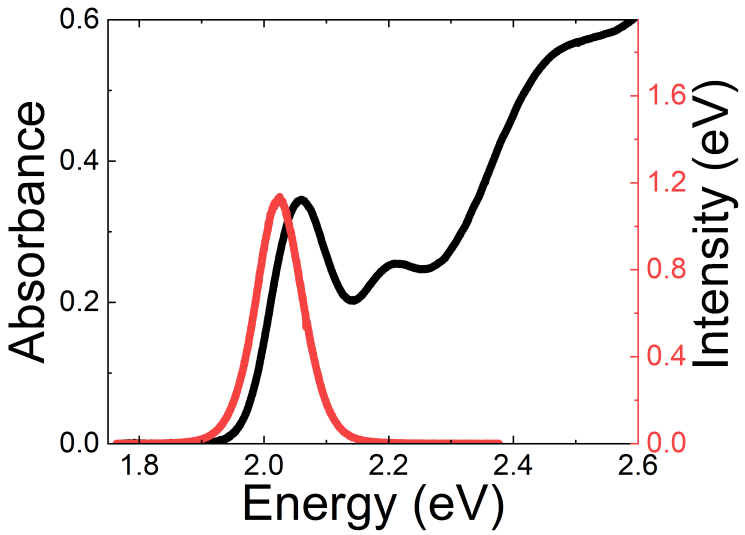

Figure 2. Absorption and PL emission spectra of the QDs synthesized in batch 2. The PL emission spectra was derived with an excitation energy of 3.05 eV.

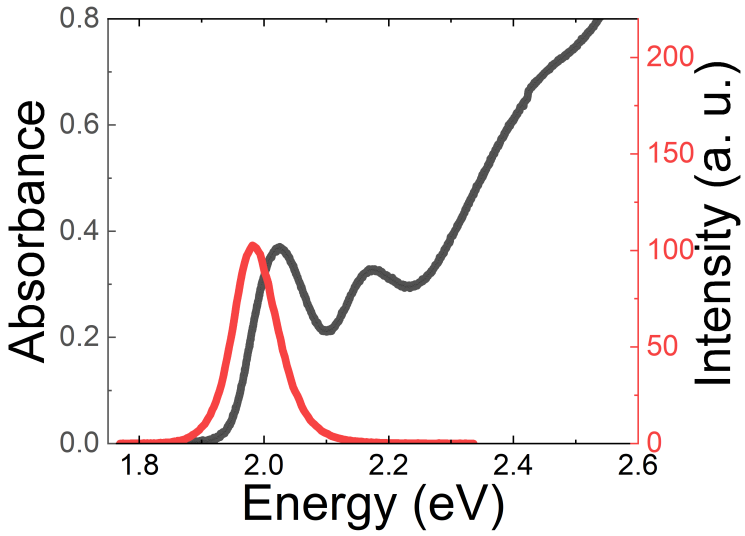

Figure 3. Absorption and PL emission spectra of the QDs synthesized in batch 3. The PL emission spectra was derived with an excitation energy of 3.05 eV.

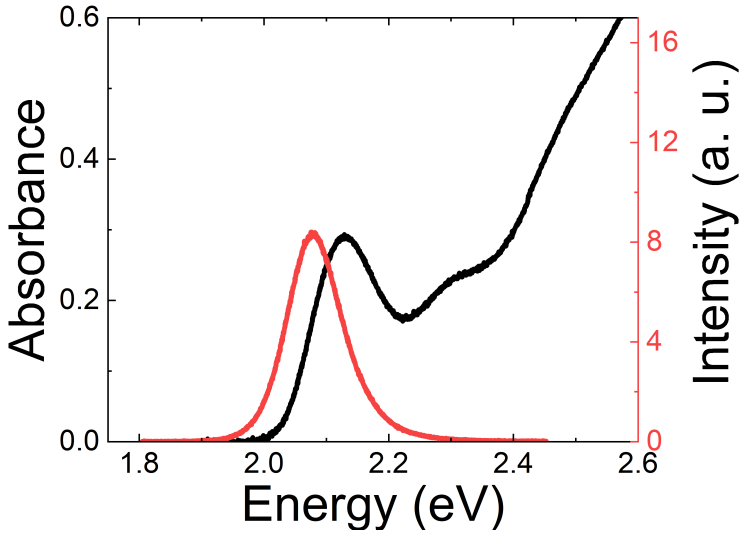

Figure 4. Absorption and PL emission spectra of the QDs synthesized in batch 4. The PL emission spectra was derived with an excitation energy of 3.05 eV.

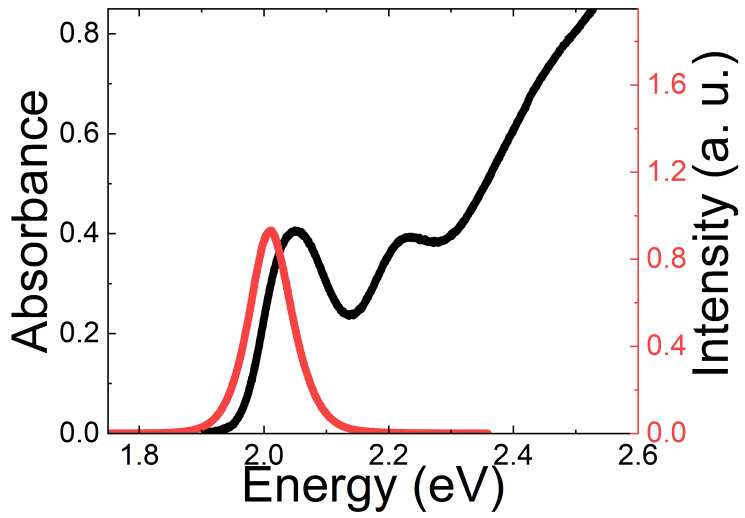

Figure 5. Absorption and PL emission spectra of the QDs synthesized in batch 5. The PL emission spectra was derived with an excitation energy of 3.05 eV.

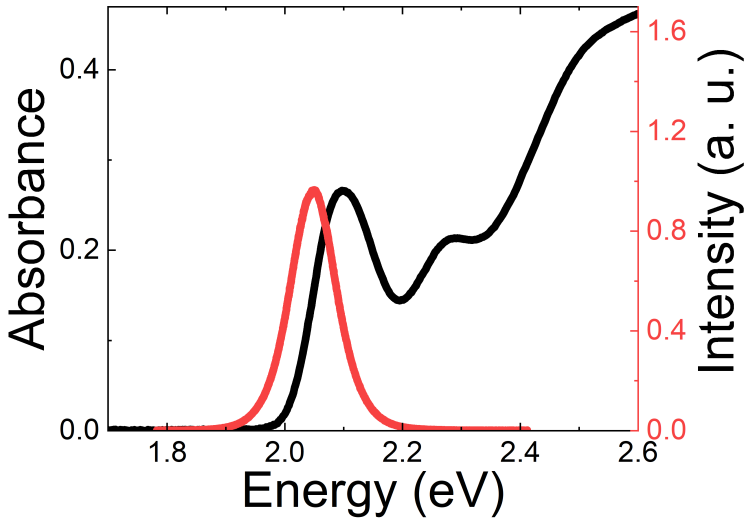

Figure 6. Absorption and PL emission spectra of the QDs synthesized in batch 6. The PL emission spectra was derived with an excitation energy of 3.05 eV.

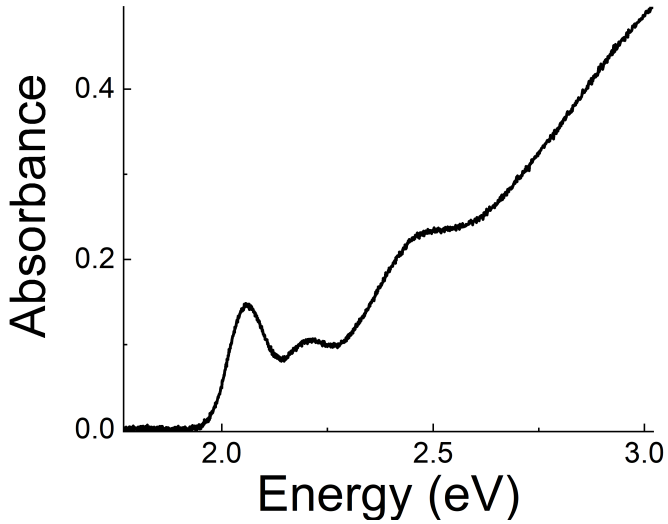

Figure 7. Absorption spectrum of the QDs synthesized in batch 2. The sample was diluted with hexane by 300 times to derive precise value of the absorbance at high energy excitation.